

University of Alberta

The Influence of Convection on Zone Refining

by

Errol John Edward Halberg



A thesis submitted to the Faculty of Graduate Studies and Research
in partial fulfillment of the requirements for the degree of

Master of Science in Chemical Engineering

Department of Chemical and Materials Engineering

Edmonton, Alberta

Spring 2007



Library and
Archives Canada

Bibliothèque et
Archives Canada

Published Heritage
Branch

Direction du
Patrimoine de l'édition

395 Wellington Street
Ottawa ON K1A 0N4
Canada

395, rue Wellington
Ottawa ON K1A 0N4
Canada

Your file *Votre référence*
ISBN: 978-0-494-29965-4
Our file *Notre référence*
ISBN: 978-0-494-29965-4

NOTICE:

The author has granted a non-exclusive license allowing Library and Archives Canada to reproduce, publish, archive, preserve, conserve, communicate to the public by telecommunication or on the Internet, loan, distribute and sell theses worldwide, for commercial or non-commercial purposes, in microform, paper, electronic and/or any other formats.

The author retains copyright ownership and moral rights in this thesis. Neither the thesis nor substantial extracts from it may be printed or otherwise reproduced without the author's permission.

AVIS:

L'auteur a accordé une licence non exclusive permettant à la Bibliothèque et Archives Canada de reproduire, publier, archiver, sauvegarder, conserver, transmettre au public par télécommunication ou par l'Internet, prêter, distribuer et vendre des thèses partout dans le monde, à des fins commerciales ou autres, sur support microforme, papier, électronique et/ou autres formats.

L'auteur conserve la propriété du droit d'auteur et des droits moraux qui protègent cette thèse. Ni la thèse ni des extraits substantiels de celle-ci ne doivent être imprimés ou autrement reproduits sans son autorisation.

In compliance with the Canadian Privacy Act some supporting forms may have been removed from this thesis.

Conformément à la loi canadienne sur la protection de la vie privée, quelques formulaires secondaires ont été enlevés de cette thèse.

While these forms may be included in the document page count, their removal does not represent any loss of content from the thesis.

Bien que ces formulaires aient inclus dans la pagination, il n'y aura aucun contenu manquant.


Canada

Abstract

Zone refining is a process commonly used to purify metals or semiconductors to ultra low (ppb) impurity levels. The purpose of this project is to improve the zone refining process by applying knowledge of the fundamental transport mechanisms. A dimensional analysis and experimental study was undertaken to determine the appropriate operating conditions for improving the yield and/or separation efficiency. Using lead as a model material, instrumented zone refining experiments were carried out on an industrial unit. An analysis of thermocouple data revealed that convection complexity was dependent on ingot geometry and external temperature gradients. Segregation efficiency was calculated by fitting chemical analysis data gathered via glow discharge mass spectrometry to a mass balance model of the molten zone. The best separation efficiency was measured during low convection complexity at the solid/liquid interface. Recommendations for enhancing process efficiency include decreasing ingot geometry and reducing temperature gradients using insulation.

Acknowledgments

I'd like to thank Genevieve Gabriel and my family for their love, support, and patience. Thanks to Dr. Henein and Dr. Forbes for their guidance and wisdom. A special thanks to Bill Micklethwaite and Colin Carew at Firebird Technologies. This research would not have been possible without such inspiring and generous people. Thanks to Doug Halberg for his help in editing this thesis.

Table of Contents

Chapter 1 Introduction.....	1
1.1 General Description of Zone Refining.....	1
1.2 Driving Force for Segregation.....	3
1.3 Statement of Problem.....	4
1.4 Outline of Thesis.....	5
Chapter 2 Process Modeling and Analysis.....	7
2.1 Impurity Distribution Models.....	7
2.2 Governing Equations.....	11
2.3 Dimensional Analysis.....	13
2.3.1 Grashof and Marangoni Numbers.....	15
2.3.2 Prandtl and Schmidt Numbers.....	16
2.3.3 Rayleigh Number.....	17
2.3.4 Peclet Number.....	18
2.4 Calculating the Segregation Rate.....	21
2.5 Deficiencies of the Burton, Prim, and Schlichter Theory.....	23
2.5.1 Varying Boundary Conditions.....	24
2.5.2 Varying Thermal Conditions.....	24
2.5.3 Fluid Flow Effects.....	25
2.6 Summary of Process Modeling and Analysis.....	27
Chapter 3 Experimental Procedures.....	28
3.1 Zone Refining Machine.....	28
3.2 Experimental Design.....	31

3.2.1	Manipulated Variables	31
3.2.2	Control Variables	32
3.2.3	Test Matrix.....	34
3.3	Thermocouple Tests.....	36
3.3.1	Thermocouple Testing Procedure	41
3.4	Assay Tests	42
3.5	Summary of Experimental Procedures	43
Chapter 4	Discussion of Experimental Results	45
4.1	Typical Thermocouple Data	45
4.2	Analysis of General Temperature Trends	50
4.2.1	Temperature Visualization.....	50
4.2.2	Measured Grashof Numbers	58
4.2.3	Critical Grashof Number.....	61
4.2.4	Marangoni Flow.....	62
4.3	Analysis of Temperature Fluctuations	65
4.3.1	Discrete Fourier Transform.....	66
4.3.2	Visualization of Frequency Spectra	71
4.3.3	Power Spectral Density.....	79
4.4	Assay Tests	85
4.4.1	Mass Balance Model.....	86
4.4.2	Separation Efficiency.....	86
4.5	Summary of Experimental Results	90
Chapter 5	Improving Separation Efficiency.....	91

5.1	Separation Efficiency in Relation to Convection.....	91
5.1.1	Dominant Transport Phenomenon	92
5.2	Beneficial Control Measures.....	95
5.2.1	Enclosure Depth.....	95
5.2.2	External Temperature Gradients	97
5.2.3	Interface Shape.....	98
5.3	Application to Different Materials.....	99
5.3.1	Stefan Number	100
5.3.2	Estimations of Fluid Flow Regime	103
Chapter 6	Conclusions and Future work.....	107
6.1	Conclusions.....	107
6.2	Future Work	109
Chapter 7	Appendices.....	124
Appendix A	Specifications for the Thermocouples, Drywell Calibrator	124
Appendix B	Raw Data from Tests 1, 3, 4, and 5.....	129
Appendix C	High and Low Pass Filter Design	131
Appendix D	Wavelet Spectrum Plots for Tests 1, 3, 4, and 5	133
Appendix E	Mass Balance Model Program	139
Appendix F	Linear Least Squares Program	144

List of Tables

Table 2-1: Dimensionless numbers relevant to the zone refining system	15
Table 2-2: Material Properties of Pb at T=600.5K [44][45].....	18
Table 3-1: Controlled variables for thermocouple and assay experiments.....	33
Table 3-2: Test matrix for thermal measurement experiments.....	34
Table 3-3: Position of thermocouples in surface planes	40
Table 3-4: Position of thermocouples in vertical planes.....	41
Table 3-5: Summary of passes done during thermocouple tests.....	42
Table 4-1: Temperature Gradients, Characteristic Length and Grashof	60
Table 4-2: Critical Grashof Numbers from Literature.....	61
Table 4-3: Sample spectral density for Test 5, plane 'C', pass 3.....	80
Table 4-4: Sample Spectral Density for Test 1, plane 'C', pass 2	80
Table 4-5: Maximum power spectral density threshold for all tests.....	81
Table 4-6: Threshold count at the interfaces, averaged between passes.....	82
Table 4-7: Calculated separation coefficients.....	89
Table 5-1: Summary temperature gradient and critical Grashof number ranking....	105
Table A-1: Thermocouple Specifications.....	124
Table A-2: Thermocouple calibration offset in degrees Celsius	125
Table A-3: Drywell calibrator specifications.....	126
Table A-4: Fluke 725 Multifunction Calibrator specifications.....	127
Table A-5: List of data acquisition equipment.....	128

List of Figures

Figure 1-1: Zone refining schematic.....	2
Figure 1-2: Dilute Binary Phase Diagram	3
Figure 2-1: Impurity distribution for different zone lengths, $k=0.3$, $n= 10$ passes	10
Figure 2-2: Schematic of the Molten Zone for $k<1$	12
Figure 2-3: Characteristic Distance (D/V) as a function of the growth rate.....	20
Figure 2-4: Hypothetical momentum and concentration boundary layer thicknesses	21
Figure 2-5: Stagnant film in solute transport during melt growth.	23
Figure 2-6: Non uniform solute layer thickness.	24
Figure 3-1: Zone refining heater assembly	29
Figure 3-2: Cross section of tube, boat, and heaters	29
Figure 3-3: Schematic of heater movement.....	30
Figure 3-4: Cooling fan applied to the exterior of the tube for Test 1	35
Figure 3-5: Insulation added on top of the tube and in front of the heater for Test 5.	36
Figure 3-6: Thermocouple pass-through.....	37
Figure 3-7: Thermocouple Configuration within the zone refining apparatus	39
Figure 3-8: Placement of surface (horizontal) thermocouple in planes A and B.....	40
Figure 3-9: Placement of vertical thermocouples in planes C through F	41
Figure 4-1: Typical Temperature Data of the Molten Zone	46
Figure 4-2: Orientation of 2-D contour plots.....	50
Figure 4-3: Lengthwise temperature contour plot of the molten zone for.....	51
Figure 4-4: Typical horizontal interface shape	54
Figure 4-5: Heating element surrounding the zone.....	57

Figure 4-6: Average log of Grashof versus Test number for planes C and D	60
Figure 4-7: Surface film covering the molten zone during lead experiments.....	63
Figure 4-8: Oscillatory flow-Numerically calculated stream function of a fluid	66
Figure 4-9: Temperature oscillations in relation to fluid flow regime.....	66
Figure 4-10: Fourier transform of a solid region of Test 5, Plane 'C'	68
Figure 4-11: Fourier transform of a simple liquid sample, Test 5, plane 'C'	69
Figure 4-12: Fourier transform of a complex liquid sample, Test 1, plane 'C'	70
Figure 4-13: Wavelet Power Spectrum plot for Test 2, plane 'C'	72
Figure 4-14: Wavelet Power Spectrum, Test 2, plane 'C'	73
Figure 4-15: Wavelet Power Spectrum, Test 2, plane 'C'	74
Figure 4-16: Wavelet Power Spectrum, Test 2, plane 'C'	75
Figure 4-17: Contour plot for Test 2, pass 2.....	75
Figure 4-18: Representation of toroidal flow	78
Figure 4-19: Averaged maximum power spectral density and Grashof number	81
Figure 4-20: Power spectral density at the freezing and melting interfaces,.....	82
Figure 4-21: Average distance between the heater and the freezing interface	84
Figure 4-22: Power spectral density versus the distance between.....	85
Figure 4-23: Best fit model to Iodine, Test 5 (calculated $k_{eff}=0.41$).....	87
Figure 4-24: Calculated effective distribution coefficient (k_{eff}) fitted to assay data ..	87
Figure 5-1: Qualitative relationship between convection and separation efficiency..	93
Figure 5-2: Varying boat cross section shape	96
Figure 5-3: Stefan coefficient ($\Delta H_f/C_p$) for metals at their melting temperature.....	101
Figure 5-4: Approximate separation efficiency versus fluid flow regime	102

Figure 5-5: Prandtl numbers of metals at their respective melting points	104
Figure 5-6: Melting temperature for various metals	105
Figure B-1: Sample raw data from Test 1, Plane 'C', pass 3	129
Figure B-2: Sample raw data from Test 3, Plane 'C', pass 3	129
Figure B-3: Sample raw data from Test 4, Plane 'C', pass 2	130
Figure B-4: Sample raw data from Test 5, Plane 'C', pass 1	130
Figure C-1: Temperature data from Test 2, plane 'C', top thermocouple	131
Figure C-2: Discrete Fourier transform of the top thermocouple	132
Figure D-1: Wavelet spectrum, Test 1, top thermocouple, plane 'C', pass 3	133
Figure D-2: Wavelet spectrum, Test 1, upper-mid thermocouple, plane 'C' pass 3..	133
Figure D-3: Wavelet spectrum, Test 1, lower-mid thermocouple, plane 'C' pass 3..	134
Figure D-4: Wavelet spectrum, Test 1, bottom thermocouple, plane 'C' pass 3	134
Figure D-5: Wavelet spectrum, Test 3, upper-mid thermocouple, plane 'C' pass 2..	135
Figure D-6: Wavelet spectrum, Test 3, lower-mid thermocouple, plane 'C' pass 2..	135
Figure D-7: Wavelet spectrum, Test 3, bottom thermocouple, plane 'C' pass 2	136
Figure D-8: Wavelet spectrum, Test 4, lower-mid thermocouple, plane 'C' pass 2..	137
Figure D-9: Wavelet spectrum, Test 4, bottom thermocouple, plane 'C' pass 2	137
Figure D-10: Wavelet spectrum, Test 5, lower-mid thermocouple, plane 'C' pass 1..	138
Figure D-11: Wavelet spectrum, Test 5, bottom thermocouple, plane 'C' pass 1	138

List of Symbols

Symbols	Description	Units
C	Normalized concentration	
C_p	Heat Capacity	(kJ/kg·K)
dx	normalized discretation length	
D	Diffusion coefficient	(m ² /s)
\vec{e}	unit vector	
exp	exponential constant	
g	Gravitational constant	(m/s ²)
Gr	Grashof number	
h	Heat transfer coefficient	(W/m ² ·K)
H_f	Heat of formation	(kJ/kg)
k	Separation coefficient	
K	Heat conductivity	(W/m·K)
ℓ	Normalized zone length	
L	Characteristic length	(m)
M	Number of elements in a control volume	
Ma	Marangoni number	
n	Pass number	
Nu	Nusselt number	
p	Pressure	(Pa)
Pe	Peclet number	
Pr	Prandtl number	

q	q element number in a discretized length	
Ra	Rayleigh number	
Re	Reynolds number	
Sc	Schmidt number	
St	Stefan number	
t	Time	(s)
T	Temperature	(K)
V	Interface velocity	(m/s)
x	Distance along the length of the bar	(m)
X	Ingot length	(m)
Y	Zone depth	(m)
Z	Zone width	(m)
α	Thermal diffusivity	(m ² /s)
β	Expansion coefficient	(K ⁻¹)
δ	Boundary layer thickness	(m)
ρ	Density	(kg/m ³)
σ	Surface tension	(N/m)
μ	Dynamic viscosity	(kg/m·s)
ν	Kinematic viscosity	(m ² /s)
u	Fluid velocity	(m/s)

Subscripts	Description
c	Critical
D	Diffusion
eff	Effective
I	Interface
L	Liquid
m	Momentum
n	Pass number
o	Initial
s	Solid
T	Thermal
*	Theoretical
x	axial direction
y	vertical direction
z	horizontal direction

Chapter 1 Introduction

This chapter contains a description of the zone refining process and overview of typical applications. The capabilities of the process are discussed as well as the underlying mechanisms behind separation. In addition, a framework for studying zone refining is discussed.

1.1 General Description of Zone Refining

Zone refining was developed in the 1950's by Pfann [1] and has since been applied to purify a broad range of materials such as semiconductors [2], pure metals [3], and organic crystals [4] to ultra low impurity levels. It is used as an intermediary step in semiconductor production such as indium antimonide [5], germanium [6], and antimony [7] for infrared detectors [8] and windows [9]. Typical operating targets would be to upgrade feedstock purity three or four orders of magnitude [10] from around 99.999% [11] to 99.999999% [2] prior to Czochralski single crystal growth. These high purity levels are necessary for good electronic properties as well as for ease in single crystal growth [5]. Although there are several forms of zone refining such as vertical float zone [12] and horizontal Bridgman methods [13], the fundamental separating mechanism is common. Separation is based upon a solubility difference between solid and liquid phases resulting in segregation at a solid/liquid interface. As an analogy, distillation utilizes a difference in volatility of substances between liquid and gaseous phases [14].

A detailed description of the theory and practical considerations of zone refining is given in the *Handbook of Crystal Growth* [15] and *Zone Melting* [16]. Typical

operation of zone refining equipment consists of a bar of around 1 to 2 metres in length contained in an inert atmosphere. As shown in Figure 1-1, the process involves melting a portion of the ingot using resistance heaters and slowly moving this molten zone down the bar length at approximately 60 millimetres per hour [17].

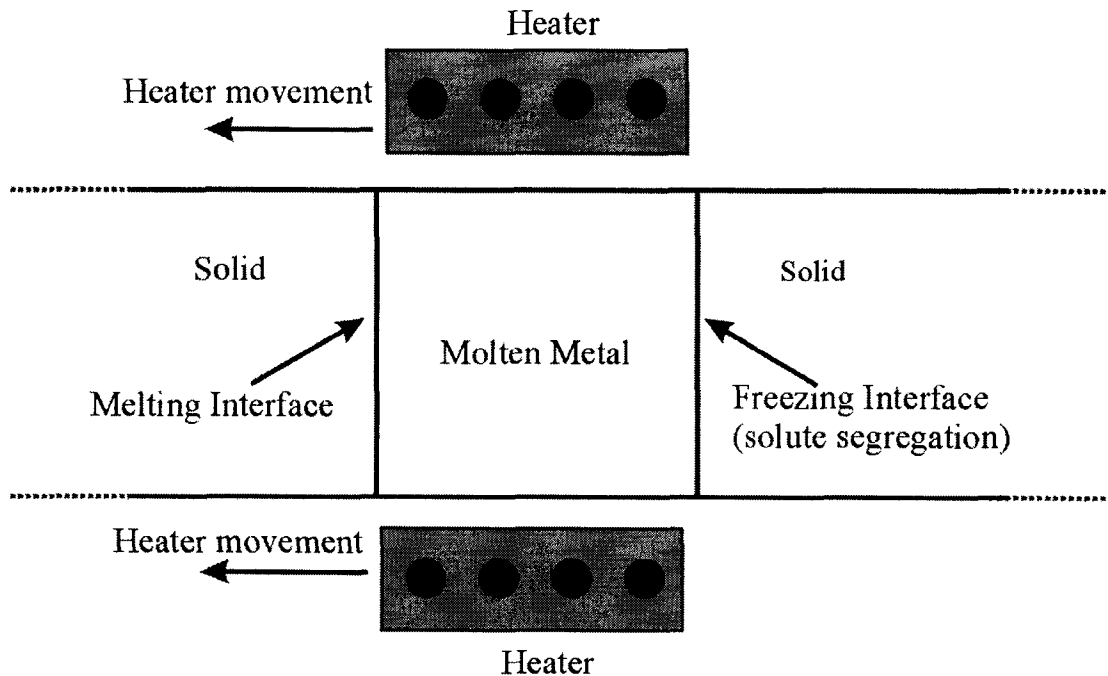


Figure 1-1: Zone refining schematic

Due to a solubility difference between liquid and solid phases, impurities are redistributed to either end of the ingot via segregation at the freezing interface. Impurities with higher solubility in the liquid accumulate in the molten zone while those with a higher solubility in the solid are depleted in the molten zone. The end result is a redistribution of impurities along the length of the ingot. The ends of the ingot are then cropped off and recycled, while the purer centre portion is retained.

In order to design operating procedures for the zone refining process, knowledge of the movement of impurities is essential. The most important parameter is the

segregation rate at the freezing interface. Section 1.2 contains a description of the driving force for this segregation, and how it can be calculated.

1.2 Driving Force for Segregation

The driving force behind this segregation is the thermodynamic difference of impurity solubility between the solid and liquid phases, and is described by the separation coefficient (k). The theoretical value of k can be calculated from a typical binary phase diagram as the ratio between the impurity concentration at the liquidus and solidus at an isothermal condition. This is demonstrated in Figure 1-2 for a system where the impurity lowers the melting temperature. Here, the separation coefficient is less than 1 and impurities are more soluble in the liquid than the solid. The opposite is true for an impurity that raises the melting point. As the value of k gets further away from unity, the thermodynamic driving force for separation is enhanced.

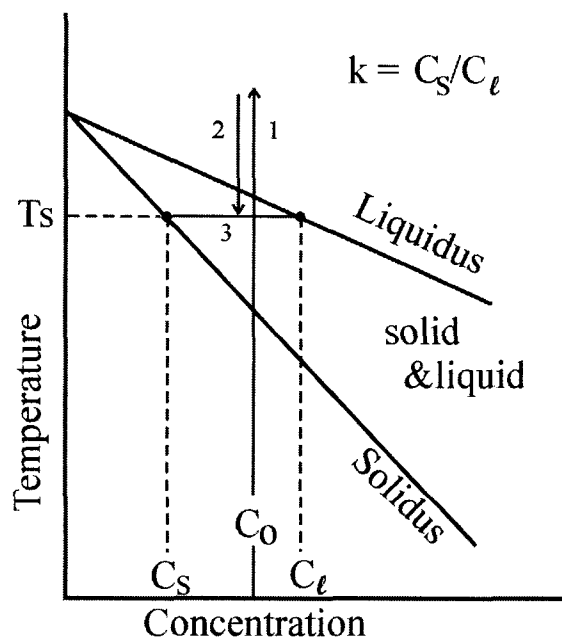


Figure 1-2: Dilute Binary Phase Diagram

Solubility does vary between different impurities and is based upon several molecular phenomena. For example, atoms that are much smaller than the matrix material typically exhibit substantial solubility because they are able to fit in the interstitial vacancies within the crystal lattice. Because of this high solubility, these atoms typically segregate very slowly [2]. The opposite is true for atoms that are much larger than the matrix material. Other phenomena that contribute to solubility include Van der Waals forces, electrostatic forces, and chemical interaction between elements. For example, one approach to target an impurity with k close to unity is to introduce an element with which it will form a compound [18][7][19][20][21]. The object of this approach is to find additives and a resulting compound that are removed easily. Although this subject is beyond the scope of this thesis, it has received little attention in literature and is possibly a fruitful area of study as suggested in Section 6.2.

The segregation coefficient is quite often assumed to be independent of concentration. This is justified by the assumption that, in most applications, impurity levels are very dilute and therefore follow Henry's law [22] indicating that the liquidus and solidus lines are linear.

1.3 Statement of Problem

Although the purifying potential of zone refining is impressive, the process is time consuming for which an ingot of 20 kg with 70% yield would take approximately one week¹. Unfortunately the rate of the melting and freezing cycle is limited by the transport processes, dictating a slow zone travel rate. In addition, multiple passes are

¹ Based upon typical operating procedures at Firebird Technologies Inc.

required to achieve sufficient purity. Thus to reduce the time to purify an ingot, various furnaces are used along the ingot length. Depending on the material to be purified and the impurity, anywhere from nine [23] to one hundred [24] passes of the molten zone are employed. In addition, the process consumes a lot of energy due to heat loss between liquid metal and the surroundings. Therefore an improvement in separation efficiency has the potential of substantially reducing processing time and energy consumption with existing equipment. Alternately, achieving higher purity products from zone refining makes it possible to produce higher quality single crystals during Czochralski crystal growth [5]. A combination of these effects would contribute to an increase in productivity of semiconductor wafers with less expense and higher quality.

1.4 Outline of Thesis

The main goal of this thesis is to understand how to improve separation efficiency of the zone refining process by studying its transport processes. It is organized into the following six chapters:

- Chapter 1: Zone refining is introduced by discussing the fundamental separation mechanism and typical applications of the process.
- Chapter 2: Analysis of the transport phenomena which contribute to the segregation of impurities is provided, and a summary of mass balance models found in literature are discussed.
- Chapter 3: Experiments designed to characterize convection currents within the molten zone, and measure the final impurity profiles after zone refining are described.

- Chapter 4: A discussion of the experimental data is provided.
- Chapter 5: A relationship between convection currents and separation efficiency is documented.
- Chapter 6: Conclusions are summarized and areas of possible future work are outlined.

Chapter 2 Process Modeling and Analysis

Although the driving force for segregation is based upon the theoretical solubility difference between liquid and solid, mass transport can drastically influence the properties of the system. In order to account for these effects, the actual segregation rate is represented by the effective segregation coefficient (k_{eff}). Studying the significant transport phenomena that contribute to segregation is crucial to understanding how to improve the zone refining process. This section will describe how the movement of impurities is influenced by initial concentration, zone length, diffusion, convection, and interface growth rate. A discussion of the system assumptions is also provided.

2.1 Impurity Distribution Models

Using a mass balance around the molten zone, it is possible to estimate the final impurity distribution within the ingot after zone refining. Many models have been derived based upon the pioneering mathematics of Lord [25] and Reiss [26], which calculate the concentration profile based upon the separation coefficient, ingot length, zone length and initial concentration. In this section, these mass balance equations are presented in a discretized format [27] so that they are easily programmed on computer. The model shows that, as the molten zone moves down the length of the ingot, impurities either accumulate ($k < 1$) or are depleted ($k > 1$) in the liquid resulting in a shift of the impurity profile within the ingot. Using an analysis of these mass balance models, variables contributing to the mechanism of separation will be identified, and the assumptions and boundary conditions will be evaluated. In

addition, the equations will be used to calculate the separation efficiency of zone refining experiments in Section 4.4.1.

A popular set of boundary conditions first described by Scheil [28] assumes negligible back diffusion in the solid and perfect mixing in the molten zone. It is reasonable to neglect back diffusion because the solid diffusion coefficients are typically 3 orders of magnitude less than that of the liquid diffusion coefficient [29][18][25]. Although the assumption of perfect mixing will be maintained for the mass balance equations, it has shortfalls and will be discussed later in this section.

Considering that the zone length is much smaller than the ingot length, there are three distinct regions with different boundary conditions [30]. In the first region, prior to the appearance of the freezing interface, the heater advances onto the ingot and melts the front of the bar. The solutes are assumed to be uniformly mixed throughout the molten material by the stirring effect of the molten metal. Equation (2-1) averages the concentration within the first zone length and computes solid concentration upon the appearance of the freezing interface at the beginning of the bar ($x=0$).

$$\text{At } x=0 \quad C_0^n = k \left(\frac{dx}{\ell} \right) \left(\sum_{q=0}^{M-1} C_q^{n-1} \right) \quad (2-1)$$

Where x is the position of solid/liquid interface (fraction of ingot length); dx is the normalized discretation length; q is the index of discretized length ($x=q \cdot dx$); ℓ is the normalized zone length (as a fraction of ingot length); M is the number of elements in

zone length ($M = \ell/dx$); n is the pass number; k is the separation coefficient; C is the normalized concentration.

Throughout the middle of the bar, material enters the molten zone via the melting interface and exits via the freezing interface. The accumulation of impurities within the zone is based upon the difference between the concentration of impurity atoms leaving and entering the zone. Once again, the impurity content is assumed to be homogeneous within the zone. These boundary conditions are consistent from the beginning of the bar until the melting interface reaches the bar's end as shown in Equation (2-2).

$$\text{At } 0 \leq q \cdot dx \leq (X - \ell) \quad C_q^n = C_{q-1}^n + \frac{k \cdot dx}{\ell} (C_{(q+M-1)}^{n-1} - C_{q-1}^n) \quad (2-2)$$

Where the additional variable X is the normalized ingot length ($X=1$).

When the heater reaches the end of the ingot, the melting interface disappears and the volume of the zone decreases until the freezing interface reaches the end of the bar. Within this region, the concentration in the zone is given by the difference between the initial solute concentration C_0 uniformly distributed throughout the sample, and the corresponding solute concentration incorporated in the solidified profile as shown in Equation (2-3).

$$\text{At } (X - \ell) < q \cdot dx \leq X \quad C_q^n = k \left(C_0 - dx \sum_{q=0}^{q-1} C_{(q)}^n \right) \quad (2-3)$$

Zone refining does not remove impurities from the ingot but redistributes them along the length of the ingot. As suggested in Section 1.1, multiple passes are applied to the

ingot in order to improve the overall distribution. Each successive pass has a lower impact on the concentration profile until a negligible effect is reached, known as the ultimate distribution [31][32]. In a host of published papers, a number of different optimization techniques were used to calculate how impurity distribution could be improved by selecting proper zone length [33][34][35][36], number of passes [37], and varying cross section [38]. A demonstration of how variation of the zone length influences the concentration profile is given below in Figure 2-1 as calculated by the mass balance model provided in this section.

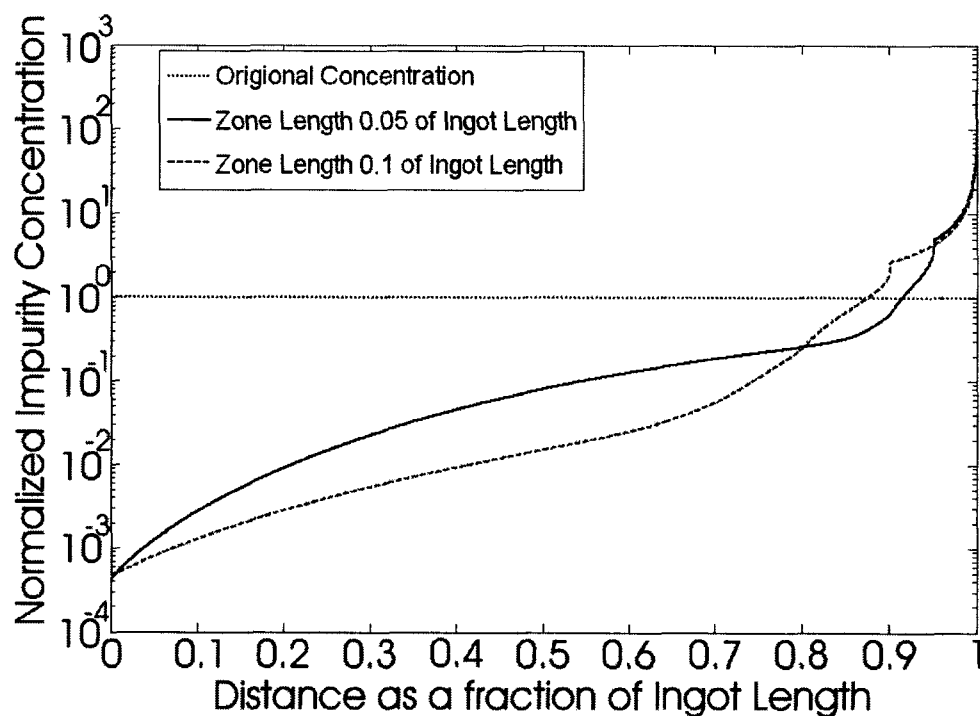


Figure 2-1: Impurity distribution for different zone lengths, $k=0.3$, $n=10$ passes

The mass balance model is a good tool for demonstrating several important zone refining concepts such as the influence of zone length, ingot length and separation coefficient; however, it employs some assumptions that represent an idealized system. One of the primary assumptions in this model is that convection in the molten zone is thorough and uniform. This implies that there is perfect mixing within the zone, no

concentration gradients at the freezing interface, and a constant separation coefficient. Conversely, it has been found that a concentration boundary layer exists adjacent to the interface whose shape is highly dependent on the rate of liquid diffusion, interface velocity, and the stirring conditions within the zone [39]. In fact, convection plays a dominant role in heat transfer and transport of species. In consequence, the assumptions of the mass balance model are inadequate, limiting the function of the model as a predictive tool [40] for estimating how changes in process variables will affect the concentration profile. In order to improve separation efficiency and understand how operating conditions might influence the zone refining process, a detailed analysis of the transport phenomena is required. The following section will provide an analysis of the most important transport phenomena and show how impurity separation is influenced by heating conditions, ingot geometry, fluid properties, and interface velocity.

2.2 Governing Equations

While the driving force for segregation is a solubility difference between solid and liquid, mass transport is responsible for movement of impurities ahead of the freezing interface. One criterion that is essential for the segregation is that mass transport of impurities must be faster than the interface travel rate. If not, the impurities would be trapped in the advancing solid for $k < 1$, or a concentration gradient would not be established at the interface for $k > 1$. In either case, there would be little to no segregation.

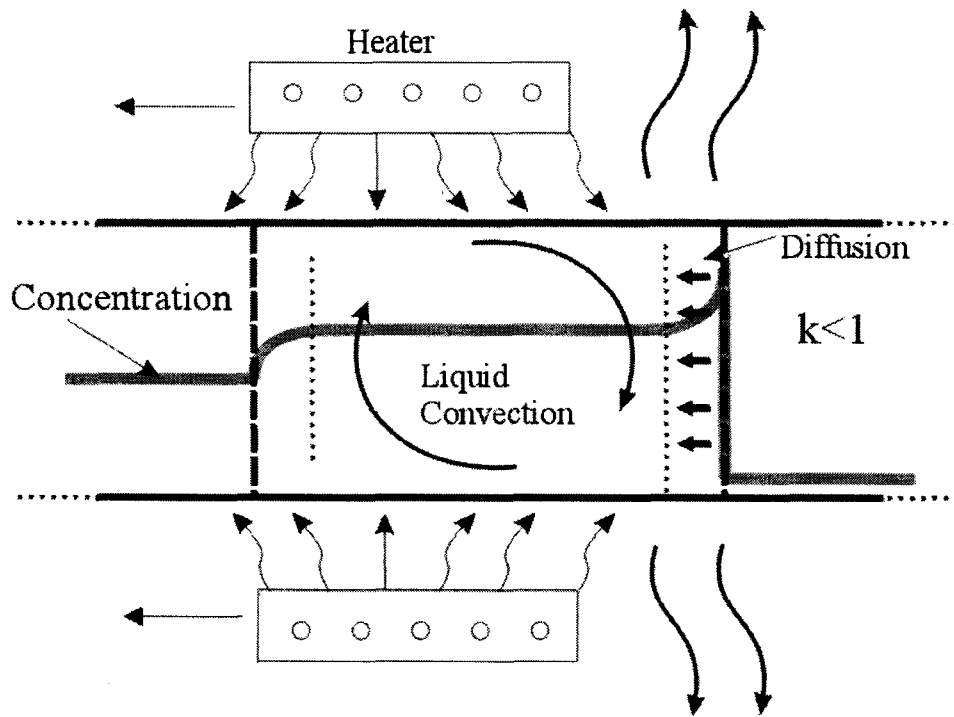


Figure 2-2: Schematic of the Molten Zone for $k < 1$

The important transport phenomena that occur within the molten zone are represented in a schematic of the molten zone in Figure 2-2 ($k < 1$). The grey line represents the concentration gradient while the dark dotted lines represent the melting (left) and freezing (right) interfaces. A common assumption in fluid dynamics models is the presence of a non-slip boundary condition, where the fluid velocity approaches zero at the interface because of friction [41]. The location where fluid velocity is 99% of the bulk velocity is defined as the boundary layer thickness (δ_m), represented by the light dotted lines. The width of this boundary layer is dependent on the fluid velocity, viscosity of fluid, and interface velocity. As fluid velocity decreases, diffusion plays a more significant role in mass transport. At a critical distance from the interface, mass transport is purely diffusive, determined by the Peclet number in Section 2.3.4. Note that fluid velocity is common in equations 2-4, 2-5, 2-6, and 2-7 indicating that momentum, thermal, and mass transport are all interrelated.

$$\rho_0 \left(\frac{\partial \bar{v}}{\partial t} + \bar{v} \cdot \nabla \bar{v} \right) = -\nabla p + \mu \nabla^2 \bar{v} + \rho_0 g \beta_T (T_0 - T) \bar{e}_y \quad (2-4)$$

$$\nabla \cdot \bar{v} = 0 \quad (2-5)$$

$$\left(\frac{\partial T}{\partial t} + \bar{v} \cdot \nabla T \right) = \alpha \nabla^2 T \quad (2-6)$$

$$\left(\frac{\partial C}{\partial t} + \bar{v} \cdot \nabla C \right) = D \nabla^2 C \quad (2-7)$$

Where ∇ is the gradient operator; v (m/s) is the fluid velocity; p (Pa) is pressure; μ (kg/m·s) is the viscosity; T (K) is the temperature; α (m²/s) is the thermal diffusivity; D (m²/s) is the solute diffusivity; β_T (K⁻¹) is the thermal expansion coefficients of the liquid; \bar{e} is the unit vector in the direction of gravity.

From these equations, it can be observed that fluid movement is driven by density variations in the fluid due to thermal buoyancy as described in the final term of Equation (2-4). As shown in Section 2.3.1, thermocapillary flow can also contribute to convection via surface tension gradients caused by surface temperature gradients. The boundary conditions for surface tension flow are summarized in Brown et al. [40]. Convection due to concentration differences is negligible in pure metals because typical concentrations are extremely low [42].

2.3 Dimensional Analysis

The complexity of the zone refining system makes it difficult to recognize the most important factors that influence segregation. In order to try and identify the dominant mass transport phenomena without solving the transport equations (2-4 to 2-7) with appropriate initial and boundary conditions, important information can be inferred

from dimensionless numbers. The purpose of this exercise is to provide means to calculate the approximate magnitude of convection, and identify all the important variables for segregation. For example, a description of the Grashof number shows that temperature gradients and enclosure dimensions are important for fluid movement, and a modified Peclet number shows how the rate of segregation is dependent on fluid velocity, diffusion rate, and interface travel rate. Table 2-1 includes the dimensionless numbers relevant to zone refining followed by a discussion of each.

Table 2-1: Dimensionless numbers relevant to the zone refining system

Name	Meaning	Definition
Grashof	$\frac{\text{buoyancy force}}{\text{viscous force}}$	$Gr = \frac{g \cdot \beta_T \cdot L^3 \cdot \Delta T}{\nu^2}$
Marangoni	$\frac{\text{surface tension forces}}{\text{viscous forces}}$	$Ma = \frac{(d\sigma/dT)L \cdot \Delta T}{\alpha \cdot \mu}$
Rayleigh	$\frac{\text{buoyancy force}}{\text{viscous force}}$	$Ra = Gr \cdot Pr$
Prandtl	$\frac{\text{viscous diffusivity}}{\text{thermal diffusivity}}$	$Pr = \frac{\nu}{\alpha}$
Schmidt	$\frac{\text{viscous diffusivity}}{\text{species diffusivity}}$	$Sc = \frac{\nu}{D}$
Peclet	$\frac{\text{convective species transport}}{\text{diffusive species transport}}$	$Pe = \frac{v \cdot L}{D}$
Reynolds	$\frac{\text{inertial forces}}{\text{viscous forces}}$	$Re = \frac{v \cdot L}{\nu}$
Stefan	$\frac{\text{heat of transformation}}{\text{heat capacity}}$	$St = \frac{H_f}{C_p \cdot \Delta T}$
Nusselt	$\frac{\text{convective heat transfer}}{\text{conductive heat transfer}}$	$Nu = \frac{h \cdot L}{K}$

2.3.1 Grashof and Marangoni Numbers

Convection is the common variable in all 4 transport equations and therefore plays a major role in both the thermal and solute transport within the system. As

demonstrated in Equation (2-4), the fluid movement is driven by buoyant forces, which result from thermal gradients. These forces are typically characterized using the Grashof number which represents a ratio between buoyancy versus viscous forces. For example, the higher the Grashof number, the higher the driving force for fluid movement. In addition, temperature gradients on the surface of the fluid cause surface tension gradients. For example, surface tension decreases as temperature increases, providing a driving force for surface fluid to move towards regions of lower temperature. The Marangoni number characterizes the ratio of surface tension forces versus viscous forces; the higher the Marangoni number, the higher the driving force for surface tension flow. Note that characteristic length, temperature gradients, and material properties are the principle variables in both numbers. As the Grashof and Marangoni numbers suggest, convection increases with size of the enclosure and temperature gradients. It should also be pointed out that the characteristic distance is to the third power in the Grashof number therefore convection is much more dependent on geometry than temperature gradient.

2.3.2 Prandtl and Schmidt Numbers

The Prandtl and Schmidt numbers are derived from molecular diffusivity constants and are therefore formed from physical properties of the melt. The Prandtl number is a ratio of the dissipation of momentum to the diffusion of heat and is a measure how easily convection will evolve in a fluid. For example, the ratio of thermal (δ_T) to momentum (δ_m) boundary layer thicknesses at a stationary interface is related to the Prandtl number using the correlation found in Equation (2-9) [41].

$$\frac{\delta_T}{\delta_m} \doteq \text{Pr}^{-1/3} \quad (2-8)$$

At low Prandtl numbers, such as the case with molten semiconductors (0.1-0.01) [40], fluid flow develops readily. These fluids are more likely to experience time dependent or turbulent convection compared to higher Prandtl number fluids.

According to Equation (2-7), both diffusion and convection contribute to mass transport. As represented in Figure 2-2, there is a concentration gradient at the freezing interface whose shape and thickness is dependent on the diffusion rate, convection currents, and interface velocity. Given that diffusion is analogous to heat transfer, the ratio of the diffusion boundary layer thickness (δ_D) versus the momentum boundary layer (δ_m) at a stationary interface is related to the Schmidt number in Equation (2-10) [47]. The lower the Schmidt number (1-10 for solutes in semiconductors [40]), the faster impurities diffuse into the fluid stream. Convection is faster than diffusion, and since an overlap of these boundary layers would encourage more convective mass transport, segregation would be enhanced.

$$\frac{\delta_D}{\delta_m} \doteq Sc^{-1/3} \quad (2-9)$$

2.3.3 Rayleigh Number

The Rayleigh number is calculated by multiplying the Grashof number by the Prandtl number and can be used to determine the magnitude of convection. The Rayleigh number indicates the likelihood of natural convection for zone refining of lead. According to Incropera and DeWitt, significant convection occurs when $Ra > 1708$ [43]. Using the material properties of lead in Table 2-2, convection will be significant when the temperature gradient exceeds 0.123 K.

$$Ra = \frac{g\beta L^3 \Delta T}{\alpha \nu} > 1708 \quad \text{when } \Delta T > 0.123K \quad (2-10)$$

Table 2-2: Material Properties of Pb at T=600.5K [44][45]

Pr=0.026	Prandtl Number
Y=0.03 m	Common Zone Depth
$\beta = \frac{-\partial\rho/\partial T}{\rho} = \frac{-1.3174 \times 10^{-3} \text{ g} \cdot \text{cm}^{-3} \text{ K}^{-1}}{10.678 \text{ g} \cdot \text{cm}^{-3}} = 1.2337 \times 10^{-4} \text{ K}^{-1}$	Expansion Coefficient
$\nu = \frac{\mu}{\rho} = \frac{2.65 \times 10^{-3} \text{ N} \cdot \text{s} \cdot \text{m}^{-2}}{10678 \text{ kg} \cdot \text{m}^{-3}} = 2.48 \times 10^{-7} \text{ m}^2 \text{ s}^{-1}$	Dynamic Viscosity
$\alpha = \frac{K}{\rho C_p} = \frac{15.4 \text{ W} \cdot \text{m}^{-1} \text{ K}^{-1}}{10678 \text{ kg} \cdot \text{m}^{-3} 152 \text{ J} \cdot \text{kg}^{-1} \text{ K}^{-1}} = 9.49 \times 10^{-6} \text{ m}^2 \text{ s}^{-1}$	Diffusivity of Heat
g=9.804 m/s ²	Acceleration of Gravity

A reasonable assumption for zone refining would be that, since convection occurs at such a low temperature gradient, there will always be significant convection in the system. Common temperature gradients for semiconductor melts are around (8-19 K/cm [46]) in literature. In addition, the complexity of the temperature field even in the most carefully designed crystal growth systems leads to both vertical and horizontal temperature gradients in the melt [40]. As a result, buoyant flow is always present.

2.3.4 Peclet Number

Another tool for comparing the significance of convection over diffusion is the Peclet number as described in Table 2-1. The Peclet number identifies whether convection is dominant over diffusion based upon the fluid velocity, the diffusion coefficient, and

size of enclosure. Based on this ratio, valuable information about the rate of segregation can be inferred. For example, Peclet numbers above 1 dictate that transport is diffusion controlled [48]. Since diffusion is normally much slower than convection, relatively poor separation would occur. Although the Schmidt and Peclet numbers are valuable for indicating whether diffusion or convection will be dominant, this analysis is not complete since they do not incorporate a moving interface. A modification of the Peclet number, as derived below, accounts for a moving interface and is a measure of the cooperation between convection and diffusion.

In a classic paper by Tiller et al.[49], an expression was derived for a diffusive concentration profile in the absence of convection. This expression, as given in Equation (2-11), is a function of interface velocity, diffusion rate, and distance from the solidifying interface.

$$C_L = C_I \exp\left(\frac{-Vx}{D}\right) + C_0 \quad (2-11)$$

Where C_L is the liquid concentration profile in the boundary layer; C_I is the liquid concentration at the interface ($C_a=k \cdot C_0$); C_0 is the bulk concentration outside of the boundary layer; V (m/s) is the interface travel rate; D (m^2/s) is the liquid diffusion coefficient; x (m) is the distance from the freezing interface.

According to Equation (2-11), the concentration profile decomposes exponentially as a function of distance from the interface. Figure 2-3 demonstrates how the characteristic diffusion boundary layer is inversely proportional to growth rate. For

simplicity, a characteristic distance (D/V) is defined as the point where C_L has fallen below C_0+C_L/\exp [49].

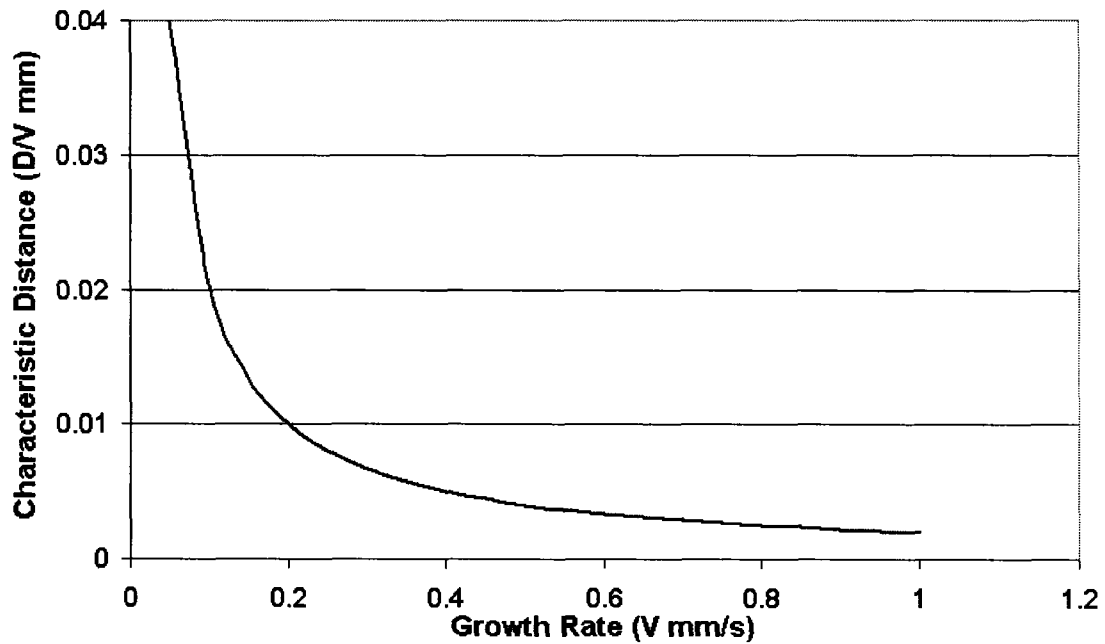


Figure 2-3: Characteristic Distance (D/V) as a function of the growth rate.

This calculation is important for demonstrating the effect of growth rate on diffusion. If combined with information about the fluid velocity boundary layer thickness, the overall mass transport due to convection and diffusion can be characterized. If the momentum boundary layer thickness (δ_m) is substituted for x in Equation (2-11), the exponential term resembles the Peclet number. The difference is that this modified Peclet number is based on the interface velocity instead of fluid velocity.

$$Pe_s = \frac{V\delta_m}{D} \quad (2-12)$$

Where V (m/s) is the interface velocity, δ_m (m) is the momentum boundary layer thickness, and D (m^2/s) is the liquid diffusion coefficient.

The magnitude of the modified Peclet number gives an indication of the synergistic contribution of diffusion and convection to mass transport. The smaller the Peclet number, the more interaction between the convection and diffusion transport mechanisms, and the better the segregation. For example, as shown on Figure 2-4 a small Peclet number (B) represents a large diffusion boundary layer thickness (δ_D) relative to a thin momentum boundary layer thickness (δ_m). Note that the diffusion boundary layer thickness is a hypothetical distance and the actual concentration profile would be influenced by both diffusion and convection. Using this relationship, it can be inferred that a decrease in interface velocity, an increase in diffusion rate, or an increase in stirring rate would reduce the Peclet number and enhance the segregation process [50]. The segregation rate is best for scenario B depicted in Figure 2-4.

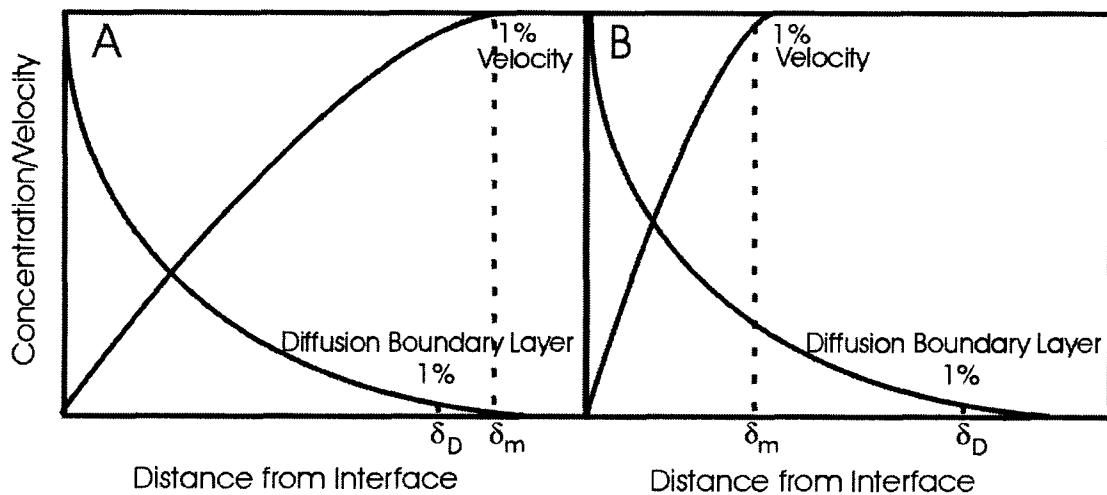


Figure 2-4: Hypothetical momentum and concentration boundary layer thicknesses for $Pe_A > Pe_B$.

2.4 Calculating the Segregation Rate

The relationship between interface velocity, convection currents, diffusion rate, and separation efficiency was hypothesized in a seminal paper by Burton, Prim, and

Schlichter (BPS) [51]. They defined the expression in Equation (2-13) to calculate the effective separation coefficient k_{eff} based on a hypothetical stagnant film thickness. The basis of stagnant film theory is the assumption that there is a stagnant region (δ^*) adjacent to the freezing interface where mass transfer is entirely diffusive. In addition, beyond this stagnant region, the mass transport is assumed to be entirely convective. Note the similarity between the parameter Δ and the Peclet number described above in Equation (2-12).

$$k_{eff} = \frac{k}{k + (1 - k)e^{-\Delta}} \quad , \quad \text{where } \Delta = \frac{V\delta^*}{D} \quad (2-13)$$

Where k is the theoretical distribution coefficient; k_{eff} is the effective distribution coefficient; V (m/s) is the interface velocity; D (m²/s) is the liquid diffusion coefficient; δ^* (m) is the hypothetical stagnant film thickness.

As demonstrated in Figure 2-5, the concentration within the stagnant region is linear while outside this layer the concentration is assumed to be perfectly mixed. This stagnant region is assumed to be constant length throughout the interface cross section, and independent of time. The purpose of these assumptions is to provide simple boundary conditions to solve the mass transport equations. The stagnant film thickness represents a hypothetical, equivalent film thickness that emulates the segregation rate of the system.

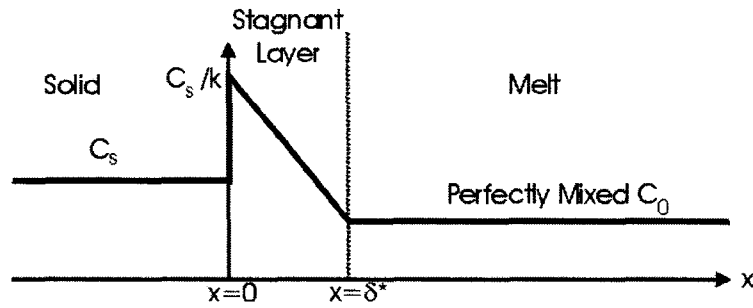


Figure 2-5: Stagnant film in solute transport during melt growth.

2.5 Deficiencies of the Burton, Prim, and Schlichter Theory

The BPS theory has been quite successful at modeling the characteristics of separation, and has been highly praised in literature. However, there are also well known deficiencies [40]. Contrary to stagnant film theory, experimental and theoretical studies have shown that there is a non-linear velocity profile that approaches zero near the freezing interface [52]. BPS theory requires an empirical value of δ^* or δ^*/D based upon experimental or computational data. This may be estimated by directionally freezing an ingot and fitting the concentration profile to the mass balance model in Section 2.1. Unfortunately, in order for the theory to be predictive, prior empirical knowledge the system is required. In addition, it is generally assumed that δ^* is independent of the interface velocity in order to simplify calculations for many applications. Wilcox [53] showed that this is not necessarily true by proving that δ_m/δ^* is a function of V/D and the Schmidt number.

Numerous attempts have been made to extend the BPS theory by including convection within the solute layer, accommodating a dynamic interface velocity, and providing a physical basis behind the boundary layer thickness [47][54][55][56][57]. Also, numerical analysis has been done to calculate the boundary layer thickness in

several ideal geometries [58][48]. An analysis of physical phenomena in a practical sense shows how the assumptions are imperfect and may play an important role in segregation. These phenomena include varying boundary and thermal conditions, and fluid flow effects.

2.5.1 Varying Boundary Conditions

As suggested in Section 2.4, the BPS model assumes a constant boundary layer thickness. Due to the geometry of the molten zone, it is not likely that fluid velocity is constant throughout the cross section of the interface [47]. This would result in varying concentration boundary layer thicknesses as represented in Figure 2-6 and varying separation characteristics across the cross section.

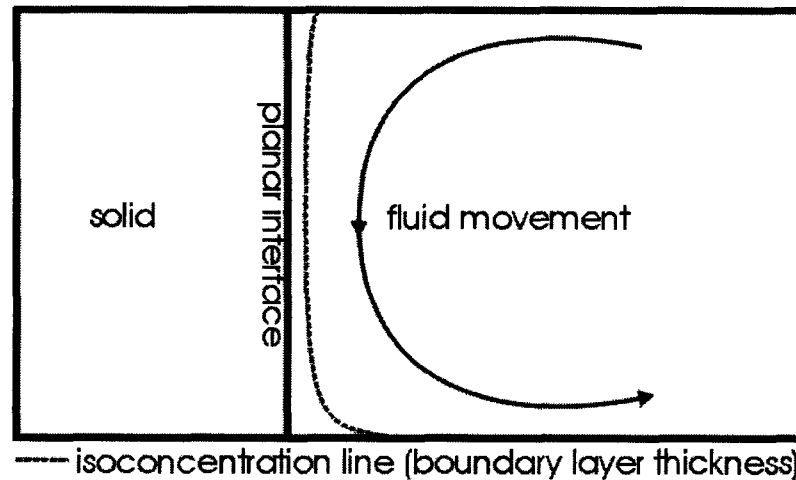


Figure 2-6: Non uniform solute layer thickness due to inhomogeneous bulk fluid velocity.

2.5.2 Varying Thermal Conditions

In addition to varying boundary layer thickness, it is quite probable that boundary conditions vary in different positions within the bar. For example, temperature gradients within the zone are dependent on the surrounding external temperature gradients. While the zone closest to the end of the bar has only one neighboring zone,

a zone near the middle of the bar would have two neighbors. Because of the different thermal conditions, stirring conditions are likely to be different between the two scenarios. This would result in an unforeseen change in segregation rate as a function of location within the bar. With this in mind, it would be difficult to calculate the segregation rate based upon the BPS model without a thermal model of the system.

2.5.3 Fluid Flow Effects

In Section 2.3.4 it was suggested that an increase in fluid flow enhances mass transport adjacent to the freezing interface. In combination with a slow, steady interface velocity, this results in improved segregation. Although this relationship is true in a laminar flow regime, it has been shown that more complex fluid flow regimes such as oscillatory or turbulent flow can cause perturbations in fluid velocity and the heat transfer rate [59]. One assumption in the BPS model is that there is a planar interface with a constant velocity. On the contrary, temperature perturbation at the interface can cause instability in the freezing rate [60]. Studies show that while the macroscopic interface velocity is typically constant and equal to the heater velocity, the microscopic interface velocity can be as much as 20 times higher in the presence of temperature oscillations [39][46][61]. These oscillations are characterized as rapid growth of the interface associated with super cooling, and a successive release of heat which stops the freezing [39]. As further evidence, the period of temperature fluctuation typically coincides with striations in the concentration [56]. These striations can be used as a strong visual indication of the interface velocity oscillations and have been studied extensively in literature [62]. Correlations for the interface velocity as a function of period and amplitude of thermal oscillations have

been found [63]. Since boundary conditions typical of crystal growth and zone refining commonly result in time dependent fluid regimes where no steady state is reached [57], a model to calculate a constant value for k_{eff} is probably not realistic. A complete model must take time dependent fluid flow effects into account.

While it is well known that oscillations cause microscopic striations in the impurity profile, there is some controversy considering the effects on macro segregation. Several authors have published numerical and experimental work with inconsistent conclusions. For example, Kim et al. [64] established that segregation is controlled by the microscopic interface growth rate while convection induced boundary layer perturbations is a second order effect. A transition was found where the segregation went from an erratic concentration profile during turbulence to a monotonic increase in concentration during laminar flow. On the other hand, slightly different conclusions were presented by Holmes et al. [65] who suggested that macro segregation is controlled by the boundary layer thickness under both laminar and turbulent flow. This implies that stirring should be increased indefinitely to improve separation. Numerical models by Wilson [66] and Van Run et al. [67] estimate that significant back melting under high turbulence can provide marked improvement in separation. They suggest that, under varying segregation rates, if the peak concentration of the striation can be melted off and reincorporated into the melt, k_{eff} can be enhanced beyond the thermodynamic limit. Experimental evidence to support this model was not provided and practical considerations for zone refining are not

discussed. Because of the contradicting results in literature, it is unknown whether oscillations will increase or decrease the macro segregation rate.

2.6 Summary of Process Modeling and Analysis

This chapter contained a discussion of the important phenomena for segregation during zone refining. It was found that most models for calculating the impurity profile depend on incorrect assumptions. These assumptions include perfect mixing within the zone, constant boundary layer thickness, and constant interface velocity. Most importantly, as shown in Section 2.5.3, there is conflicting evidence for the effects of convection on separation efficiency. It is not clear whether complex convection regimes are detrimental to macro segregation.

In order to challenge the contradictions in literature, it is essential to find a relationship between the convective conditions of the system and segregation. An accurate calculation for a time dependant value of k_{eff} would require a detailed understanding of the thermal and other boundary conditions. Specifically, an experimental regime is valuable for determining whether convection characteristics can be influenced by process operation or design. In order to improve the current process, it is essential to identify which fluid flow regimes are achievable, and isolate the best fluid flow conditions for segregation. The following chapter will describe experimental techniques to measure the temperature field for characterizing convection and assay tests for measuring segregation rates under different boundary conditions.

Chapter 3 Experimental Procedures

A series of experiments were completed on industrially scaled equipment at Firebird Technologies. The purpose of these experiments was to produce an array of fluid dynamic effects to study the mechanisms of transport. This is done by correlating separation efficiency to convection characteristics for various operating conditions. The experiments were split into two stages, the first being a thermal profiling of the molten zone. These experiments involved thermocouples, in direct contact with the melt, for measuring the temperature field. Convection within the molten zone was characterized using the temperature data. The second stage of experiments involved chemical analyses using glow dispersion mass spectrometry to measure separation efficiency. All experiments were done on lead metal because of its relatively low cost, similar physical properties to semiconductor materials, and the availability of thermodynamic data in literature [20]. This chapter describes the equipment and experimental procedures for both the thermocouple and assay tests.

3.1 Zone Refining Machine

This section describes the zone refining machine at Firebird Technologies. All experiments were done on existing industrially scaled equipment. One of the advantages to this approach is that the results from this study are directly transferable to industry.

The zone refining apparatus consists of a stationary cylindrical quartz boat (1.56 metre length by 116 millimetre inner diameter) held in a quartz tube. High purity quartz is used because of its high strength and to prevent contamination of the lead

due to leaching at high temperatures. An assembly of 9 evenly spaced (185 millimetres) heaters is positioned on the outside of the tube in order to provide heat for the molten zones. As shown on Figure 3-1, all heaters are bolted to a rack so that they move collectively at a rate of 55 millimetres per hour with a total travel distance for each furnace of 185 millimetres. A cross section of the assembly is provided in Figure 3-2.

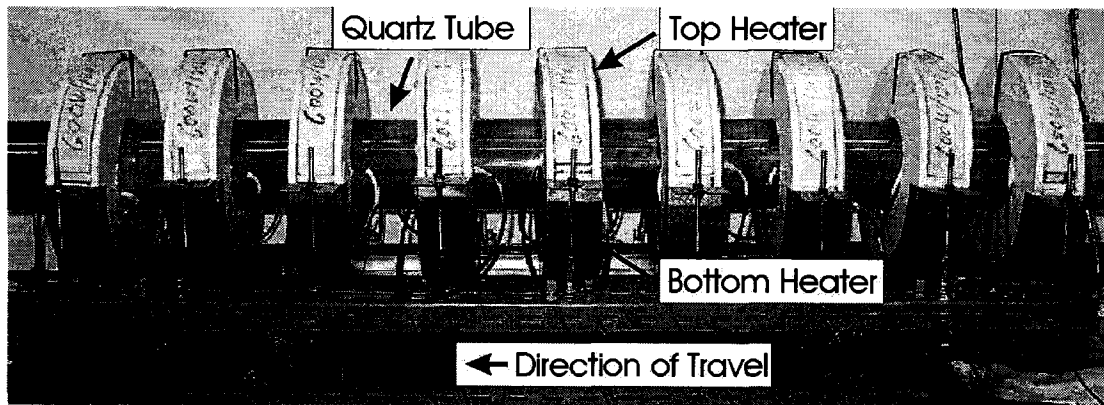


Figure 3-1: Zone refining heater assembly

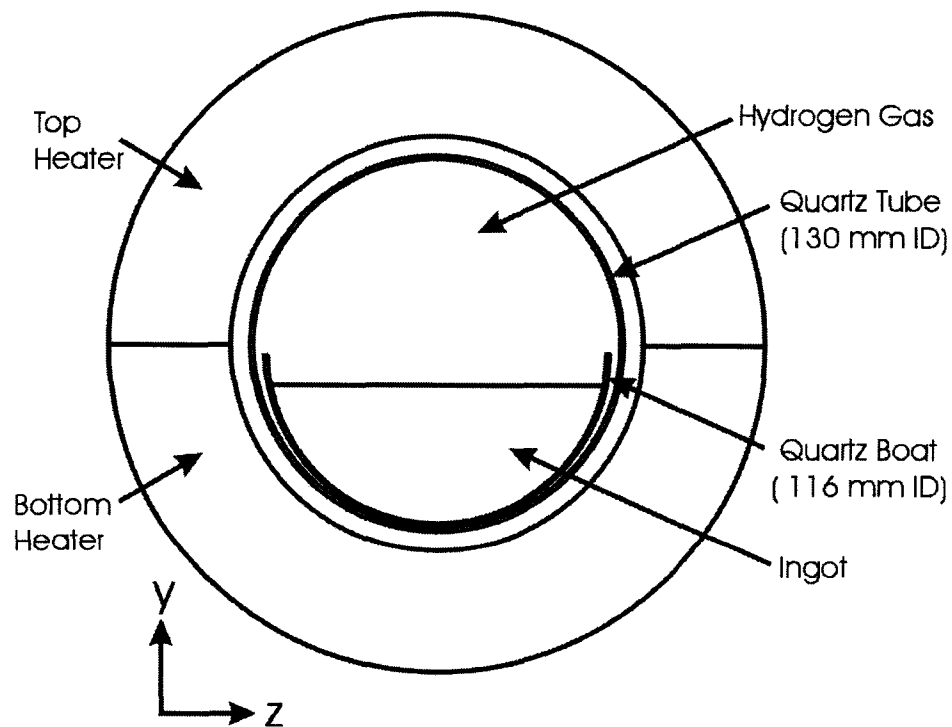


Figure 3-2: Cross section of tube, boat, and heaters

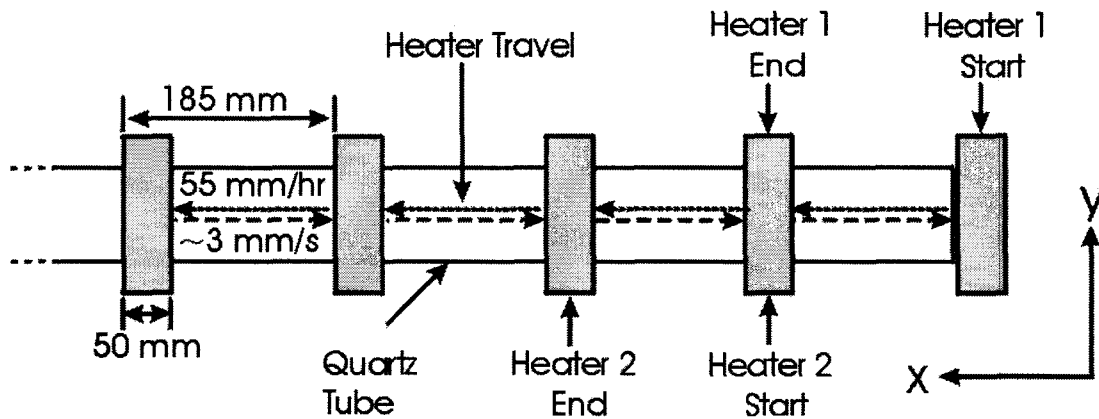


Figure 3-3: Schematic of heater movement

As shown in Figure 3-3, upon reaching the end of its travel, the entire assembly retracts quickly and the subsequent heater takes over where the previous one left off. The heaters act cooperatively so that the zone travels the entire length of the ingot. Nine zones are maintained simultaneously to speed up the processing time, however at the end of the procedure the heaters must be shut down in sequence to prevent any zone from freezing halfway through a pass. In addition, there is a discontinuity in the process while the heater retracts and the zone is left without heat for approximately one minute. A common industrial batch process consists of 35 passes with 8 shutdown passes and takes about a week of 24 hour per day operation to complete. Each heater consists of a top and bottom coil operated independently. The bottom heater (1200 W) is in closer contact with the melt and provides most of the heat while the top heater (600 W) keeps the surrounding region warm. The boat is commonly sprayed with boron nitride to reduce sticking and boat breakage during heating and cooling. As shown in Figure 3-1, white fiberglass insulation surrounds the heaters to decrease heat loss.

3.2 Experimental Design

In this section, practical choices for manipulated and controlled variables are discussed, and a test matrix is presented. The purpose of these experiments is to investigate how convection currents within the molten zone influence separation efficiency under a range of thermal and geometrical boundary conditions. Other than the absence of thermocouples and the use of new, uncontaminated lead, the zone refining equipment remained the same for thermocouple and assay tests. The assay tests were done separately from the thermocouple test to prevent contamination from the stainless steel thermocouple sheaths since they were in direct contact with the melt.

3.2.1 Manipulated Variables

The idea behind choosing manipulated variables is to identify factors that will affect the rate and complexity of fluid movement in the molten zone. According to Section 2.3.1, the geometry of the enclosure and thermal boundary conditions are most important for influencing convection. Although there are many ways to vary these conditions, practical solutions include changing the load depth and applying different combinations of insulation and cooling fans.

Changing the load depth is a convenient solution because it does not require the purchase of new boats other than what is presently used at Firebird Technologies. Semicircular boats are used in all cases because of their ease of fabrication, strength, and compatibility with cylindrical tubes. In addition, varying the depth changes the aspect ratio of the enclosure while changing boat size only varies its scale. Aspect

ratio of the enclosure is a very important variable for manipulating convection patterns [68] as discussed further in Section 5.2.1. Also, this approach is very easy to manipulate and can be accomplished by simply altering the amount of lead in the boat.

Another variable to manipulate is the temperature gradients in the ingot. To increase the buoyant forces in the molten zone, temperature gradients should be increased in the vertical direction. Thermal conditions can be manipulated by a variety of methods including adjustment of heater power, cooling fans, and insulation as described in Section 3.2.3. For example, applying heat to the bottom and cooling from the top of the ingot would encourage a temperature inversion in the form of fluid movement. This could be accomplished by introducing a cooling fan to the top of the zone and by increasing the bottom heater power input. Conversely, by applying insulation to the top of the zone and decreasing the bottom power input, the vertical temperature gradient would be decreased.

3.2.2 Control Variables

As mentioned in Section 3.2, the goal of assay experiments is to measure the impurity profile while the goal of thermocouple experiments is to measure the temperature field. Because of the difference in dependent variables, the control variables are specific for the two experiments. For example, variables such as ingot length and number of passes do not change convection within the zone but are essential for determining the impurity profile. As a result, ingot length and number of passes are important controlled variables in the assay experiments but are irrelevant for the

thermocouple experiments. On the other hand, according to Section 2.1, both the impurity distribution and convection rates are influenced by zone length and travel speed and therefore must be maintained constant throughout all experiments. Table 3-1 lists controlled variables for both experiments and their associated values.

Table 3-1: Controlled variables for thermocouple and assay experiments

Variable	Value	Thermal Tests	Assay Tests
Zone length (ℓ)	70 mm	<input checked="" type="checkbox"/>	<input checked="" type="checkbox"/>
Travel Speed (V)	55 mm/hr	<input checked="" type="checkbox"/>	<input checked="" type="checkbox"/>
Ingot Length (X)	1.56 m	<input type="checkbox"/>	<input checked="" type="checkbox"/>
Number of Passes (n)	9 full passes, 8 partial passes for shutdown	<input type="checkbox"/>	<input checked="" type="checkbox"/>

Initial concentration is a very important variable when considering the final impurity distribution after zone refining. In order to ensure consistent results between assay tests, the same feedstock was used. New lead metal was used for the assay tests in order to prevent contamination from the thermocouples. In addition, by using the same feedstock for all tests, it avoids the expense of multiple chemical analyses for control purposes.

In extreme circumstances, changes in composition can influence the material properties of liquid metal and therefore manipulate the fluid dynamics of the system. Fortunately the concentration range common in these experiments does not significantly affect the melting temperature or density. For example, in the control assay described in Section 3.4, all impurities added together equal to about 5.76×10^{-4}

atomic % of the lead. Out of all available phase diagrams, the impurity which depresses the melting temperature most is cadmium at 13.5°C per atomic % [69]. If all impurities depressed the melting point at this rate, the melting point would be reduced by only 0.0078°C, which is far below the thermocouple resolution. Similarly, it is not likely that such low concentrations will affect the density of lead significantly, and therefore concentration gradients will not result in a significant change in buoyancy [42].

3.2.3 Test Matrix

A test matrix based upon the manipulated variables described in Section 3.2.1 is summarized in Table 3-2. Variables are arranged so that the expected rate of fluid movement will decrease from Test 1 through to Test 5. Accordingly, it is expected that the Grashof number will decrease from Test 1 to Test 5.

Table 3-2: Test matrix for thermal measurement experiments

Test Number	Description
Test 1	Deep depth (42mm), no top insulation, cooling fan
Test 2	Deep depth (42mm), no top insulation
Test 3	Mid depth (22mm), no top insulation
Test 4	Shallow depth (18mm), no top insulation
Test 5	Shallow depth (18mm), with top insulation

The goal in Test 1 was to maximize the driving force for convection by having the deepest depth and strongest external temperature gradients. As described in Section 3.2.1 and depicted in Figure 3-4, the top insulation was removed and a cooling fan was applied to the exterior of the tube.

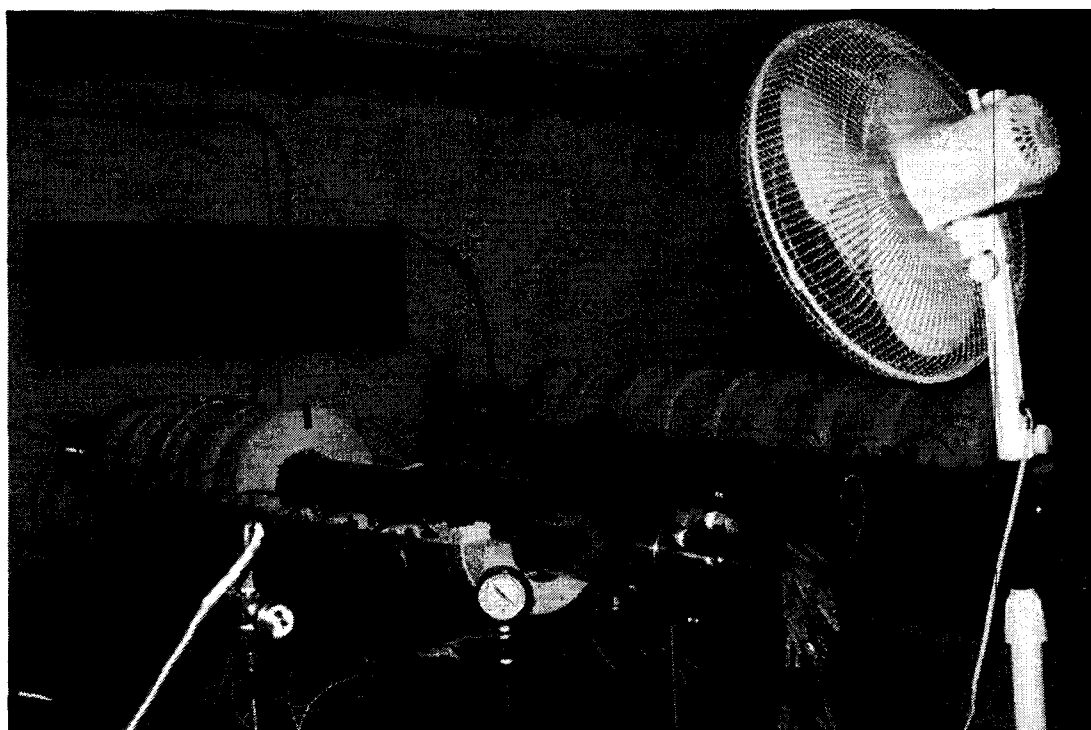


Figure 3-4: Cooling fan applied to the exterior of the tube for Test 1

For Test 1 and 2, the depth of the melt was maximized. Due to the high density of lead, the length of the ingot was limited in order to meet the weight capacity of the apparatus. The ingot extended just beyond the sixth heater, was dammed using solid lead, and the remaining portion of the boat was left empty. As discussed in Section 3.3, thermal data is not collected from zones 5 through 9 therefore their insulation was not removed. A zone was established above heater 5 in order to maintain consistent boundary conditions for heater 4 while no power was given to heaters 6 through 9 throughout all thermocouple tests.

Test 2 had similar boundary conditions compared to Test 1 except the cooling fan was removed. For Test 3, the depth was reduced by melting the entire bar, thus allowing molten lead to run to the end of the boat and extending the ingot length. The depth

was once again decreased for Tests 4 and 5 by removing the ingot from the apparatus, cutting off the last third of ingot length, and then melting the entire ingot to fill the bottom of the boat.

The goal of Test 5 was to minimize the driving force of convection by having a low depth and low external temperature gradients. Insulation was added to the front of the heaters similar to existing equipment at Firebird Technologies. The top heater (see Figure 3-5) was not operated in any test but served as insulation in Test 5.

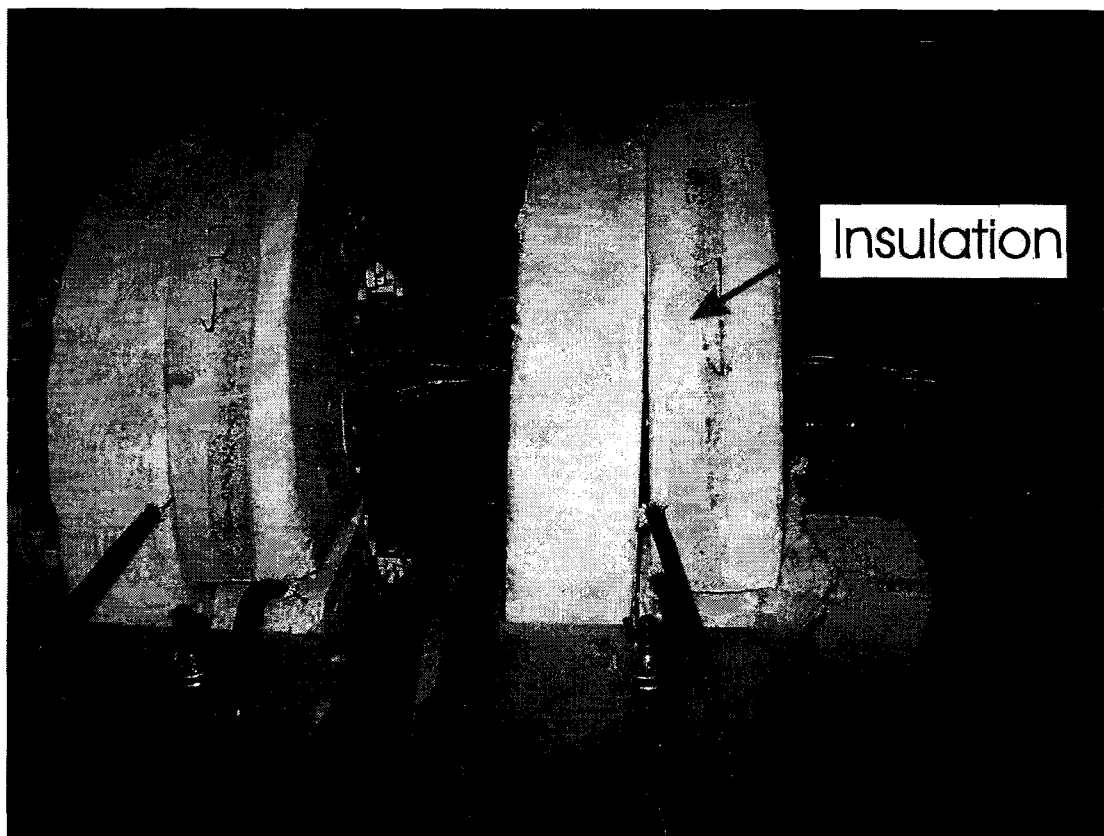


Figure 3-5: Insulation added on top of the tube and in front of the heater for Test 5

3.3 Thermocouple Tests

This section discusses test procedures and equipment specific to the thermocouple tests. During operation, the quartz tube is evacuated then back-filled with hydrogen.

A pass-through purchased from Omega with Teflon ferrules was incorporated into the design to provide a seal around the thermocouples entering the end cap of the tube. The smallest pass-through diameter (1 millimetre) was sourced in order to incorporate the smallest thermocouple diameter possible. Small thermocouples are required in order to minimize the heat transfer from the melt and to limit interference between the probes and fluid movement within the zone. This dictated a 1 millimetre thermocouple/pass-through combination as shown in Figure 3-6. Thermocouples were purchased at WIKA with specifications found in Appendix A.

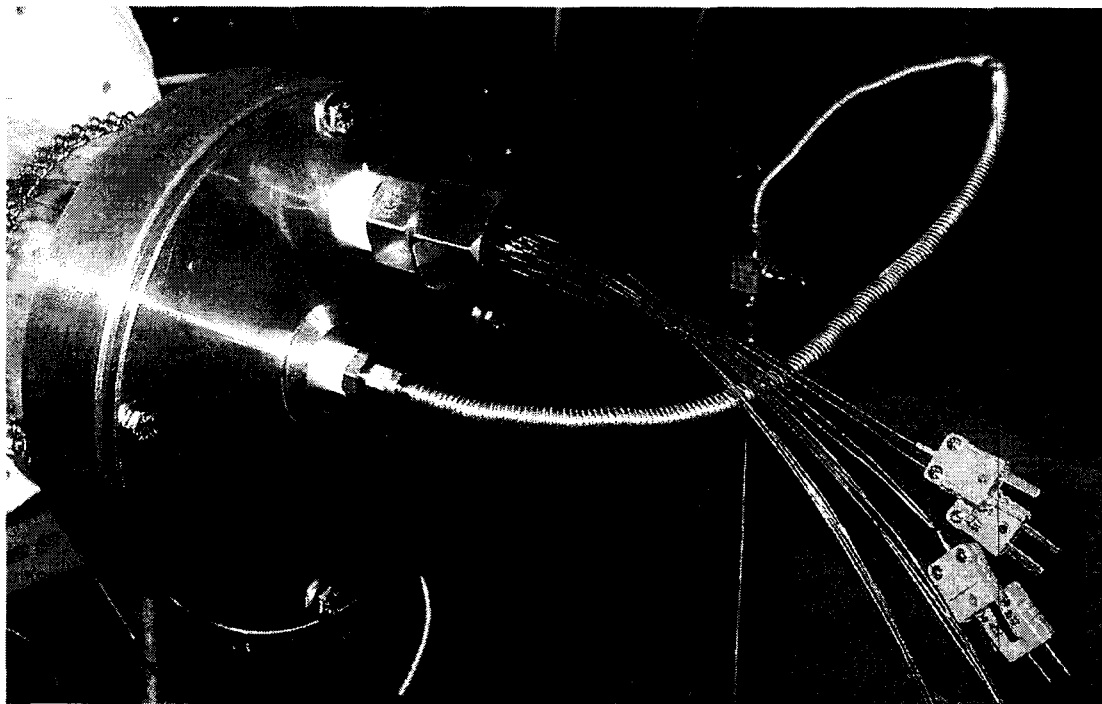


Figure 3-6: Thermocouple pass-through

Before and after the tests, the thermocouples were calibrated to refine their accuracy (thermocouple error was $\pm 1.3^{\circ}\text{C}$ at 327.5°C prior to calibration). Each thermocouple was inserted into a Hart Scientific dry-well calibrator set to $327.5^{\circ}\text{C} \pm 0.15^{\circ}\text{C}$ (lead melting temperature), allowed to equalize, and then the signal was measured using a Fluke 725 multifunction process calibrator (accurate to within $\pm 0.1^{\circ}\text{C}$). The settings

in the 32 channel National Instruments data logger were adjusted for each thermocouple according to this calibration. Total error is expected to be around $\pm 0.46^{\circ}\text{C}$ by combining error of the drywell calibrator ($\pm 0.15^{\circ}\text{C}$), the data logger ($\pm 0.21^{\circ}\text{C}$), and the multifunction calibrator ($\pm 0.1^{\circ}\text{C}$). Data logger resolution error was very small at $\pm 0.009^{\circ}\text{C}$ and the thermocouples were accurate to within $\pm 0.1^{\circ}\text{C}$ of one another after calibration. Thermocouple corrections as well as specifications for the drywell block calibrator, calibrator, and data logger are presented in Appendix A.

To ensure direct contact with the melt, holes were drilled into the solid bar prior to the experiments and the thermocouples were inserted. The probes were organized in six planes (A-F) with four thermocouples each, for a total of twenty four. One additional thermocouple was delegated to measure the ambient temperature of the room. As shown in Figure 3-7, there are two planes (A and B) designed to measure horizontal temperature gradients at the surface of the zone and four planes (C through F) designated for vertical temperature gradients. Each plane of thermocouples was positioned 50 millimetres from its pair (A/B, C/D, E/F). Each pair of planes were positioned in the center between the heaters in their starting position.

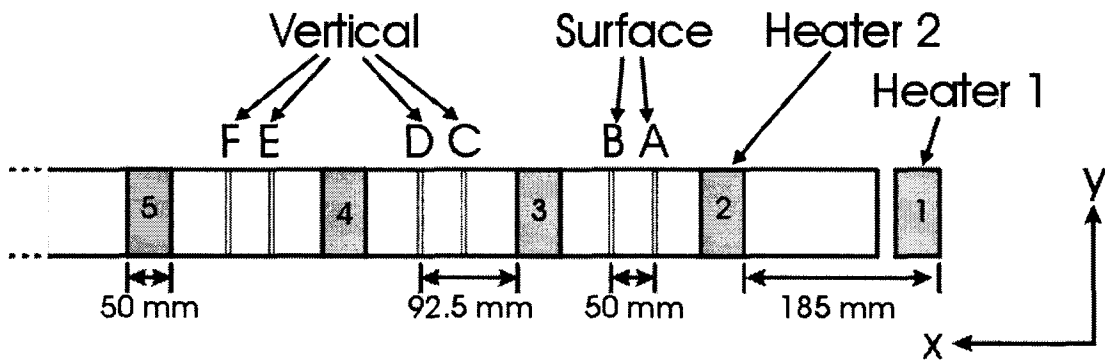


Figure 3-7: Thermocouple Configuration within the zone refining apparatus

The thermocouples were arranged in two different configurations to measure both surface and vertical temperatures shown in Figure 3-8 and Figure 3-9 respectively. The horizontal and vertical position of thermocouples were measured before and after completion of the tests and are shown in Table 3-3 and Table 3-4. Unfortunately the vertical position of plane A and B were not stable throughout the experiments and their data could not be used for analysis in Chapter 4. Planes C through F were held in constant position throughout the experiments, set approximately 9 millimetres apart to span the depth of the deepest test with the lowest thermocouple approximately 2 millimetres from the bottom of the zone.

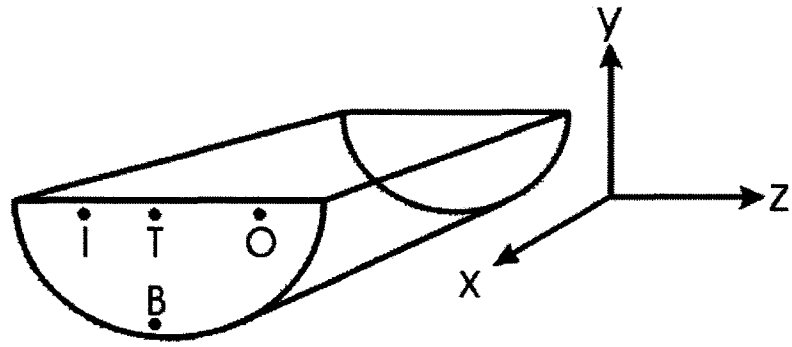


Figure 3-8: Placement of surface (horizontal) thermocouple in planes A and B

Table 3-3: Position of thermocouples in surface planes

Thermocouple	Plane 'A'	Plane 'B'
Top (T)	centre	centre
Bottom (B)	centre	centre
Outer (O)	32 mm right of centre	32 mm right of centre
Inner (I)	16 mm left of centre	16 mm left of centre

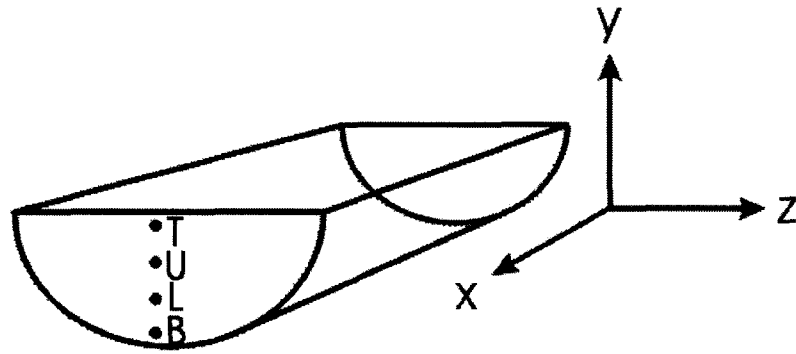


Figure 3-9: Placement of vertical thermocouples in planes C through F

Table 3-4: Position of thermocouples in vertical planes

Thermocouple	Plane 'C'	Plane 'D'	Plane 'E'	Plane 'F'
Top (T)	29.5 mm	33.5 mm	33 mm	30 mm
Upper-mid (U)	21.5 mm	22.5 mm	23 mm	21 mm
Lower-mid (L)	10 mm	17.5 mm	13 mm	11 mm
Bottom (B)	2 mm	4.5 mm	3 mm	1 mm

3.3.1 Thermocouple Testing Procedure

For each set of test conditions, the heater voltages were adjusted manually until a molten zone of about 70 millimetres was established, measured using a ruler on the exterior of the tube. The heaters were then set in motion at 55 millimetres per hour and a number of different passes were done for each test condition in order to establish a consistent zone size. The zone size did vary somewhat (approximately 5 millimetres) during the experiments because of the changing boundary conditions associated with the varying position of the heaters on the bar. Once heater settings were established, the data logger was then engaged and the stationary thermocouples

profiled the temperature within the zone for several passes. A summary of the thermocouple tests are shown in Table 3-5.

Table 3-5: Summary of passes done during thermocouple tests

	Test 1	Test 2	Test 3	Test 4	Test 5
Number of Passes Done	4	3	4	2	3

The collection rate was chosen to be 10 hertz. Since 10 hertz is a multiple of 60 hertz, interference from the alternating current power supply was minimized. In addition, the collection rate is sufficient for detecting the anticipated oscillation frequencies due to convection (see Section 4.3.1). Data was gathered and recorded using LabVIEW 7.0 for later analysis using Matlab 7.1 and Excel.

3.4 Assay Tests

The intent of the assay tests was to duplicate test conditions presented in Table 3-2 in the absence of thermocouples. The difference, as outlined in Section 3.2.2, is that a constant ingot length and number of passes is required (see Table 3-1). In order to ensure a consistent ingot length, the entire length of the boat was used, requiring the use of all 9 heaters simultaneously. In addition, longer ingot length presents a greater degree of resolution for comparing the separation efficiency of different operating conditions. This is related to the fact that, after zone refining, a longer ingot length would exhibit a more dramatic change in concentration profile (see Section 2.1), and therefore assay results are accentuated between tests of various segregation rates. The problem with using the entire boat length is that, with the depths of Test 1 and 2, the weight capacity of the glassware would be exceeded. Unfortunately this limits the assay experiments to the test conditions of Tests 3 through 5. However, there is a

good representation of different thermal and geometrical boundary conditions between Tests 3, 4, and 5.

Prior to assay experiments, new lead was acquired from the same feedstock as the thermocouple experiments, etched using HCl (38% mol), and assayed to measure initial concentrations. The boat was etched using CP4 (12% HF, 24.5% CH₃COOH, 35% HNO₃) to eliminate contaminants. After the bar was zone refined according to Table 3-2, it was solidified, cooled, removed from the zone refining apparatus, and then sampled. A small pool of molten lead was created on the top surface of the bar using a propane torch, then drawn up into a 1 millimetre glass tube using a pipette bulb. Three samples were taken from each ingot at 10%, 50% and 80% of the ingot length and sent for Glow Dispersion Mass Spectrometry (GDMS) at the National Research Council in Ottawa. To ensure homogeneous concentrations for the next test, the bar was completely melted and left for fifteen minutes to mix thoroughly. Depth was adjusted for Test 3 and 4 as described in Section 3.2.3 for the thermocouple tests.

3.5 Summary of Experimental Procedures

This chapter outlined the procedure and experimental equipment used for thermocouple and assay tests. The purpose of these tests was to measure a range of convection conditions within the molten zone, and correlate convection characteristics to separation efficiency. Thermocouple tests are used to profile the thermal field used to characterize the convection. Assay tests are used to measure the impurity concentration along the length of the bar to calculate separation efficiency.

This data will be presented and processed in Chapter 4 and the correlation between convection characteristics and separation efficiency will be discussed in Chapter 5.

Chapter 4 Discussion of Experimental Results

This chapter contains a discussion of experimental results for the thermocouple and assay experiments described in Chapter 3. Using these experiments, the fluid movement within the molten zone is characterized for different operating conditions and correlated to separation efficiency. Prior to analysis of the thermal measurements, the data was filtered to separate general temperature trends from the fine fluctuations. General temperature trends were then analyzed to give information about the shape of the molten zone, temperature gradients, and the resulting buoyant driving forces for convection. Fine fluctuations in the temperature signal were analyzed for information about the convection regime and the rate of fluid movement within the enclosure. Using these two techniques, a relationship between operating conditions, temperature trends and the corresponding fluid movement intensity was formulated. For the assay test experiments, separation efficiency was evaluated using a computer program to model the measured concentration profile after zone refining. In combination with knowledge of the convection characteristics from the temperature analysis, a relationship between the operating conditions and separation efficiency is formed.

4.1 Typical Thermocouple Data

This section introduces some characteristics common to all thermocouple experiments. Figure 4-1 shows an example of typical thermal measurements from a single molten zone. The data was gathered during Test 2 by thermocouples arranged vertically in plane 'C' (see Figure 3-7). More examples of data from Tests 1, 3, 4 and 5 are given in Appendix B.

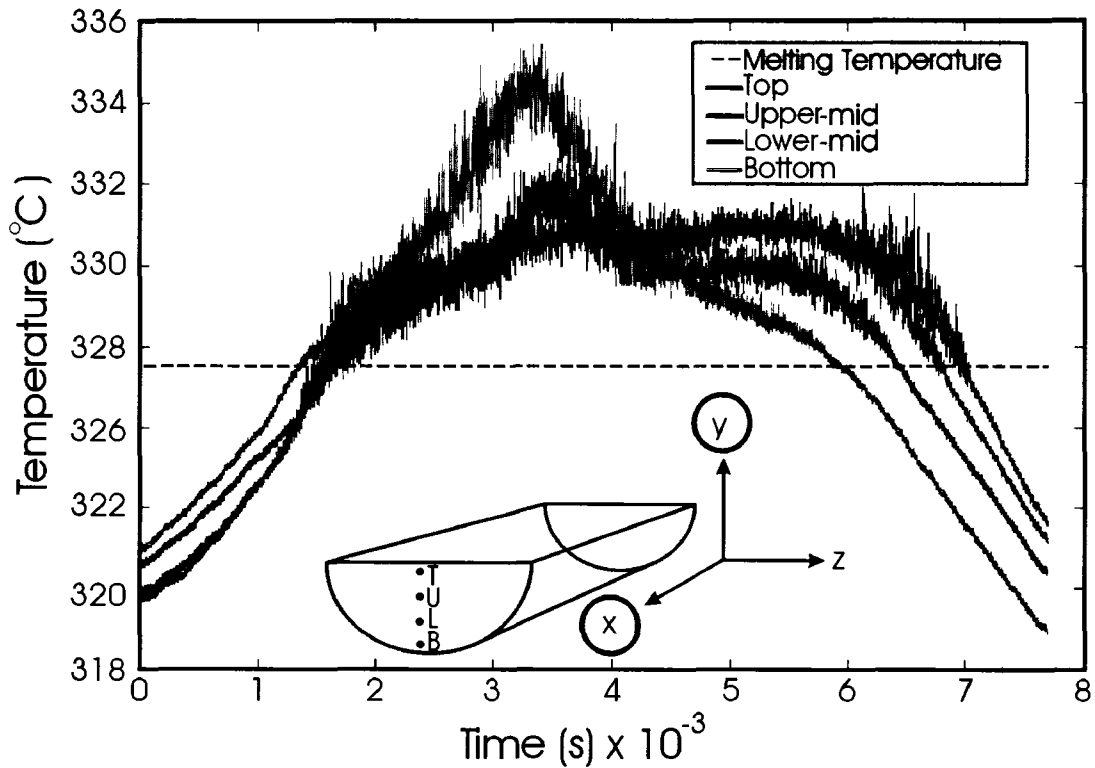


**Figure 4-1: Typical Temperature Data of the Molten Zone
Test 2, plane 'C', pass 2**

From left to right, as the heater approaches the plane of thermocouples, the temperature rises towards the melting temperature. When the thermocouples reach melting temperature (dotted line), they cross the melting interface and are submerged in the molten metal of the liquid zone. The thermocouples trace the lengthwise profile of the molten zone and then mark the freezing interface as the temperature decreases below the melting temperature again. Note that the positions of the melting and freezing interfaces vary between thermocouples and can be used to identify the shape of the molten zone. As shown in Figure 4-1 and Appendix B, the shape of the interface is typically not vertical because the thermocouples do not pass through the melting temperature at the same time. Commonly there is larger gap between thermocouples passing through the freezing interface compared to the melting interface. This indicates that the freezing interface is more sloped than the melting

interface. Pure metal systems such as the lead used in this experiment do not experience a significant depression of freezing point because solute concentrations are small [70]. As a result, melting point will not deviate between tests and is a reliable indication of interface location. A further discussion of interface shape is given in Section 4.2.

From left to right, the temperature changes with time. Also, at any position within the zone, a temperature difference is apparent between thermocouples. This indicates that there are both vertical and horizontal temperature gradients within the zone. Typical of all experiments, the highest temperature is at the bottom of the zone just left of centre, as indicated by the light blue line in Figure 4-1 and in additional data sets presented in Appendix B. The location of this peak is due to the position of the zone relative to the heater as explained further in Section 4.2.1. The lower-mid thermocouple shows a less pronounced peak at this location. For the bottom and lower-mid thermocouples, the highest temperature gradients surround the temperature peak. For the top and upper-mid thermocouples, the highest temperature gradients are typically surrounding the edges of the zone but are relatively flat throughout the bulk of the melt. The temperature patterns do not appreciably change between tests. A further discussion of these general temperature trends is given in Section 4.2.

A typical phenomenon for all thermocouple experiments is that, at temperature above the melting point, the temperature signal fluctuates. Note that when the lead is below melting temperature (327.5°C [44]), heat transfer is limited to conduction in the solid

resulting in a smooth temperature signal. When the thermocouples are submerged in molten lead, the signal varies in response to the convection currents in the liquid [46]. As shown in Appendix B, some tests show fluctuations in the signal below the melting temperature to the left of the melting interface. These fluctuations are likely due to interference caused by the close proximity of the heater. This interference would be at 60 Hz due to the frequency of the alternating current in the heaters. Unfortunately, the frequency of the alternating current is much faster than the data capture rate from the thermocouples and therefore the interference cannot be resolved using signal analysis tools. In the general temperature analysis in Section 4.2, this interference should be filtered out when processed using a low pass filter. As demonstrated in Figure 4-1, the amplitude of fluctuations in the temperature signal are not uniform, but vary according to position within the zone. A further discussion of temperature fluctuations is given in Section 4.3.

Valuable data can be inferred from both the general temperature trends and the small fluctuations of the raw signal. However, it is difficult to analyze the temperature signal in its raw form. For example, since the amplitude of the fluctuations is typically up to 4°C, it is difficult to identify the general temperature at any given point. Also, it is difficult to characterize the frequency and amplitude of the fluctuations in the presence of the general temperature trends. In order to address this problem, a low pass filter was applied to eliminate any higher frequency temperature fluctuations for analysis of the general temperature trends, while a high pass filter was

applied to isolate the small temperature fluctuations of higher frequency. This filtering technique is described in Appendix C.

As the heater moves along the length of the ingot, the stationary thermocouples trace the length of the moving zone. Since the heater travel rate was held constant at 55 millimetres per hour, it took about 1 hour and 15 minutes (4500 s) for the thermocouples to trace a zone of about 70 millimetres in length, as reflected on the x axis of Figure 4-1. Data was collected at a rate of 10 hertz throughout the experiments which produced about 60 000 data points per thermocouple for one zone. In tests where ingot depth was reduced, some thermocouples were not submerged and did not provide data. For example, as shown in Table 3-3 and Table 3-4, thermocouples higher than 22 millimetres were not submerged during Test 3 and thermocouples above 18 millimetres were not submerged in Tests 4 and 5. The result is a 2-D profile of the zone with fine resolution along the length of the ingot, and four data points for Tests 1 and 2, three data points for Test 3, and two data points for Tests 4 and 5 in the vertical direction. This is reflected in the sample data displayed in Appendix B.

Data from planes 'E' and 'F' were discounted because of a faulty thermocouple after Test 3. Their position was altered during the process of replacing this thermocouple and therefore data is not consistent for all tests. As discussed in Section 3.3, data from planes 'A' and 'B' was not used because of their unreliable position. In addition, the position of probes in plane 'D' were higher than planned and therefore only two thermocouples were submerged in Test 3. Plane 'C' had the best vertical position to

span all depths and was used for most analysis dealing with buoyant convection in this project.

4.2 Analysis of General Temperature Trends

General temperature trends can be used to give information about the shape of the zone, possible fluid flow patterns, and the driving force for convection. As calculated using a low pass filter in Appendix C, the temperature fluctuations are removed to create general temperature trends. Qualitative information of these average temperatures and temperature gradients is given in Section 4.2.1 using contour plots. Quantitative information about the driving force for natural convection is given in Section 4.2.2 by calculating the Grashof number.

4.2.1 Temperature Visualization

Contour plots were produced using the 'CONTOURF' function in Matlab 7.1 in order to visualize the general temperature gradients and shape of the interfaces. The contour plots shown in Figure 4-3 are created using data gathered from plane 'C' for all test conditions. The molten zone is represented by a 2-D lengthwise temperature profile as shown in Figure 4-2.

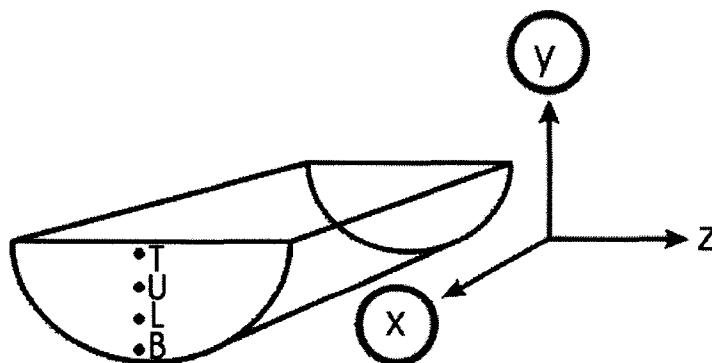


Figure 4-2: Orientation of 2-D contour plots

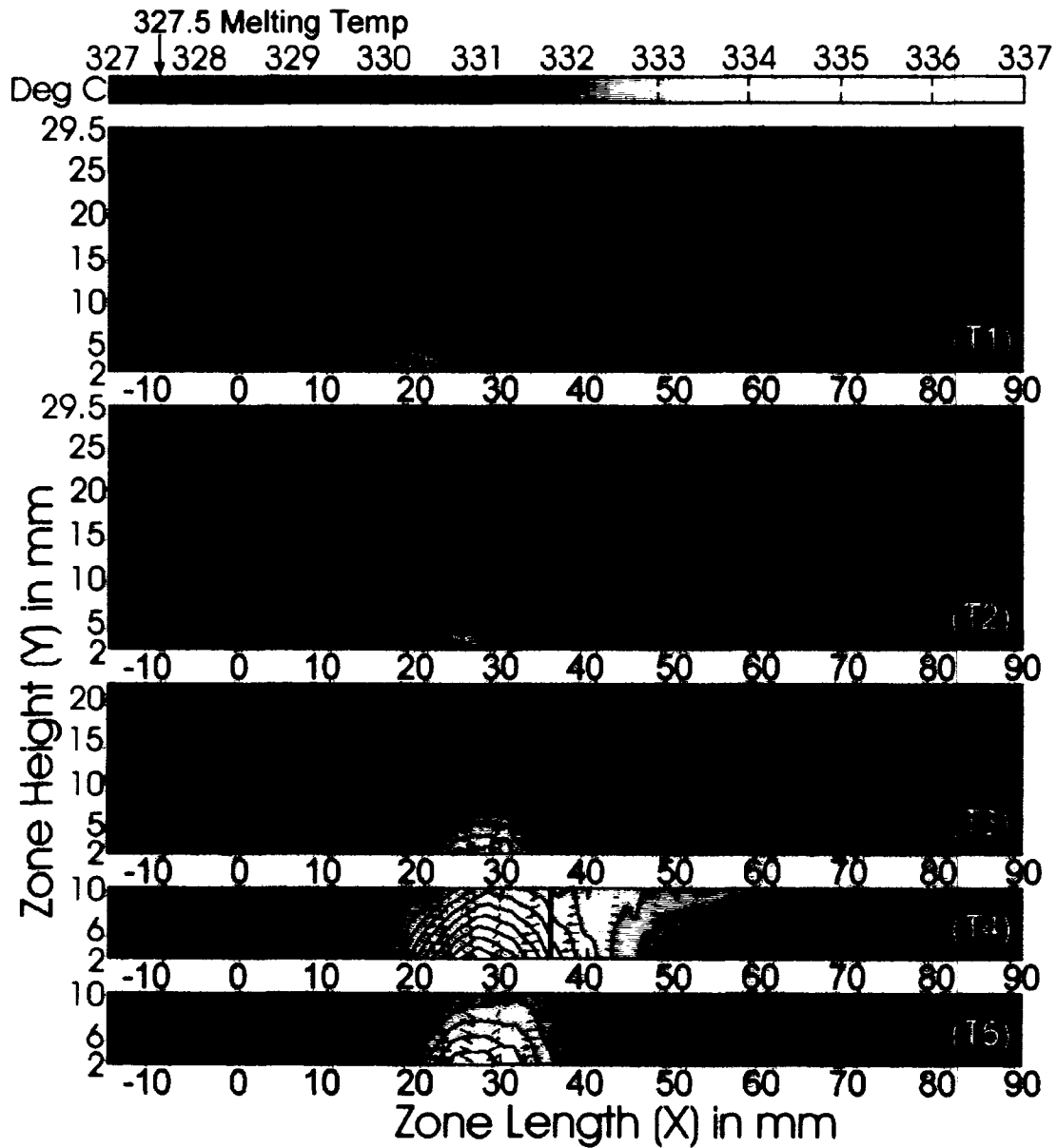


Figure 4-3: Lengthwise temperature contour plot of the molten zone for (T1) Test 1, pass 3 (T2) Test 2, pass 2 (T3) Test 3, pass 3 (T4) Test 4, pass 2 (T5) Test 5, pass 1

The x-axis of the contour plots represents zone length while the y-axis represents the depth. Contour lines are spaced to represent a change in temperature of 0.5° C. As discussed later, the green vertical lines represent the position of the heater, and the blue quiver arrows indicate the direction and magnitude of temperature gradients. Although data is gathered over time, the position within the zone is calculated using

the travel rate of the heaters. Since the axes are given in units of length, the plots approximate a still picture of the molten zone. However, from the moment when the thermocouples pass through the melting interface (left) to when they cross the freezing interface (right), the zone has traveled approximately 70 millimetres and 1 hour 15 minutes has elapsed. During this time, it is possible that the zone size and temperature may have changed slightly. No significant trend has been noticed and this phenomenon has been ignored.

As discussed in Section 4.1, data is gathered at 10 hertz throughout the experiment and therefore provides high resolution of data along the length of the zone. On the other hand, vertical data points are limited to the number of thermocouples submerged in the melt in each plane (see Table 3-4 for thermocouple locations). For example, Figure 4-3 (a) and (b) have four, (c) has three, while (d) and (e) have two vertical data points. The 'CONTOURF' function interpolates to produce uninterrupted contour lines between data points. Therefore, the shape of contours and interfaces are calculated and may deviate from the actual shape of the interface. This explains the presence of aberrations along the contour lines, and sharp discontinuities along the interface shapes in Figure 4-3.

The color scale on the top of the figure is calibrated for degrees Celsius. This was chosen so that all temperatures below the melting temperature are black and the first contour line represents the melting and freezing interfaces. In most cases, the

interface is not vertical, and quite commonly, the freezing interface is more sloped than the melting interface.

There are a range of factors that contribute to the shape of the interface including zone size, the distance between two adjacent zones, and the distance between the interface and the heater (see Section 5.2.3). Zone size and position is dependent the ambient room temperature, humidity, insulation, heater power, adjacent zone refining equipment, or any other factor that influences external temperature gradients. This is a complex relationship and has been modeled in literature [71], but is not quantified in this project.

Temperatures within the molten zone are also important for the interface shape. At the edges of the zone, higher temperatures are typically found near the top. This causes the interfaces to slope outwards at the top as shown in Figure 4-3. This phenomena is also confirmed in Figure 4-1 where the bottom thermocouple is first to freeze and the top thermocouple is last to freeze. An exception can be found in Figure 4-3 (a) where the cooling fan of Test 1 causes rapid heat loss at the top of the ingot and the melting interface slopes in towards the top. However, as shown in Figure 4-3, the zone length is greater at the top compared to the bottom in all tests. A discussion of how the interface shape affects convection currents is described in Section 5.2.3.

The contour plots show a two dimensional view of the molten zone. However, visual observations during the experiments indicate that the interface shape can vary in the

horizontal direction as well. A common interface shape in the absence of thermocouples is bowed inwards towards the edges of the zone, as shown in Figure 4-4.

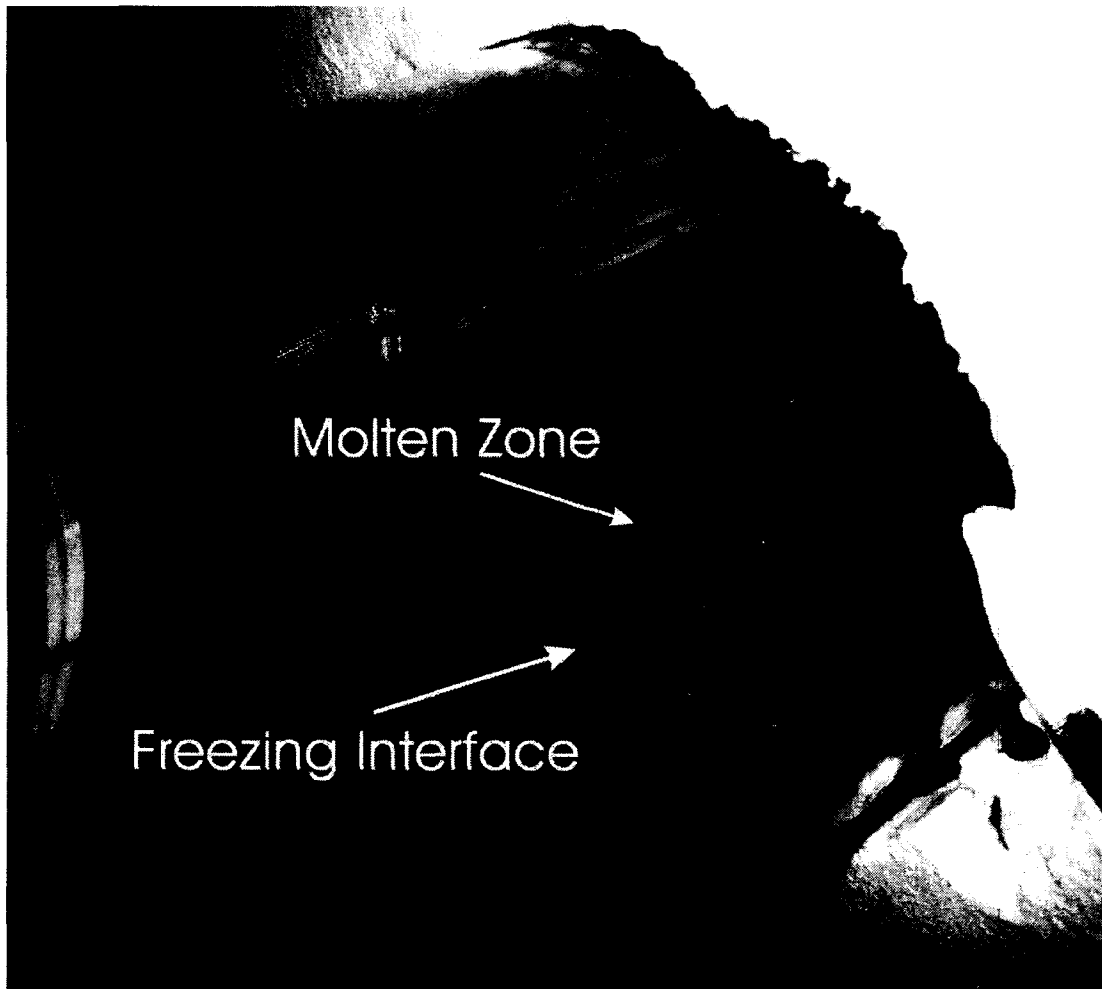


**Figure 4-4: Typical horizontal interface shape
(typical zone refinement of indium antimonide)**

During the thermocouple experiments, the probes are in direct contact with the melt and consequently provide an undesirable heat sink effect. This can influence the shape of the interface in different ways. For example, a slight 'hour-glass' shape can occur when the interfaces passes by the thermocouples.

In Figure 4-3, the location of the heater is depicted as the region between the green vertical lines. In all tests, the zone typically trails the heater. This lag is most likely due to the motion of the heater and direction of heat flux. For example, the material must be within range of the heater to absorb heat. By the time the material reaches its melting point, time has elapsed and the melting interface trails behind the leading edge of the heater. This is accentuated in Test 1, most likely due to the increased heat transfer rate from the cooling fan and steeper temperature gradients. In addition, the material must be out of the heater's proximity in order to cool, creating distance between the freezing interface and the heater.

Quiver arrows are included on the contour plots in Figure 4-3 to show a qualitative description of temperature gradients within the zone. Temperature gradients can be visualized by noting the distance between the contour lines and length of the blue quiver arrows. The closer the distance between contour lines and the longer the quiver arrows, the stronger the temperature gradients. As shown in Figure 4-3, the highest temperature gradients are typically near the hot spot at the bottom of the zone, and adjacent to the interfaces. These regions likely have the highest driving force for convection and the most active fluid movement. Further evidence of this is given in Section 4.3.2 by describing the location of the most active regions of fluid movement.

A qualitative comparison between contour plots in Figure 4-3 reveals that internal temperature gradients increase as the depth of the charge is reduced. It is assumed that external temperature gradients change gradually between Tests 2, 3, and 4, and

therefore require similar rates of heat transfer and Grashof numbers. A possible explanation is that, in order to get comparable Grashof numbers with decreasing geometry (L), internal temperature gradient must be higher (ΔT). In the case of Test 1, the cooling fan creates higher external temperature gradients and therefore the heat transfer rate is increased. The result is an increase in internal temperature gradients in Test 1 compared to Test 2. The opposite phenomenon occurs when applying insulation in Test 5, which creates smaller temperature gradients when compared to Test 4.

Prior to experiments, it was expected that the temperature peak in the fluid would correspond to the hottest region of the heater. The color of the heating elements was typically brightest near the centre of the heater as shown in Figure 4-5. On the contrary, the temperature peak is often near the trailing edge of the heater as shown in Figure 4-3.



**Figure 4-5: Heating element surrounding the zone
(typical zone refinement of indium antimonide)**

The location of the temperature peak is most likely influenced by convection cells within the zone. For example, it is expected that fluid flows along the bottom of the zone while being heated, approaches the hot spot, and then travels upwards. In plots where the hot spot is near the centre of the zone (see Figure 4-3 (b)), torodial flow is anticipated where two opposing convection cells meet at the bottom of the zone. To complete the cycle, fluid would move down the interfaces while being cooled. In Figure 4-3 (c), a smaller convection cell adjacent to the melting interface is expected because the temperature field is lop-sided towards the melting interface. In some contour plots, (Figure 4-3 (a and c)) a chimney of warmer fluid extends above the hot

spot and curls towards the freezing interface. This is indicative of a large convection cell occurring between the peak temperature and the freezing interface. A single large convection cell is expected in Figure 4-3 (a) because the peak temperature is in close proximity to the melting interface. Depending on the operating conditions, fluid flow patterns appear to change between single convection cells and torodial flow. Despite all speculation, temperature gradients are not conclusive evidence of the flow field [68].

Further support of a torodial flow and single convection cells are described in Section 4.3.2 by analyzing the relative strength of temperature fluctuations in different locations of the melt. Although the flow pattern seems to change between experiments, the most important observation is that discernable flow patterns exist. This suggests that turbulent flow is not likely to occur in this system and laminar or periodic convection prevails.

4.2.2 Measured Grashof Numbers

The idea behind the thermocouple experiments was to control convection via thermal boundary conditions and geometry of the enclosure. It was hypothesized that the level of convection will reduce as conditions are manipulated from those of Test 1 to Test 5. In order to quantify the driving force for convection, temperatures were measured and the Grashof number was calculated according to the variables found on Table 2-2. As described in Section 2.3.1, the Grashof number is a ratio of the buoyant and viscous forces according to Equation (4-1) and is a measure of the driving forces of natural convection.

$$Gr = \frac{g\beta_T L^3 \Delta T}{\nu^2} \quad (4-1)$$

Several ways to define the characteristic length can be found in literature. A common experimental setup for natural convection in small enclosures is to impose horizontal temperature gradients [72]. In this case the author identified horizontal enclosure length as the characteristic length. Other literature sources used a combination of the 3 dimensional distances (e.g. *depth*⁴ / *length*) for the characteristic length in different geometries [73]. In this thesis, the heating conditions are quite complex due to circumferential heaters, sidewall cooling, and complicated geometry. Gravity and buoyant forces act in the vertical direction and since the vertical distance was the smallest distance, depth of the molten zone was a natural option for the characteristic distance (L). The temperature gradient (ΔT) was chosen to be the peak temperature minus the temperature of the interface (melting temperature).

A summary of the Grashof calculations is shown in Table 4-1 and Figure 4-6. Several passes were completed for each test condition as shown in Table 3-5, and the Grashof number was averaged for all passes. The obvious trend is that the Grashof number decreased in the manner hypothesized from Test 1 through 5. Note that there is a large reduction between Test 2 and 3 due to a large decrease in the zone depth. From this analysis, it is obvious that the driving force for convection currents reduces consistently from Tests 1 through 5.

Table 4-1: Temperature Gradients, Characteristic Length and Grashof Calculations

	Plane 'C'			Plane 'D'		
	ΔT $\pm 0.46^\circ\text{C}$	L (mm)	Gr	ΔT $\pm 0.46^\circ\text{C}$	L (mm)	Gr
Test 1	5.8	42	8.6×10^6	3.8	42	5.5×10^6
Test 2	5.8	42	8.6×10^6	2.6	42	3.8×10^6
Test 3	7.2	22	1.5×10^6	5.4	22	1.1×10^6
Test 4	9.4	18	1.1×10^6	6.8	22	7.9×10^5
Test 5	6.5	18	7.5×10^5	5.3	18	6.2×10^5

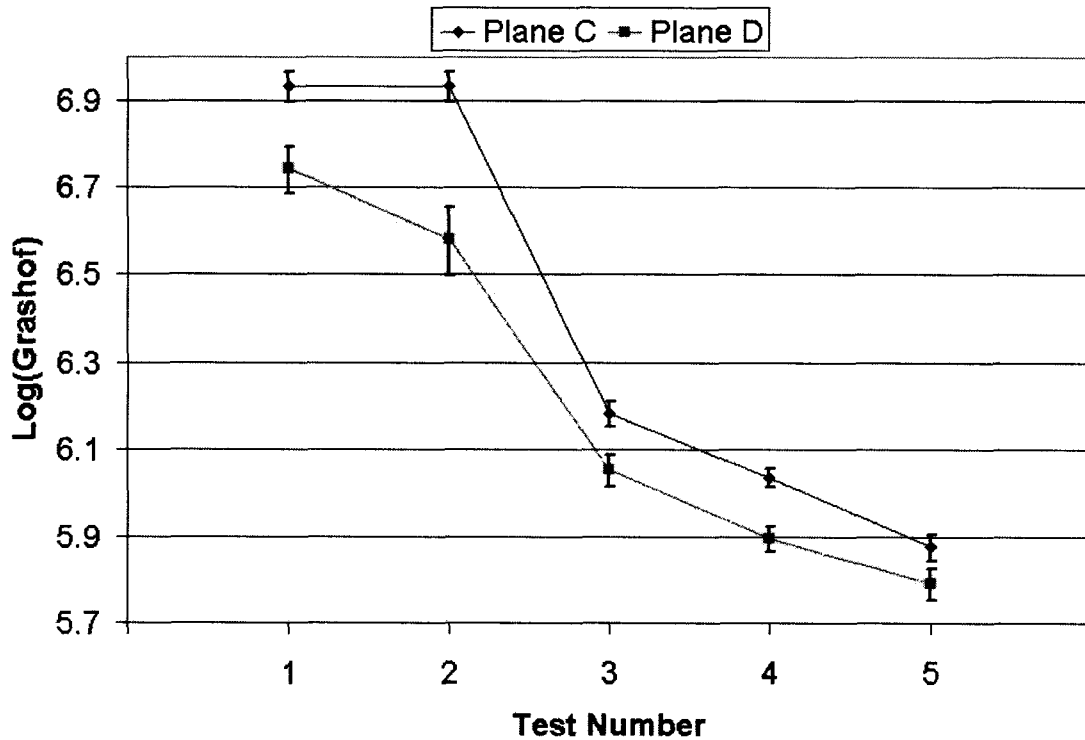


Figure 4-6: Average log of Grashof versus Test number for planes C and D

The Grashof number calculated for Test 2, plane 'C', is very close to the value for Test 1. This could be attributed to an irregularly high temperature value for one of the

passes of Test 2, even though all other passes were below the Test 1 average. All other planes exhibited a more drastic decline between the two tests.

4.2.3 Critical Grashof Number

The critical Grashof number is a common topic in fluid dynamics. Above this threshold value, flow transitions occur and time dependent flow is dominant. Henry et al. [74] used 2-D and 3-D numerical work to calculate bifurcations to estimate these flow transitions (see also [75]). The following table summarizes additional results found in literature.

Table 4-2: Critical Grashof Numbers from Literature

Gr _c	Technique/Notes	Reference
Gr=25350	2-D Numerical model, horizontal ΔT (4·2·1) enclosure dimensions, Pr=0.026	[74]
Gr=2.05x10 ⁵	3-D Numerical model, horizontal ΔT (4·1·1) enclosure dimensions, Pr=0.015	[76]
Gr=4x10 ⁴	experimental and numerical work, horizontal ΔT horizontal Bridgman apparatus various metals and aspect ratios	[42]
Gr=21600-2.4x10 ⁵	Experimental work, horizontal ΔT shallow enclosure- varying aspect ratio Mercury (Pr =0.026)	[77]

As suggested in Table 4-2, the critical Grashof number varies drastically between different systems. Various geometrical shapes have been treated in literature including vertical zone melting [78], horizontal Bridgman [79], shallow cavities [76],

and Czochralski growth [56]. In these publications, flow characteristics have been found to be highly dependent on fluid properties (Pr), heating conditions, and enclosure size. For example, smaller enclosure dimensions have a stabilizing effect on convection currents, resulting in a higher critical Grashof number [80]. The orientation of temperature gradients was also found to be important with respect to influencing fluid flow. For example, vertical temperature gradients cause much more unstable flow compared to horizontal gradients [81], and strong Marangoni flow (large surface area and surface temperature gradients) further complicates the 3-D flow [68].

Stirring conditions are very sensitive to material properties, heating conditions, and geometry. Therefore, it is difficult to estimate an exact critical Grashof number without a fluid dynamic model or specific experiments. However, since experiment parameters in this thesis have a similar magnitude to those in literature, the flow regime for the experiments can be approximated. Since, the measured Grashof numbers displayed in Table 4-1 are typically above the critical Grashof numbers from literature (Table 4-2), it can be postulated that all experiments exhibit oscillatory flow. For example, the lowest measured Grashof number was 6.2×10^5 (Test 5, Plane 'D'), which was higher than all values found on Table 4-2.

4.2.4 Marangoni Flow

The driving force for Marangoni flow requires a surface temperature gradient at a fluid/melt interface [40]. In contrast, when liquid is in contact with a solid, it obeys a no-slip condition tangential to the rigid boundary. For example, according to Kuhl et

al. [42], thin oxide layers, or suitable liquid encapsulants, are often used to cover the melt surface completely in order to avoid Marangoni flow. Even though the experiments in this thesis were conducted under a hydrogen atmosphere, an unidentified film consistently developed on the surface of the lead. As shown in Figure 4-7, the film covered the entire surface of the molten zone.



Figure 4-7: Surface film covering the molten zone during lead experiments

The film had a crusty, matte appearance in contrast to the mirror-like appearance of pure molten lead. In addition, considerable effort was required to remove the film from a solidified ingot using a wire brush, demonstrating its substantial thickness. Due to the presence of this encapsulating film, thermocapillary flow is not considered in the data analysis of the lead experiments.

In contrast, no film is created during routine zone refinement of indium antimonide at Firebird Technologies, as shown in Figure 4-5. To estimate the significance of what surface tension flow would be in the absence of a surface film, the Marangoni number was calculated from temperature data. Surface temperatures were approximated by using the maximum temperature of the top thermocouple from each test. The highest Marangoni number of all tests was calculated from data gathered from Test 4 as follows:

$$Ma = \frac{(d\sigma/dT)L\Delta T}{\alpha\mu} = \frac{0.13 \times 10^{-3} \cdot 0.018 \cdot 7}{2.65 \times 10^{-3} \cdot 9.49 \times 10^{-6}} = 651 \quad (4-2)$$

Where $(d\sigma/dT)=0.13 \times 10^{-3}$ N/(m·K) [82] is the change of surface tension with temperature, $L=0.018$ m is the depth in Test 4, $\Delta T=7.0$ K is the maximum surface temperature minus the melting temperature for Test 4, α is the thermal diffusivity of lead (Table 2-2), and μ is the kinematic viscosity of lead (Table 2-2).

According to numerical simulation experiments of small enclosures [83], the critical Marangoni number for oscillatory flow is approximately 115 for Si (Pr= 0.0065), and 606 for GaAs (Pr=0.068). The calculated value from Equation (4-2) is similar in magnitude (Ma=651 for Pr=0.026 of lead) therefore it can be concluded that there are sufficient temperature gradients for surface tension flow. From this analysis, it can be concluded that if similar temperature gradients existed in the absence of a surface film, surface tension flow will likely contribute to the overall convection in the molten zone.

4.3 Analysis of Temperature Fluctuations

Fine temperature fluctuations can be used to characterize the rate of convective movement and fluid flow patterns. This section will demonstrate that the complexity of the temperature signal varies according to the complexity of fluid movement. For example, characteristic frequencies develop in the temperature signal during the onset of oscillatory flow. Several tools in Matlab 7.1 were used for signal analysis including a discrete Fourier transform, wavelet power spectrum, and power spectral density tool. The Fourier transforms were calculated with a function called 'FFT' to identify characteristic frequencies in the signal. The wavelet power spectrum tool was developed by the process control group at the University of Alberta [82] and was used to visualize the different frequencies within the molten zone. This provides qualitative information on the location and intensity of these fluctuations. In addition, a power spectral density function called 'PEROIDOGRAM' was used to quantify the complexity of the signal.

A thorough explanation of the characteristics of oscillatory flow can be found in Henry et al.[74], while a description of the physical meaning behind de-stabilizing currents is provided by Gill [85]. In order to visualize the characteristics of oscillatory flow, a typical stream function is shown in Figure 4-8 [56]. The darkest regions on the figure correspond to the highest fluid velocity.

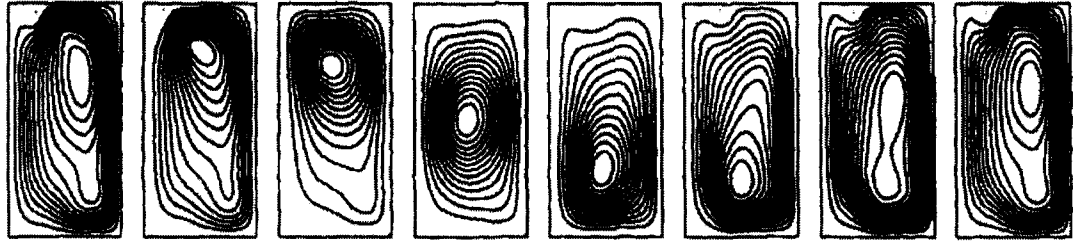


Figure 4-8: Oscillatory flow-Numerically calculated stream function of a fluid (Horizontal plane, $Ra/Pr Re_2=0.929$, $\Delta T=20s$) [56]

Prior to analysis, the high frequencies associated with fluid movement were isolated from the raw signal using a high pass (see Appendix C).

4.3.1 Discrete Fourier Transform

Abernathy et al. [86] used thermocouples to measure temperature oscillations in xenon gas, and applied Fourier transform algorithms to calculate the characteristic frequency of the oscillations. As shown in Figure 4-9, temperature fluctuations exhibit higher amplitude and more complex frequency content with more developed fluid flow.

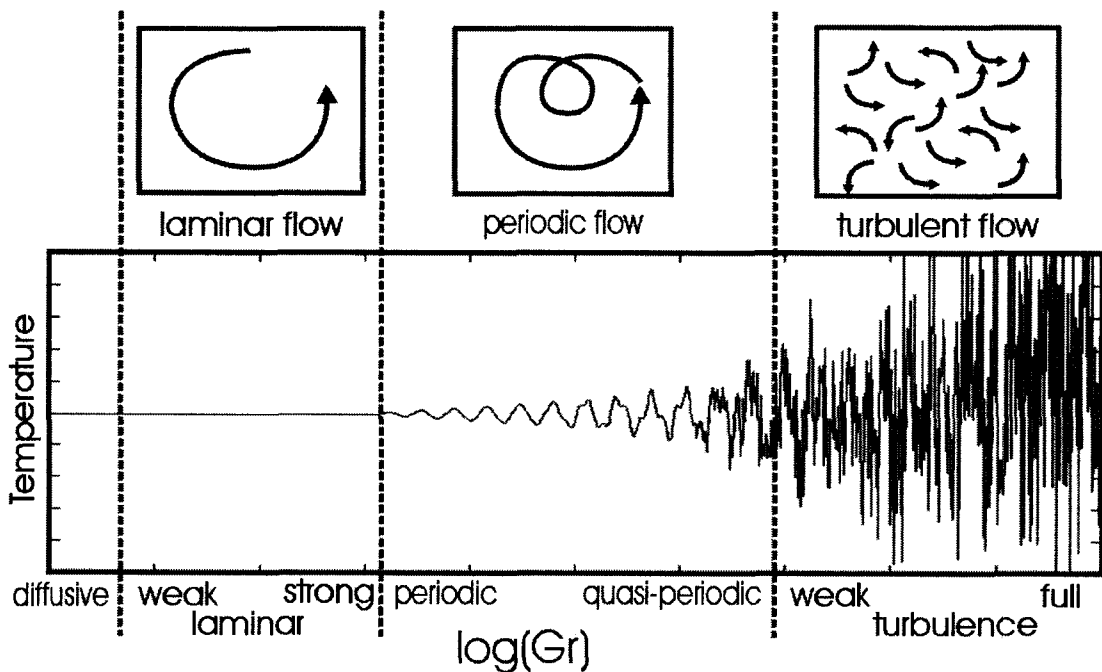


Figure 4-9: Temperature oscillations in relation to fluid flow regime [86]

Figure 4-9 shows that, under laminar convection, the temperature is typically constant at a stationary point. This relationship holds until the onset of periodic flow, upon which characteristic frequencies develop in the velocity and temperature fields. At higher Grashof numbers, the flow regime becomes more complicated and the characteristic frequencies continue to multiply and become more complex. In fully developed turbulence, the temperature signal is identified by no discernable periodicity and widely varying amplitudes and frequencies [46].

In literature, it is shown that the period of an oscillation is dependent on the geometry of the enclosure and rate of fluid movement [73]. Depending on system, characteristic frequencies such as 0.01-0.015 hertz [87], 0.015-0.02 hertz [88], 0.08 hertz [61], up to 0.15 hertz [89] have been cited. In this thesis, the characteristic frequencies varied widely according to location and differed from experiment to experiment. Using discrete Fourier transforms, the range of characteristic frequencies common in the experiments are shown. All samples were based upon 10 millimetres of travel or 6500 data points.

Figure 4-10 shows the Fourier transform from a thermocouple embedded in solid metal between 5 and 15 millimetres from the freezing interface, collected from the lower-mid thermocouple of Test 5. There is one characteristic frequency at 0.069 hertz, however, it can be neglected because of its low power (0.051).

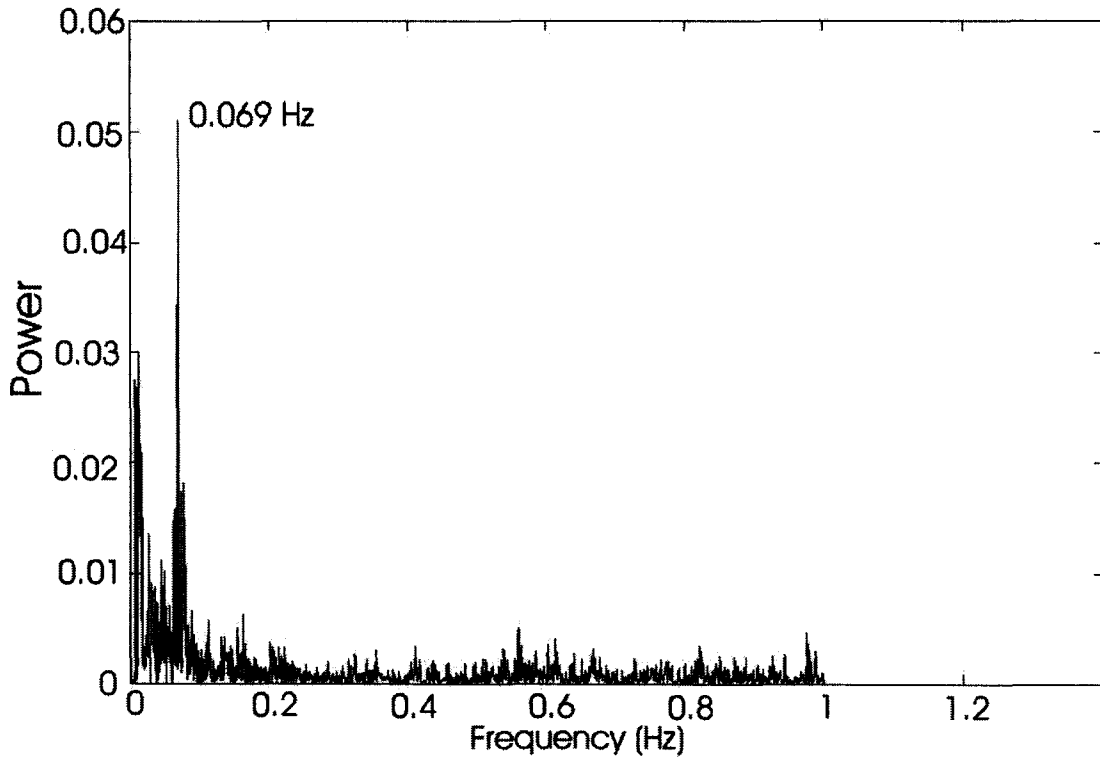


Figure 4-10: Fourier transform of a solid region of Test 5, Plane 'C', bottom thermocouple

Figure 4-11 shows the Fourier transform for a simple signal within the molten metal. The sample was taken from the bottom thermocouple of Test 5, plane 'C', adjacent to the freezing interface. As discussed later in Section 4.3.3, this sample exhibits the lowest complexity of fluid flow of all experiments. Note that there is one main frequency at 0.073 hertz accompanied by some lower frequencies. The power of this characteristic frequency (11) is over 200 times higher than the most significant frequency in Figure 4-10.

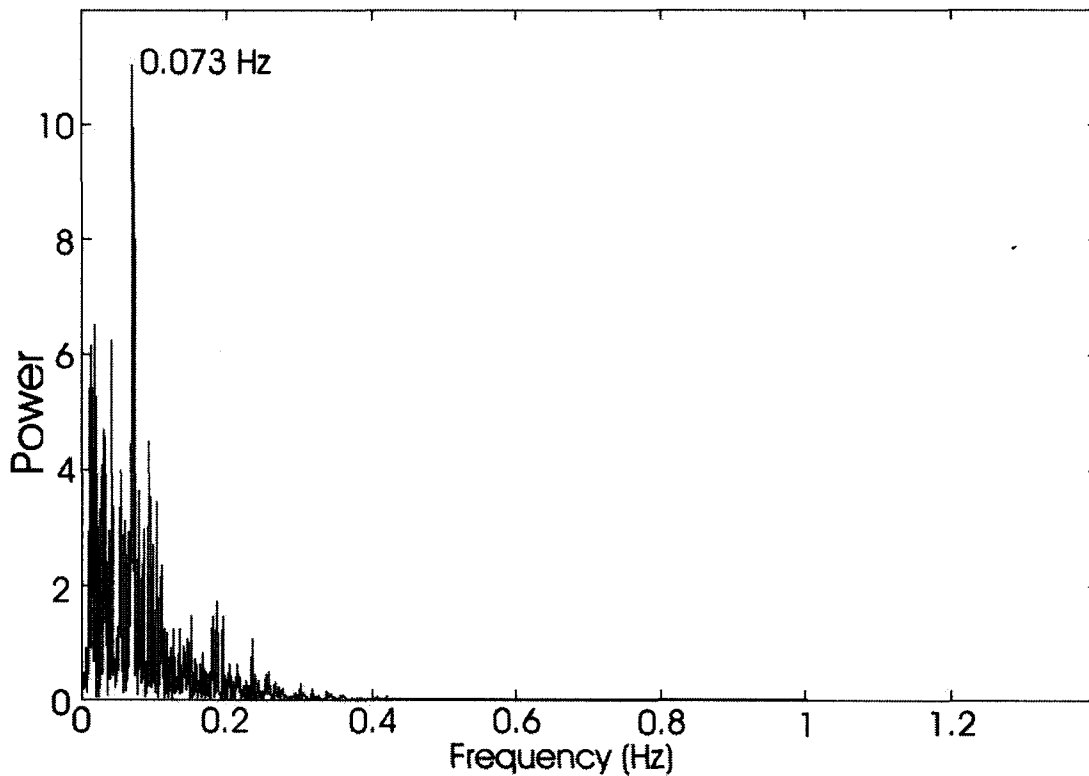


Figure 4-11: Fourier transform of a simple liquid sample, Test 5, plane 'C', bottom thermocouple, adjacent to the freezing interface

Figure 4-12 shows the Fourier transform for a complex signal within the molten zone. The sample is taken from the upper mid thermocouple of Test 1, plane 'C', adjacent to the melting interface. As discussed in Section 4.3.3, this sample exhibits the highest complexity of fluid flow of all experiments. Note that there are several main frequencies. The power of the highest frequency is about 4 times higher than the most significant frequency in Figure 4-11.

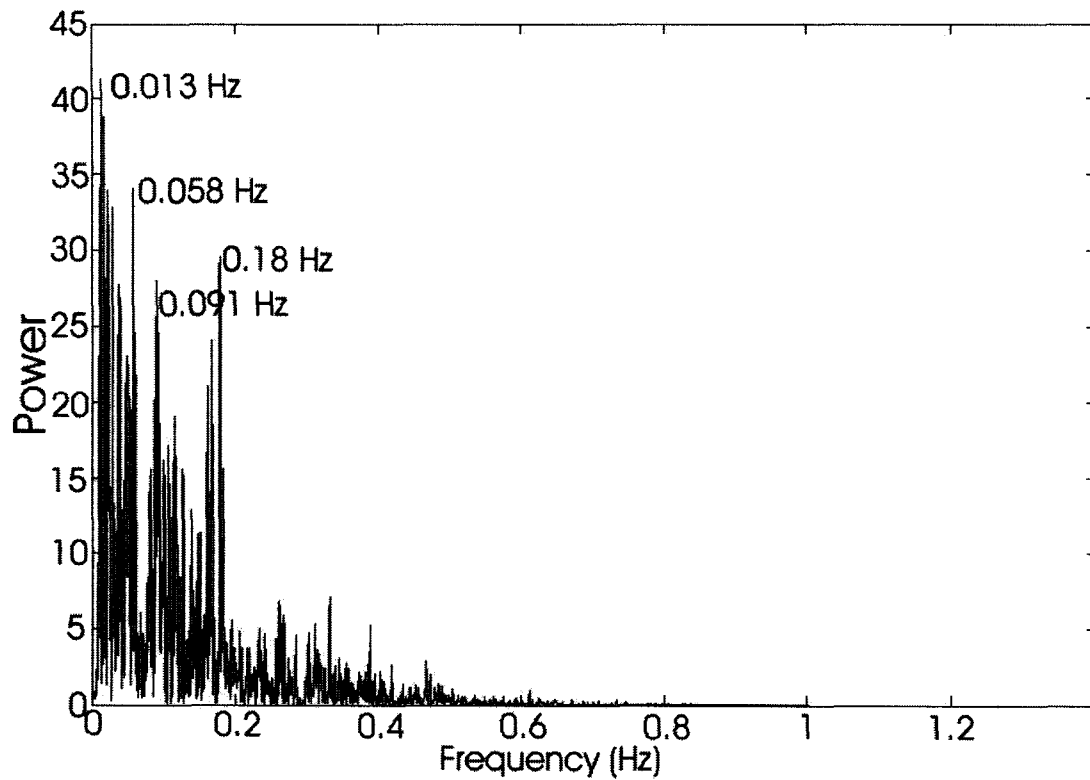


Figure 4-12: Fourier transform of a complex liquid sample, Test 1, plane 'C', upper-mid thermocouple adjacent to the melting interface

To summarize the frequency content of the experiments, the most prevalent frequencies tended to be in the range of 0.05-0.2 hertz (period of 20-5 seconds). The oscillations typically vary in power and frequency throughout the melt. Although some of the tests exhibit a broader frequency spectrum than others, usually there were several dominant frequencies characteristic of quasi-oscillatory convection [90]. Typically in literature, only a small range of Grashof numbers exhibited strictly oscillatory convection and therefore the most likely regime is quasi-periodic [42]. In very low Prandtl number fluids, heat transfer rate is not largely affected by different rates of convection [70]. Flow patterns very readily become time dependent because

large Nusselt numbers (see Table 2-1) are difficult to obtain [81]. No test exhibited a continuous spectrum of frequencies as one would expect for a turbulent regime [70].

4.3.2 Visualization of Frequency Spectra

In order to visualize frequency changes in the temperature signal, the Data Visualization and Analysis (DVA) toolbox for Matlab 7.1 was used. Plots were created using the Wavelet Power Spectrum function to show that the location and intensity of frequencies varied within the zone. The function creates a three dimensional image to depict the location and intensity of fluctuations within the zone. Two minor graphs accompany the main plot to make it easier to understand. Next to the x axis, the high pass filtered temperature signal is shown. On the y axis, the Fourier transform is included to show the frequencies contained within the signal. On the main figure, the x axis has units of time, the y-axis displays the period of oscillations, and amplitude of oscillations represented by color, red being the highest.

Each wavelet spectrum plot represents a single thermocouple. In order to map the entire molten zone, four wavelet plots are shown for Test 2, pass 2 (Figure 4-13, Figure 4-14, Figure 4-15, and Figure 4-16), one for each thermocouple. The associated contour plot is also shown in Figure 4-17.

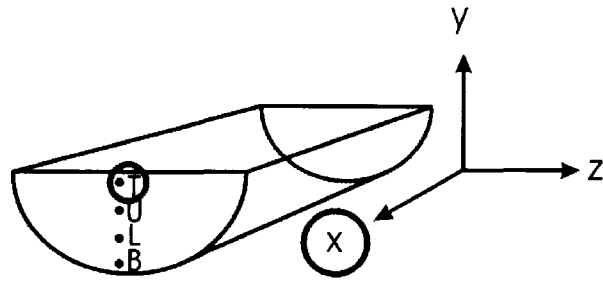
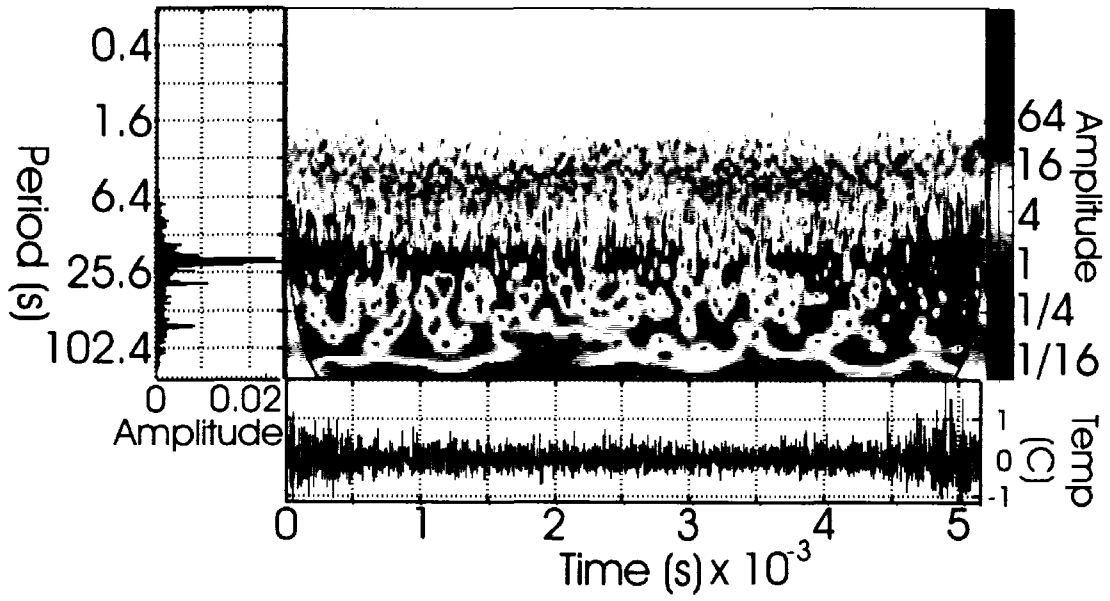


Figure 4-13: Wavelet Power Spectrum plot for Test 2, plane 'C', top thermocouple, pass 2

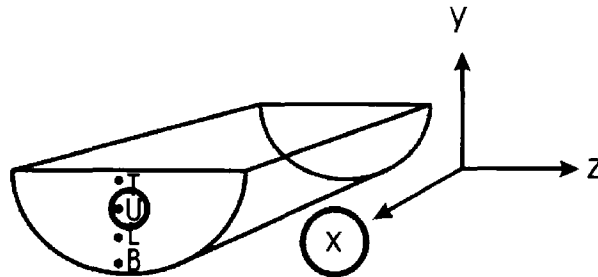
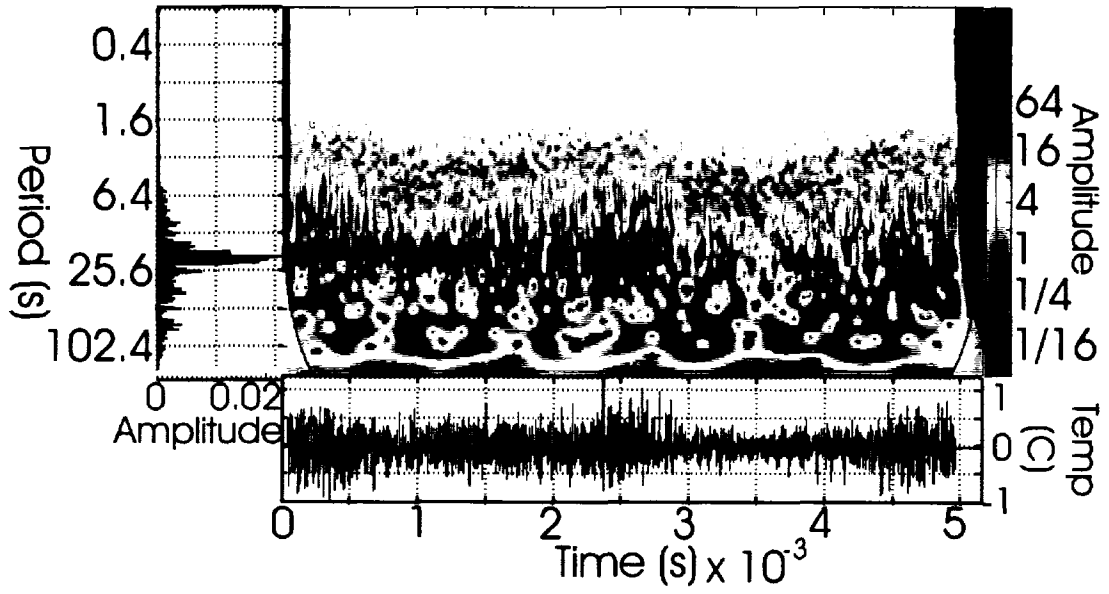


Figure 4-14: Wavelet Power Spectrum, Test 2, plane 'C', upper-mid thermocouple, pass 2

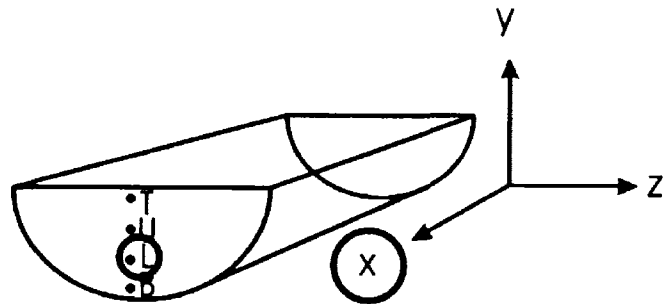
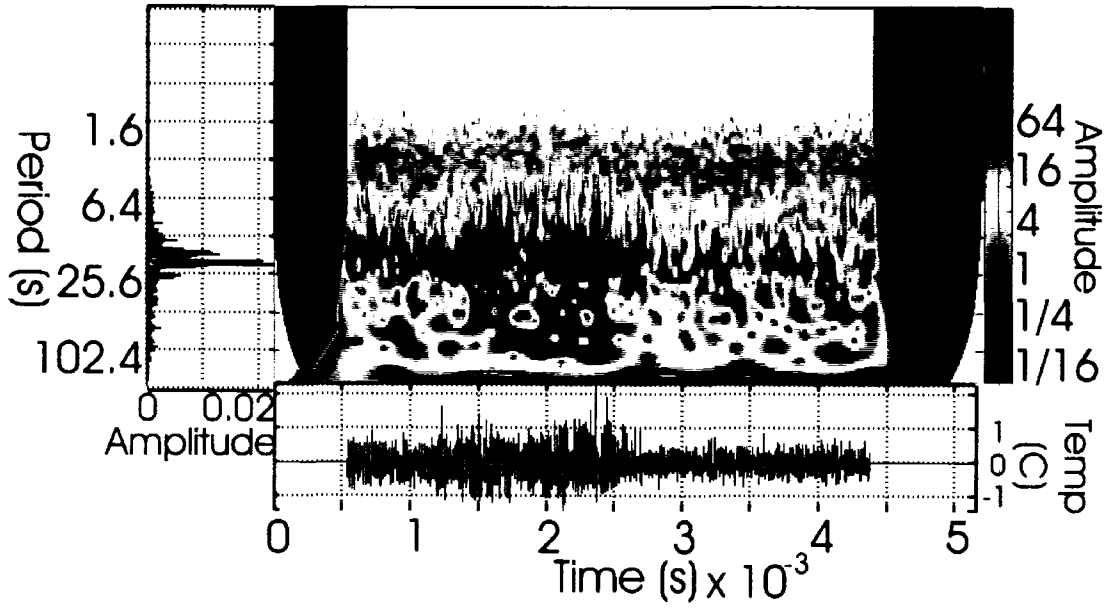


Figure 4-15: Wavelet Power Spectrum, Test 2, plane 'C', lower-mid thermocouple, pass 2

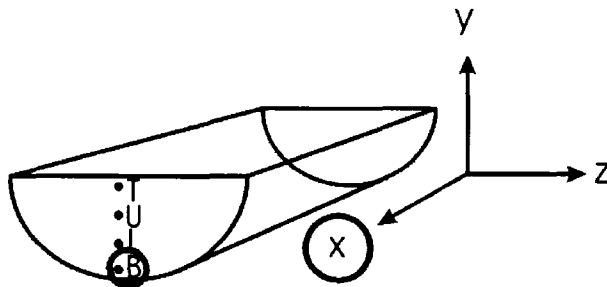
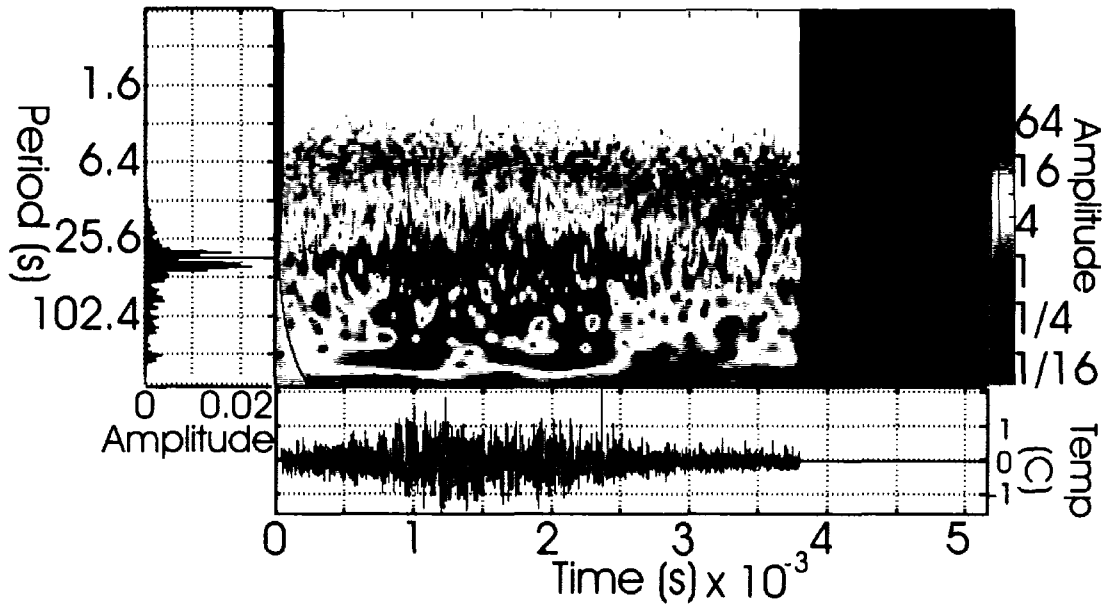


Figure 4-16: Wavelet Power Spectrum, Test 2, plane 'C', bottom thermocouple, pass 2

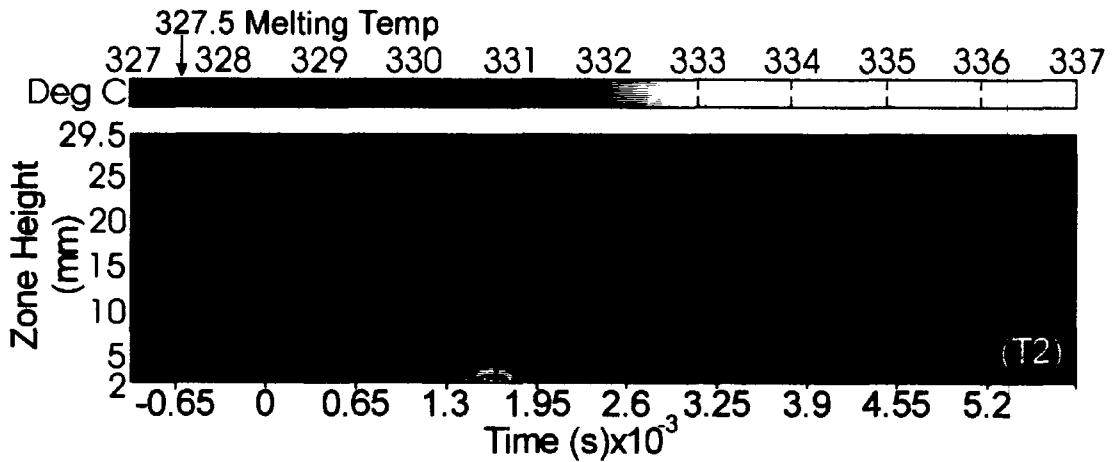


Figure 4-17: Contour plot for Test 2, pass 2

Since time is shown on the x-axis, the left side of the diagram represents the melting interface while the right side of the diagram represents the freezing interface. The y-axis shows the period of oscillations; the highest frequencies (short period) are near the top of the diagram while the low frequencies (long period) are shown on the bottom. For example, if low frequencies are dominant at the melting interface, the bottom left portion of the diagram will be deep red. Note that the amplitude on the Fourier transforms are scaled differently than the color plots. All temperature gradients mentioned in the following discussion can be visualized in the contour plot shown in Figure 4-17.

Figure 4-13 represents the frequency content of the top thermocouple (29.5 millimetres in Y direction) from the above contour plot. Notice that the most active frequencies have a period of about 20 seconds (0.05 hertz) and occur primarily near the interfaces where the highest temperature gradients are found. The complexity of temperature signal in these regions probably occurs due to fluid moving down adjacent to the cool interfaces. In comparison, the freezing interface is a more active region than the melting interface.

The upper-mid thermocouple in Figure 4-14 (situated at 21.5 millimetres in the Y direction) shows regions of activity adjacent to the interfaces and directly above the peak temperature. This activity is indicative of hot fluid moving upwards from the peak temperature and cool fluid moving down near the interfaces. In general, the upper-mid thermocouple is more active than any other thermocouple.

The lower-mid thermocouple shown in Figure 4-15 (situated at 10 millimetres in the Y direction) indicates that there is less activity next to the interfaces, but high complexity in the centre. This is because the thermocouple is close to the bottom peak temperature where fluid is moving upwards at a high velocity.

The bottom thermocouple (located at 2 millimetres in the Y direction) shown in Figure 4-16 displays almost no fluid movement next to the interfaces and the highest activity in the middle corresponding to the temperature peak at the bottom. Notice that the highest activity surrounds the peak in regions with high temperature gradients but weakens directly at the hot spot where there is likely a small stagnant region [91] (25 millimetres in the Z direction).

From analysis of these wavelet spectrum plots for Test 2, it is assumed that fluid is moving down adjacent to the interfaces and up through the centre of the zone. This is indicative of toroidal flow represented in Figure 4-18. Examples of this fluid flow pattern are shown in literature using radioactive tracing of Pb and Sn where the enclosure is heated from below and cooled from both end walls [91].

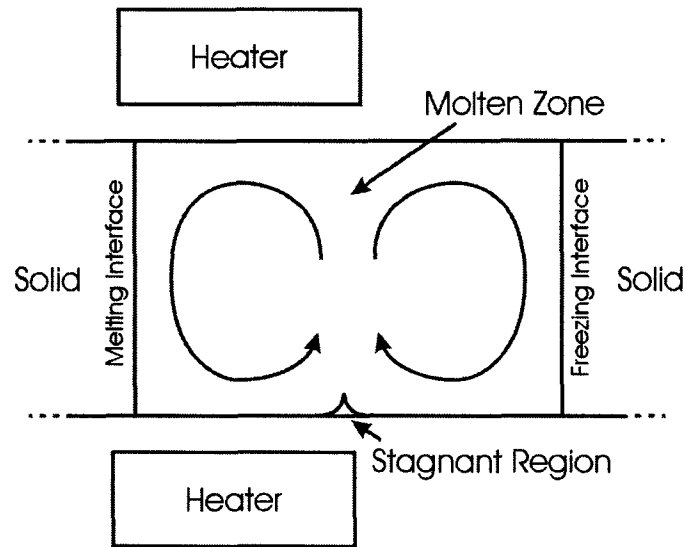


Figure 4-18: Representation of toroidal flow [40]

Additional wavelet spectrum plots for Tests 1, 3, 4, and 5 are given in Appendix D. In Tests 1 and 3, the most convective activity is found at the bottom of the zone near the melting interface and at the top of the zone near the freezing interface. This corresponds to regions of high temperature gradients as shown in Figure 4-3. As a possible interpretation, fluid may be moving clockwise in a single large convection cell. On the other hand, convective cells are not as discernable in shallower depth experiments (Tests 4 and 5). This is consistent with literature which cites that a smaller aspect ratio results in smaller, more numerous eddies [68]. It is also possible that toroidal flow exists in the shallow depths, but there are an insufficient number of data points to discern it.

In literature, fluid flow visualization experiments commonly involve the observation of a transparent fluid. Geometries common to crystal growing operations have been explored using sodium nitrate ($Pr=9.2$) [92], succinonitrile ($Pr=23$) [93], and silicone oil ($Pr=6.8$) [94] to reveal characteristic flow patterns. The disadvantage is that all

available test fluids have a relatively high Prandtl number. Observations are therefore not easily transferable to low Prandtl number systems like that of semiconductors [42]. For example, experiments using sodium nitrate showed laminar flow uncharacteristic of semiconductor melts [92].

4.3.3 Power Spectral Density

For the purpose of quantifying the complexity of fluctuations in the temperature signal, a function in Matlab 7.1 called 'PERIODOGRAM' is used. The function computes an unbiased estimate of the power spectral density based on the scaled, squared, discrete Fourier transform [95]. Sample size was kept constant throughout all calculations based upon the equivalent of 1 cm of heater travel or 6500 data points. The number of calculation windows was chosen to be half the sample size and the frequency resolution was 0.00308 hertz within the domain of 0 and 5 hertz. The power spectral density is normalized so that the variance is equal to its mean and is expressed in units of power per radians per sample. Because these units do not have any physical relevance, different samples are compared by counting the number of frequencies whose power exceeds a threshold value. The threshold (0.01) was chosen so that the sample with the lowest peak power (Sample 5, bottom thermocouple, Table 4-3) had a significant threshold count (114), providing good resolution between tests. As a reference point, this number represents the simplest signal and the lowest flow complexity. A broad frequency band width would exhibit a higher threshold count representing a high complexity of fluid flow [76]. The highest threshold count (462) was found in Test 1, upper-mid thermocouple, as shown in Table 4-4.

Table 4-3: Sample spectral density for Test 5, plane 'C', pass 3

Test 5 Sample #	Thermocouple Location	
	Lower-mid	Bottom
1	148	134
2	146	143
3	150	179
4	141	142
5	136	114
6	150	

Table 4-4: Sample Spectral Density for Test 1, plane 'C', pass 2

Test 1 Sample #	Thermocouple Location			
	Top	Upper-mid	Lower-mid	Bottom
1	404	462	286	216
2	359	422	229	210
3	405	414	185	164
4	382	354		141
5	396	439		

For each test, the molten zone varies slightly in size. In addition, the bottom is often narrower than the top because of the sloped interfaces. As a result, the number of samples in each zone varies because the signal length is different. The total number of threshold counts for each zone is therefore an inappropriate reference. To solve this problem, the maximum threshold count for all passes is averaged for each test, and displayed on Figure 4-19 and Table 4-5. This graph represents the maximum complexity of convection for each test condition. For comparison, the Grashof numbers calculated in Section 4.2.2 are included on Figure 4-19. Note that the power spectral density and the Grashof number follow the same trend with declining intensity of bulk convection from Test 1 through Test 5.

Table 4-5: Maximum power spectral density threshold for all tests, averaged between passes

Test Number	Average Maximum Threshold Count
1	412
2	382
3	240
4	202
5	171

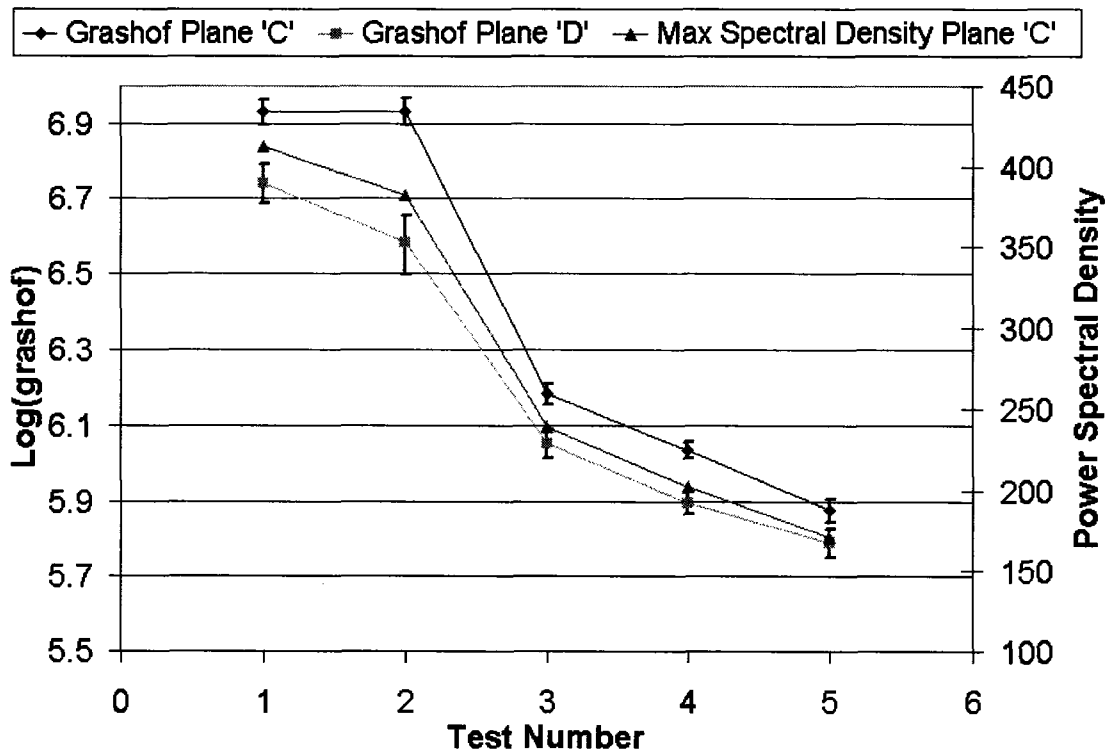


Figure 4-19: Averaged maximum power spectral density and Grashof number for each test

The level of stirring within the bulk of the zone is important because it gives an indication of how well the fluid is being mixed. However, as shown in 2.5.3, much of the mass transport important to segregation occurs at the freezing interface. To get a better indication of the convection activity adjacent to the interfaces, the local power spectral density was calculated. The threshold count at the interfaces is averaged between passes for each test, and the tests are compared in Figure 4-20 and Table 4-6.

Table 4-6: Threshold count at the interfaces, averaged between passes

Test Number	Threshold Count	
	Melting Interface	Freezing Interface
1	305	277
2	266	251
3	170	171
4	156	137
5	145	142

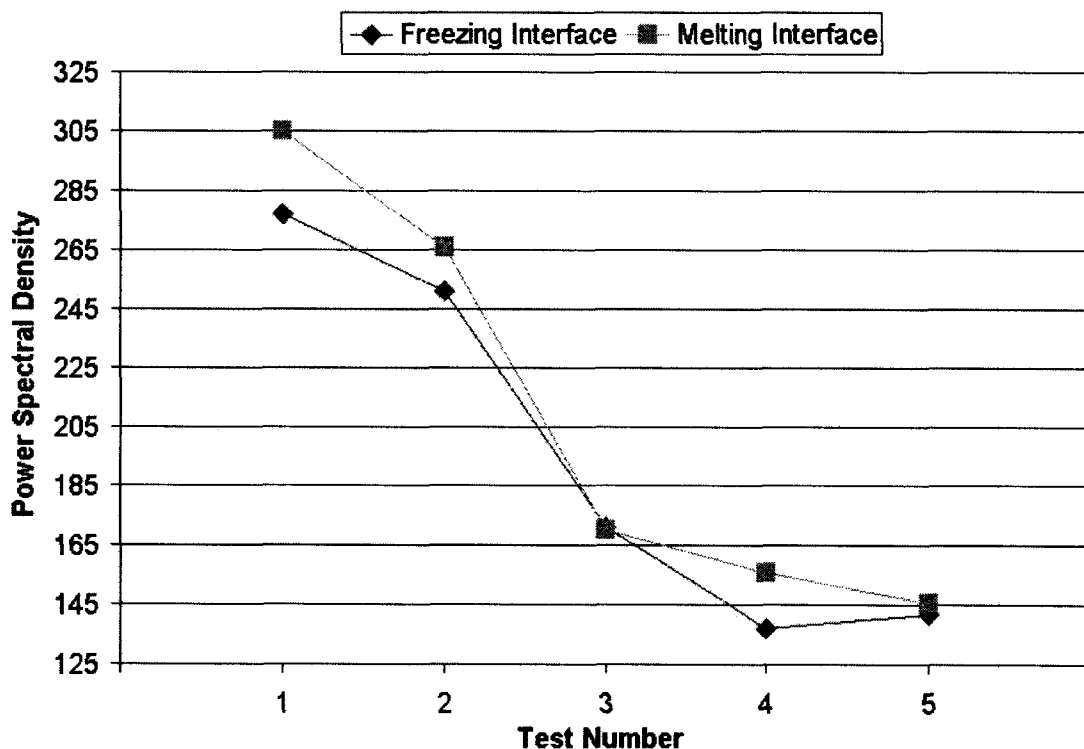


Figure 4-20: Power spectral density at the freezing and melting interfaces, data gathered from plane 'C'

According to Figure 4-20, the melting interface typically experiences higher complexity of convection than the freezing interface. This is attributed to the position of the melting interface relative to temperature gradients within the zone. As described in Section 4.2.1, the peak temperature is commonly situated closer to the melting interface. As a result, the temperature gradients adjacent to the melting interface are higher than at the freezing interface.

The spectral density at the melting interface decreases from Test 1 through to Test 5 similar to the max spectral density trend in Figure 4-19. However, this trend is not consistent at the freezing interface. According to Figure 4-20, the lowest convection complexity at the freezing interface occurs during Test 4. Upon closer examination, it was found that spectral density at the freezing interface is dependent on the distance between the heater and the freezing interface. In Test 5, insulation was added in front of the heater to reduce the bulk convection rate (see Figure 4-19). As a side effect, the zone shifted closer to the front of the heater due to a change in the external temperature gradients. The end result is a decrease in distance between the freezing interface and the heater. Since higher temperature gradients are typically experienced in close proximity to the heater (see Section 4.2.1), Test 5 experienced an increase in the fluid movement complexity at the freezing interface. As shown in Figure 4-21, the freezing interface is furthest from the heater during Test 4 and experiences the lowest convection complexity. As suggested in Section 4.1, it is also possible that electrostatic interference may increase in close proximity to the heater.

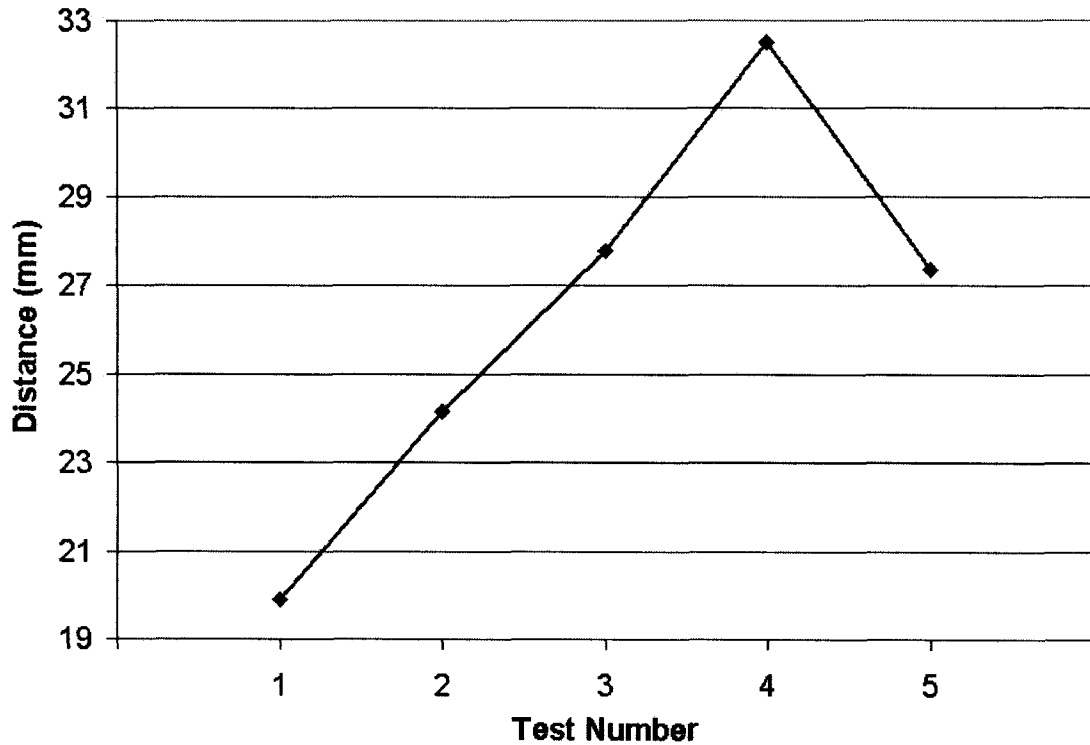


Figure 4-21: Average distance between the heater and the freezing interface for plane 'C'

Figure 4-22 shows that the greater the distance between the interface and the peak temperature of the zone, the lower the spectral density at the interface. Each test is plotted independently because the driving force for convection is significantly influenced by zone dimensions. Note that Tests 1 and 2 as well as Tests 4 and 5 have the same zone depth and exhibit a similar trend.

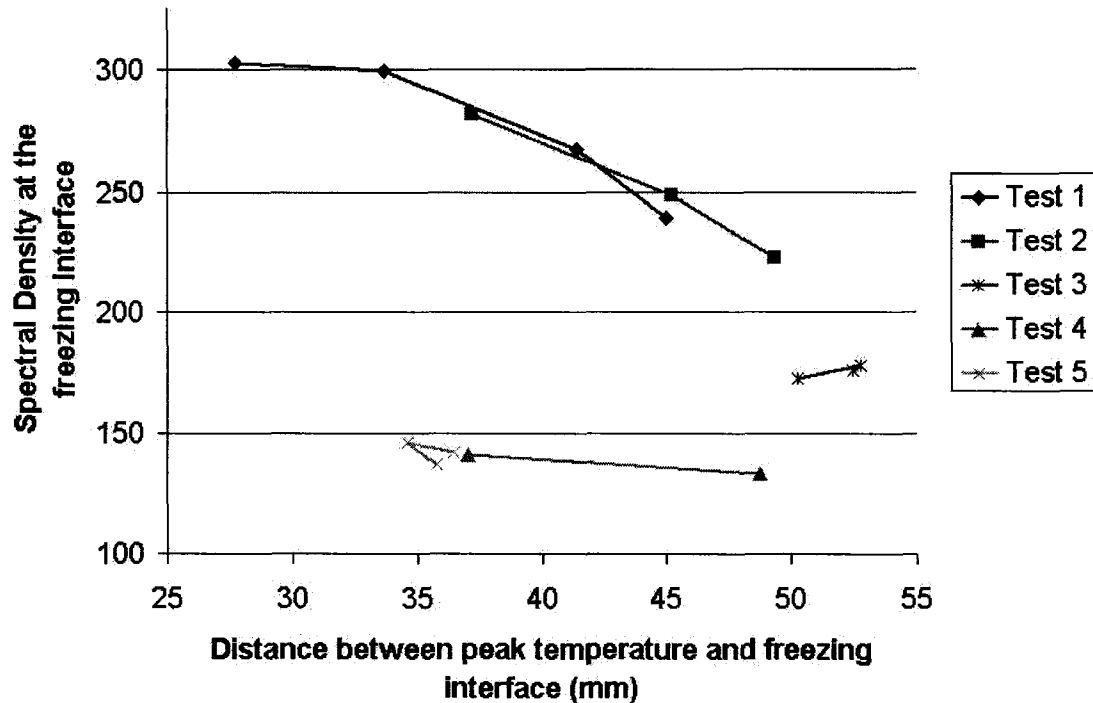


Figure 4-22: Power spectral density versus the distance between peak temperature and freezing interface for plane 'C'

In this section, it was shown that the convection complexity at the freezing interface is dependent on the bulk convection throughout the zone. However, placement of insulation can cause deviations in local convection complexity. For example, insulation used to change the distance between the freezing interface and the heater was found to influence the temperature gradients at the freezing interface. By decreasing this distance and increasing local temperature gradients, an increase in the convection complexity at the freezing interface was observed.

4.4 Assay Tests

As mentioned in Section 3.3.1, assay tests were done to measure the concentration profile of the different test conditions. For these assay tests, boundary conditions were repeated for Tests 3, 4, and 5 in the absence of thermocouples. The ingots were then sampled at 10%, 50% and 80% of ingot length and characterized using GDMS. In

order to compare test results, assays were fitted to a mass balance model to estimate a distribution coefficient that best suits the assay data. The test with the distribution coefficient furthest from unity is considered to have the best separation efficiency. Using knowledge of the convection characteristics for each set of boundary conditions, a correlation can be drawn between operating conditions and separation efficiency.

4.4.1 Mass Balance Model

A mass balance model (see Appendix E) was written in Matlab 7.1 based upon the equations described in Section 2.1. The model calculates an impurity profile based upon separation efficiency (k_{eff}), initial concentration, number of passes, and zone length as a ratio of normalized length. As explained in Section 3.3.1, zone length changes slightly throughout the experiments because of varying thermal conditions down the length of the bar. However, the zone length was assumed constant for all tests to keep the model simple. To provide a good estimate, zone length from all passes during thermocouple Tests 3, 4, and 5 were averaged (70 millimetres).

4.4.2 Separation Efficiency

The distribution coefficient (k_{eff}) for each test is calculated by fitting the mass balance model to assay data. As shown in Appendix F, the model calculates an impurity profile based upon an arbitrary value of k_{eff} . It then reiterates the calculation based on an adjusted k_{eff} value, determined from a linear least squares algorithm that compares the impurity profile to experimental data. An example of this approach can be found in literature where experimental data was matched to Scheil's normal freezing equation using the linear least squares method [96]. The calculated impurity profile

for iodine in Test 5 is shown in Figure 4-23, superimposed on experimental data. Calculated k_{eff} values are shown in Table 4-7 for iodine, chlorine, arsenic and copper. Unprocessed assay data is shown in Appendix F.

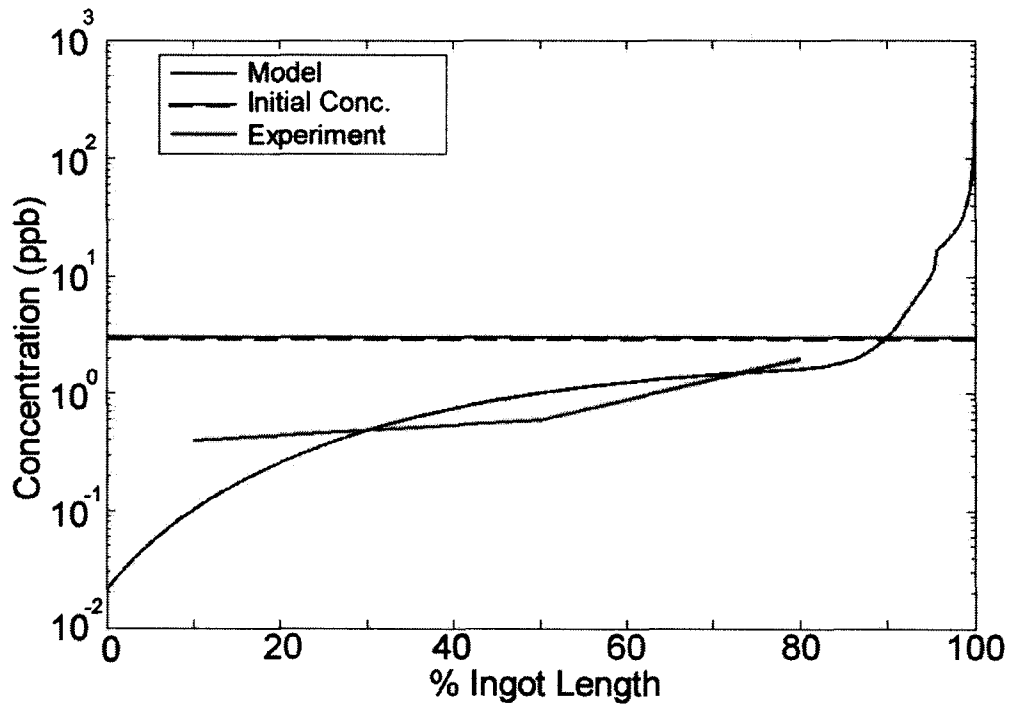


Figure 4-23: Best fit model to Iodine, Test 5 (calculated $k_{eff}=0.41$)

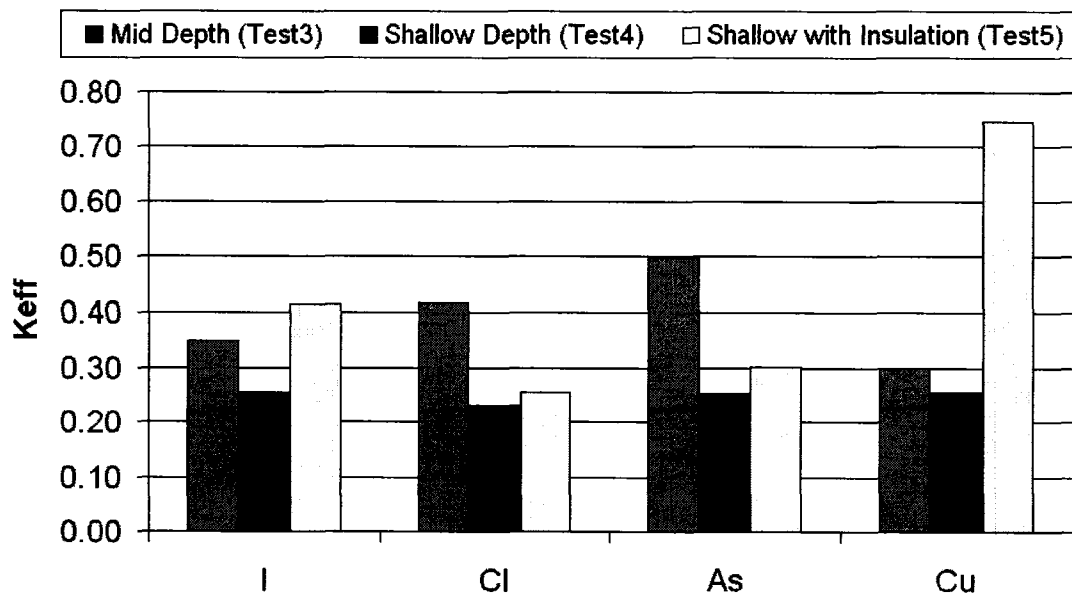


Figure 4-24: Calculated effective distribution coefficient (k_{eff}) fitted to assay data

The most striking trend found on Figure 4-24 is that Test 4 consistently has the best performance for separation. Neither Test 3 nor Test 5 asserts superior separation characteristics over the other. This is plausible since, as shown in Section 4.3.3, the convection rate at the freezing interface is similar in both tests.

As mentioned previously, glow dispersion mass spectrometry (GDMS) was used to measure impurity content of the chemical assays. This technique is capable of resolution down to part per billion concentrations for most impurity elements [97], however not all impurities were found in reasonable concentrations. Some impurities showed signs of contamination where, regardless of location in the bar, the content exceeded that of the initial concentration. For example, antimony had been processed using the same equipment and therefore showed erratic concentration patterns. Boron was found in large concentrations because of the boron nitride non-wetting agent sprayed on the boat prior to experiments (see Section 3.1). Other impurities such as magnesium were simply below the detection limit.

After zone refining, a monotonic impurity profile is expected. Some impurities were not redistributed throughout the bar in such a fashion, but decreased throughout the entire length of the bar. This may be attributed to high vapor pressure of the impurities and evolution at high temperatures. For example, sulfur has a very high vapor pressure of 10.9 atm at 377°C [44] and its concentration reduced dramatically throughout the bar. In contrast, copper has a very low vapor pressure at 2.2×10^{-8} atm at 377°C [44] and gave very consistent results. Also, if volatile impurities are

vaporized and then freeze on cold regions of the ingot, they may be re-incorporated into the metal on the subsequent pass. This is known as shunting and can inhibit the separation potential of some impurities [98]. Additional sources of discrepancy between the experiment and model could be attributed to slight variation of zone length during the experiment, changing thermal and fluid flow conditions from one end of the bar to the other, and possible interaction of impurities.

Table 4-7 shows the standard deviation of test data with respect to the calculated impurity concentration distribution. These four impurities were chosen for examination because they exhibited the lowest standard deviation of all impurities. The shape of the impurity profile is therefore similar to what can be expected from the mass balance model. Note that the theoretical separation coefficients are much lower than measured values. This emphasizes the discrepancy between the thermodynamic potential for segregation and the limitations due to the rate of transport processes. Because there is such a drastic difference between theoretical and measured segregation coefficients, there is ample opportunity to improve separation efficiency by manipulating transport processes.

Table 4-7: Calculated separation coefficients and the corresponding standard deviation data

Element	k	k _{eff}			Standard Deviation (fraction of initial concentration)		
		Test 3	Test 4	Test 5	Test 3	Test 4	Test 5
I	n/a	0.35	0.26	0.41	0.17	0.1	0.15
Cl	n/a	0.42	0.23	0.26	0.11	0.06	0.28
As	0.02 [20]	0.50	0.25	0.30	0.36	0.12	0.17
Cu	0.04 [20]	0.30	0.26	0.75	0.09	0.04	1.74

4.5 Summary of Experimental Results

In this chapter, a discussion of experimental analysis revealed characteristics of the fluid flow within the molten zone, and quantified the segregation rate under various operating conditions. Using thermal data gathered from thermocouples, the dominant convection regime was shown to be time dependant flow. The lowest complexity of convection at the freezing interface was recorded in a test with the lowest ingot depth and largest distance between the freezing interface and heater. This relationship indicates that convection can be controlled within the molten zone by manipulating boundary conditions such as ingot depth and insulation. Using Glow Discharge Mass Spectrometry, the composition of the ingot was measured after zone refining under various operating conditions. The concentration profile was then used to calculate separation efficiency by fitting the data to a mass balance model using a linear least squares technique. The best segregation efficiency was measured during experiments with low convection complexity at the freezing interface. From this discussion, it is clear that there is a strong relationship between the operating conditions such as ingot depth and thermal conditions surrounding the molten, and separation efficiency. Chapter 5 will discuss ways to improve the separation efficiency by manipulating these operating conditions.

Chapter 5 Improving Separation Efficiency

The goal of this project is to identify operating conditions that will improve separation efficiency of the zone refining process. By studying how the transport phenomena interact and are controlled with varying operating parameters, separation can be influenced. In Chapter 2, it was determined that the rate and nature of convection is instrumental to segregation. The purpose of experimentation was to identify the convection characteristics typically experienced in industrial equipment, learn how to control convection, and quantify how separation efficiency is affected. In this chapter, a connection between convection characteristics and separation efficiency will be drawn, the ideal situation for separation will be identified, and suggestions for increasing separation by controlling operating conditions will be proposed. All experiments were done using lead metal because of the inexpensive raw material and abundance of thermodynamic data. However, zone refining is applicable to a host of materials such as indium antimonide, germanium, and antimony. In order to transfer knowledge to other metals, a dimensional analysis is provided.

5.1 Separation Efficiency in Relation to Convection

According to the results presented in Chapter 4, it is apparent that convection within the molten zone can be manipulated drastically by varying its geometry and the surrounding thermal conditions. As supported by the decreasing Grashof number on Figure 4-6 and a lower magnitude of temperature oscillations on Figure 4-19, the level of convection is reduced by constricting the geometry and reducing external

temperature gradients. Transport theory indicates that a reduction in convection could result in two contradictory conditions affecting separation.

On one hand, lower convection rates would decrease the rate of stirring, thereby opposing the idealized assumption that the molten zone is perfectly mixed. In addition, the fluid velocity boundary layer thickness at the freezing interface would be smaller, slowing down mass transport in the region. A combination of these characteristics indicates a reduction in the separation efficiency with decreased fluid movement.

On the other hand, a reduction in convection would simplify the oscillatory nature of fluid flow, resulting in a more stable crystal growth rate. Without oscillations at the freezing interface, the microscopic interface velocity would be much lower. In literature, there is controversy whether these oscillations are detrimental to macro segregation (see Section 2.5.3). Considering microscopic interface velocity as the dominant phenomenon over boundary layer thickness, lower convection complexity could provide better separation efficiency. It is imperative to identify the true dominating phenomenon in order to properly adjust operating conditions and better control separation characteristics.

5.1.1 Dominant Transport Phenomenon

The challenge posed by this experimental study is to identify the convection regime typical of industrially scaled equipment, and manipulate the fluid movement rate to benefit segregation. Experimental analysis in Chapter 4 revealed that the dominant

fluid flow regime was quasi-oscillatory in all tests. No firm relationship was established between the bulk convection rates and separation efficiency. For example, even though bulk convection was less complex in Test 5 compared to Test 3 (Figure 4-19), there was no appreciable difference in segregation characteristics (Table 4-7). However, it was demonstrated that oscillations are dependent on the location within the melt and can deviate from the bulk fluid movement. While Test 4 had intermediate bulk convection complexity, it consistently experienced the lowest oscillation complexity at the freezing interface (Figure 4-20). In addition, it consistently experienced the best segregation rates. From this information, it can be concluded that local convection characteristics at the freezing interface are very important to the segregation rate

Brown et al. [40] predicted that variations in the fluid velocity field can result in an unstable segregation rate. The relationship between convection regime and separation characteristics is summarized in the curve provided in Figure 5-1.

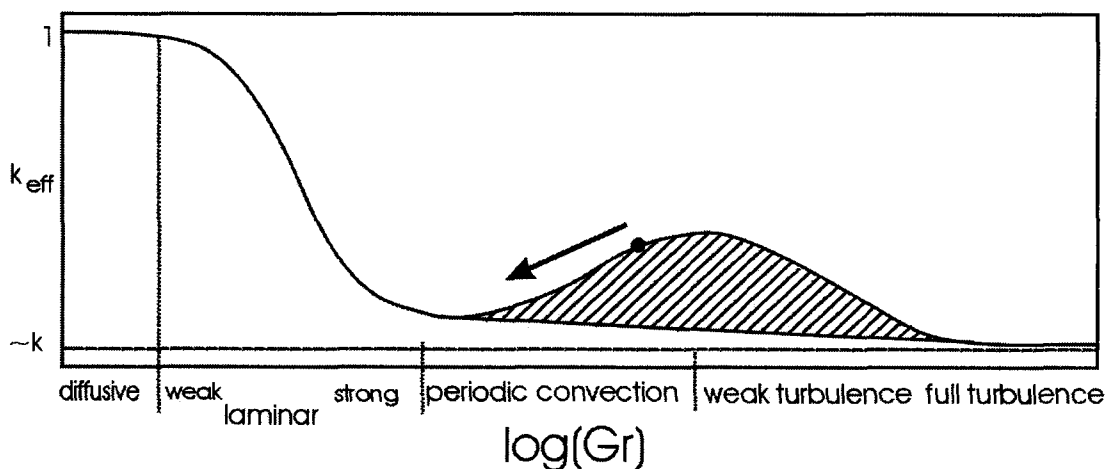


Figure 5-1: Qualitative relationship between convection and separation efficiency [40]

Figure 5-1 suggests that, as fluid flow increases in the laminar regime from left to right, there is an improvement in separation. As oscillations are introduced and intensify in the periodic regime, segregation becomes unstable because of increasing microscopic interface velocity. This is represented by the cross-hatched region in which the segregation rate fluctuates. It is hypothesized that the periodic regime is followed by a stabilization of the segregation rate during the onset of turbulence due to a reduction in interface velocity. Turbulent flows often exhibit higher frequencies which have a smaller impact on the heat flux at the interface [39] resulting in a decrease in interface instability.

All tests exhibited quasi-oscillatory convection, and the most effective separation occurred at low convection rates at the freezing interface. Using this information, the approximate convection regime found during the experiment is represented by the black circle on Figure 5-1. The arrow indicates the direction that convection should be controlled at the freezing interface to enhance segregation. Since we have very extreme stirring conditions in Test 1 and no turbulence, it is unlikely that segregation efficiency can be improved by pushing the system into the turbulent regime [70].

There is a unique opportunity to optimize separation by controlling the intensity of convection locally within the melt. By limiting convection at the freezing interface to minimize oscillations in the interface velocity, the best separation characteristics are expected. Different combinations of operating conditions are discussed in Section 5.2 with the goal of manipulating the fluid movement within the molten zone.

5.2 Beneficial Control Measures

In Chapter 4, it was demonstrated that oscillations are generally less prominent with lower Grashof numbers, and regional convection currents can be further manipulated by external temperature gradients. This section discusses possible control measures to limit convection at the freezing interface thereby reducing oscillations in the solidification rate. The purpose of this section is to assess practical operating techniques such as manipulating enclosure depth and insulation. Also included in this section is a discussion of how external temperature gradients influence the interface shape and the resulting effect on the impurity profile.

5.2.1 Enclosure Depth

Although regional convection currents can be controlled by the thermal conditions surrounding the zone, geometry of the enclosure is vital for the driving force of natural convection throughout the melt. If the fluid flow is simple throughout the bulk of the melt, it is likely that the magnitude of thermal oscillations at the freezing interface is smaller. For example, the dimensions of the enclosure have more influence on the bulk convection than temperature gradients. Accordingly, characteristic length in the Grashof number is cubed while temperature difference is to the first power (see Table 2-1). In section 4.2.2 and 4.3.3, it was shown that the complexity of bulk fluid flow decreases with enclosure size.

As discussed in Section 3.2.1, ingot depth was manipulated to vary the enclosure size. The alternative would be to purchase boats with varying cross section or size. As shown in Figure 5-2, shallow and wide (A) or tall and thin cross (B) sections could be

fabricated. Rectangular or triangular cross sections are not considered because of the possibility of stress concentrations at the corners.

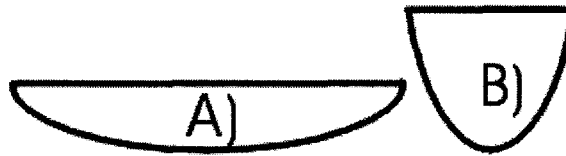


Figure 5-2: Varying boat cross section shape

To maximize strength and to provide fast heat transfer from the heaters, the boat cross section should match the tube shape so that contact surface area between the boat and tube is maximized. For example, a shallow and wide boat as shown in Figure 5-2 (A) would require a horizontally oblong tube. Additional support equipment such as aluminum end caps and heaters must also be fabricated to match the tube shape. The advantage of changing the boat cross section is that the load can be increased, thereby maximizing the capacity of the equipment while maintaining a low ingot depth.

In addition to inhibiting the overall magnitude of convection, reducing ingot depth influences the size and number of convection cells present [68]. As discussed in Section 4.3.2 using the wavelet spectrum diagrams, large convection cells are not as easily defined at lower depths. With the disruption of large convection cells, fluid movement from one region of the melt is transferred to other regions with difficulty in the presence of more internal friction. For example, momentum is not as easily transferred from the active region at the bottom of the zone to the freezing interface if several small convection cells are involved. In this situation, the freezing interface would be less sensitive to convection rates in other regions of the melt.

Reducing the load will likely increase the segregation rate and decrease the total number of passes to achieve target purity levels. However, a smaller load would decrease the overall yield from each batch. An essential optimization criterion would be to manipulate the volume of charge to produce the most material per unit of processing time. This is discussed further in the future work (Section 6.2). Another option would be to extend the ingot length. However, this is limited by the available space for zone refining equipment. In addition, the quartz tube is supported at either end, and must be strong enough to support the weight of the ingot. A length of a zone refining unit may be limited by the strength of the quartz.

5.2.2 External Temperature Gradients

As mentioned previously, external temperature gradients are important for localized control of convection currents and the shape of the zone. The most effective way to influence external temperature gradients is the appropriate placement of insulation around the heaters. In present equipment, insulation is added to the front of the heater to save energy costs. However, as found with Test 5 in Section 4.3.3, this is not the most desirable approach. Due to a change in the external temperature gradients, the freezing interface migrates closer to the heater. The result is an increase in local temperature gradients, and more complex fluid movement develops. Ultimately, separation efficiency is reduced. A more suitable approach would be to add insulation to the back of the heater thereby distancing the freezing interface.

Benefits to adding insulation include a reduction in temperature gradients and a decrease in energy consumption. However, the machinery may be more difficult to

operate. For example, it may be harder to maintain a consistent zone under varying environmental conditions such as changing room temperature and air currents. Controlling the zone size under varying conditions may be enhanced by applying a process control system to manage the temperature of the heaters as discussed further in Section 6.2.

5.2.3 Interface Shape

While decreasing convection is suitable for preventing thermal oscillations, a separate issue arises when considering the assumption of perfect stirring throughout the zone. Although the limiting transport phenomenon for segregation was determined to be thermal oscillations at the freezing interface, it is important that there are no stagnant regions within the melt. If sufficient fluid flow is not maintained, the impurity concentration would not be homogenized throughout the melt.

As shown in Section 2.5.1, the interface shape is likely to play a role in the shape of the convection cells. In the case of a completely vertical interface, it is probable that a small stagnant region would develop at the intersection between the interface and the boat. This would lead to an inconsistent segregation rate over the area of the interface and would likely impede the overall separation process. For example, interface shape has been found to result in radial segregation during Czochralski crystal growth [99] due to a variation in the boundary layer thickness across the interface. In this respect, a smooth, slight curve in the interface is beneficial to avoid stagnant regions.

In terms of the impurity profile after processing is complete, excessive freezing interface slope may be detrimental. For example, the bottom and top would freeze at different points in time. Since the concentration is expected to change along the length of the bar and is a function of time, there would be a concentration gradient between the top and bottom of the bar. To compensate for this, assays should be taken from the bottom of the ingot where the concentration is most likely to be highest (first to freeze). This will prevent errors in characterizing the bar and impurities entering the next process stream unintentionally. At low depths, the problem of a steep slope is not as critical. Even in the case of a severely sloped interface, it will not span a large axial distance because of the low depth. Given the analogy of a staircase, if the rise is not high, even at a low inclination angle, the run will not span a great distance.

To satisfy both mechanisms mentioned in this section, a shallow charge is beneficial. Low depth would allow for a curved interface to inhibit stagnant regions at the freezing interface without causing a severe vertical concentration gradient. In order to control the shape of the molten zones, insulation can be added to the top and bottom of the tube in different combinations to achieve the proper slope of freezing interface. For example, to decrease the slope of the interface, it would be better to add insulation to the bottom of the tube while leaving the top of the tube exposed.

5.3 Application to Different Materials

As described in Section 1.1, zone refining is important for the purification of various semiconductors including germanium, indium antimonide, and antimony. Although similar equipment is used, these metals have different physical properties compared

to lead and react differently under similar thermal conditions. The purpose of this section is to identify the differences in their physical properties which would affect their zone refining characteristics. Of the many physical properties, the most important variables are the melting temperature, and those encompassed in the Prandtl and Stefan numbers.

5.3.1 Stefan Number

The rate of a transformation between phases is dependent on the Stefan number. As described by Equation 5-1, it is a relationship between the heat of formation, the heat capacity of the metal, and the amount of superheating or supercooling. Assuming similar temperature gradients and temperature oscillations, the coefficient $\Delta H_f/C_L$ can be used to compare the melting and freezing rates of different metals.

$$Sf = \frac{\Delta H_f}{C_L \cdot (T_{melt} - T_L)} \quad (5-1)$$

Where C_L (J/g·K) is the heat capacity of the liquid phase, and ΔH_f (J/g) is the heat of transformation.

The correlation provided in Equation 5-2 was derived by Crochet et al. [79] to describe the amplitude of interface velocity oscillations as a function of the Stefan number. The empirical coefficient 0.038 is dependent on ratio of the heat capacities as well as the ratio of heat conductivities between the liquid and solid (set to 1 in this example). According to this correlation, the smaller the Stefan number, the higher the amplitude of interface oscillations.

$$Amplitude = \frac{0.038 \cdot (enclosure \ depth)}{Sf} \quad (5-2)$$

Figure 5-3 demonstrates the Stefan number coefficient for various metals. Assuming a similar oscillatory flow in the molten zone, the interface velocity would oscillate most at low Stefan numbers. For example, germanium would be least susceptible to oscillatory flow while indium is most susceptible. In terms of the separation efficiency, the temperature oscillations in the fluid would be more detrimental to separation for materials with a low Stefan number.

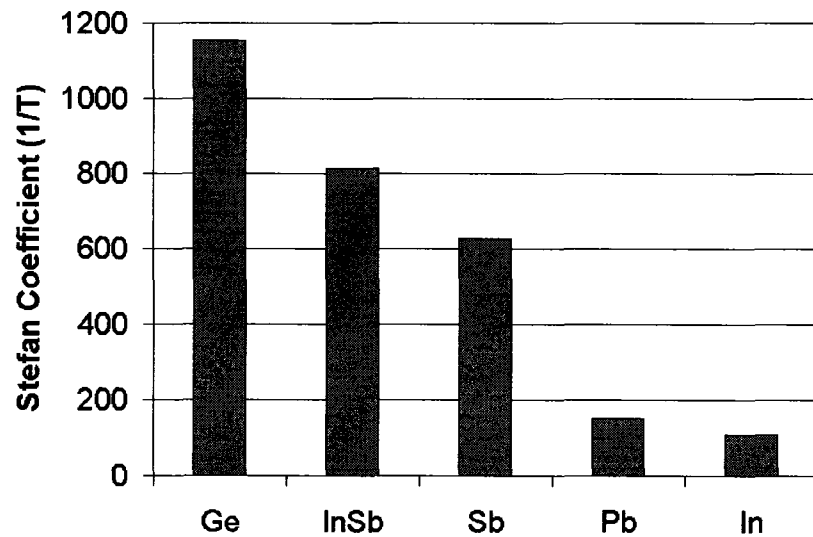


Figure 5-3: Stefan coefficient ($\Delta H_f/C_p$) for various liquid metals at their melting temperature [44][43][100][101]

In Section 5.1.1, Figure 5-1, the qualitative relationship between separation efficiency and the fluid flow regime was predicted. As the convection regime advances through laminar, oscillatory, and finally turbulent flow, it is expected that the separation efficiency improves, worsens, and then improves again respectively. Using the Stefan number, the influence of oscillatory flow on the zone refining characteristics of various materials can be compared. For example, the relative shape of the separation efficiency versus flow regime diagram can be approximated. As shown in

Figure 5-4, it is expected that the smaller the Stefan number, the more detrimental oscillatory flow is to separation efficiency.

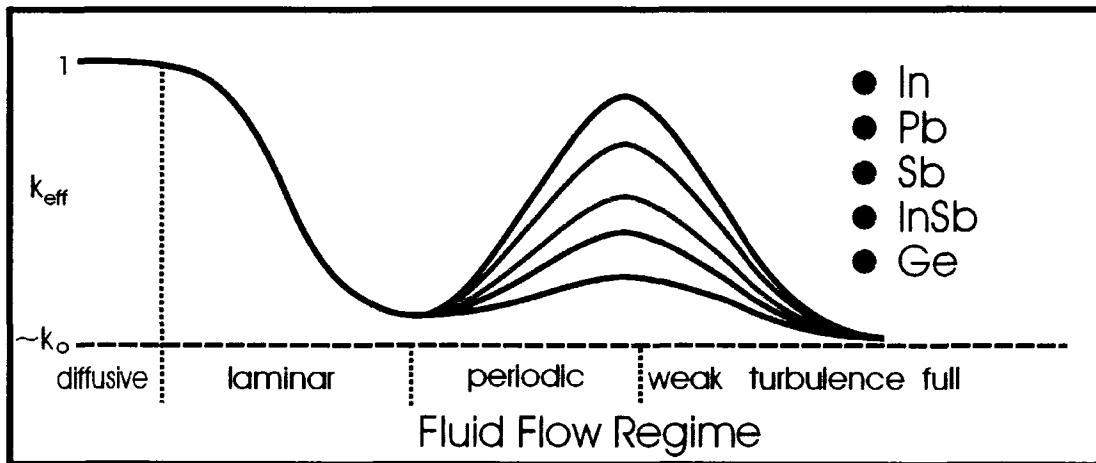


Figure 5-4: Approximate separation efficiency versus fluid flow regime for various metals

Assuming a similar convection regime, Figure 5-4 indicates that indium should be the most difficult to zone refine, followed by lead, antimony, indium antimonide, and finally germanium. This relationship is supported in literature. For example, in Czochralski growth experiments of germanium, k_{eff} is not altered by more than 5% by oscillations [102] suggesting that it should be relatively easy to zone refine. In addition, empirical evidence formulated from practical experience at Firebird Technologies shows that germanium is extremely responsive to zone refining compared to indium antimonide or antimony [103]. On the other hand, indium is very difficult to zone refine [103]. In addition, the experiments outlined in this thesis show that lead is very susceptible to oscillations at the freezing interface and is relatively difficult to zone refine.

A practical application of this is the preparation of indium antimonide, where it would be more effective to zone refine the compound compared to refining its elemental components indium and antimony separately. Also, reducing the convective complexity of fluid flow would have the greatest impact on the separation efficiency of indium, followed by lead, antimony, indium antimonide, and lastly germanium. However, as seen in Section 5.3.2, reducing the fluid flow complexity is much more difficult for some materials than others.

5.3.2 Estimations of Fluid Flow Regime

The Prandtl number, as mentioned in Section 2.3.2, is a measure of how easily convection is developed in the fluid. Metals with low Prandtl numbers typically experience oscillatory flow at lower Grashof numbers (low critical Grashof number). This is important in relating metals to one another because metals with lower Prandtl numbers will exhibit more complex convection under similar temperature gradients. Figure 5-5 displays the Prandtl number for various materials. Accordingly, indium antimonide resists natural convection currents easily while Germanium will exhibit the most advanced convective complexity.

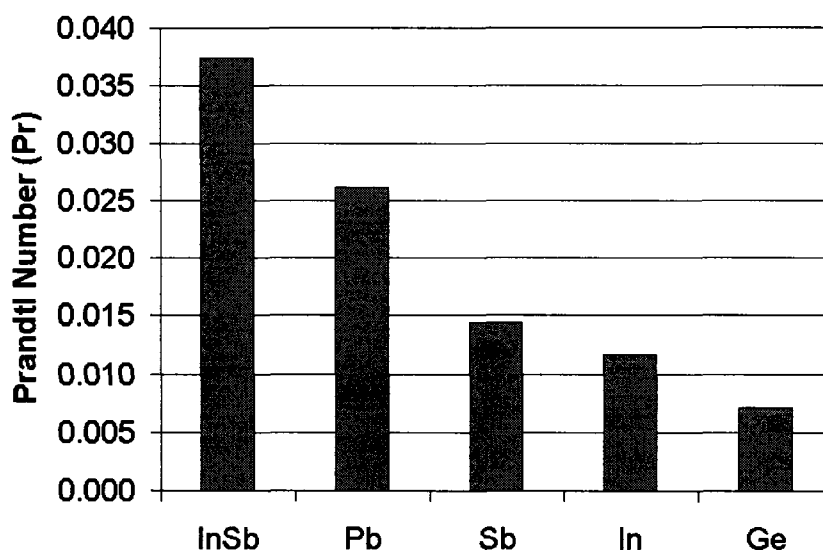


Figure 5-5: Prandtl numbers of various liquid metals at their respective melting points [100][44][43][101]

As mentioned in Section 2.3.1, temperature gradients in the molten zone result in buoyant forces which drive convection. Although it is difficult to estimate temperature gradients without experimental data or a thermal model, the melting temperature is a good indication. For example, metals with a higher melting temperature experience a larger temperature difference between the molten pool and the ambient temperature surrounding the ingot. In this situation it is likely that temperature gradients within the molten zone are larger. Figure 5-6 shows the melting temperature for various semiconductor metals. In summary, germanium is expected to have the highest temperature gradients followed by indium antimonide, antimony, lead, and indium. Other factors that could influence temperature gradients include the heat conductivity of the solid ingot, emissivity, heat capacity, or viscosity, although these properties are not discussed here.

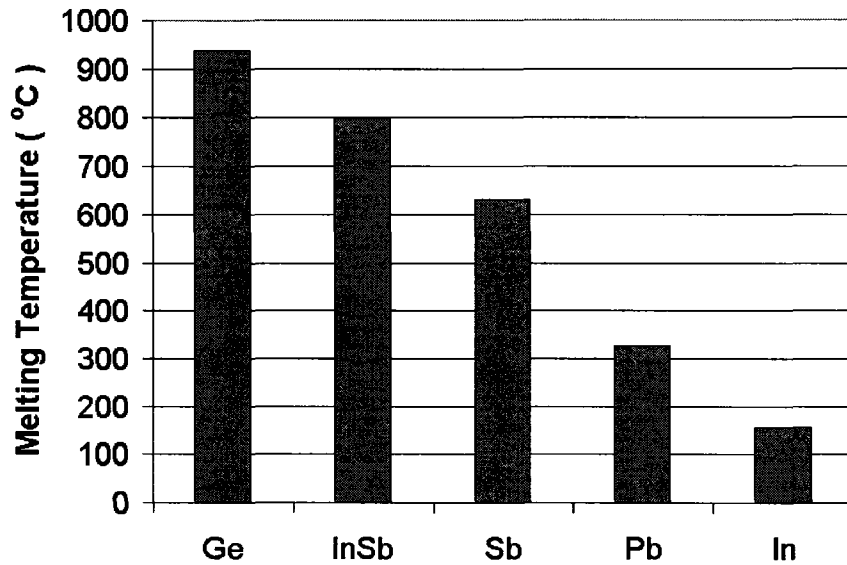


Figure 5-6: Melting temperature for various metals [100][44][43][101]

Table 5-1: Summary temperature gradient and critical Grashof number ranking

Rank	Expected $\frac{dT}{dx}$	Gr_c (lowest to highest)
1	Ge	Ge
2	InSb	In
3	Sb	Sb
4	Pb	Pb
5	In	InSb

Table 5-1 is a summary of the temperature gradient and critical Grashof number ranking between metals that are analyzed in this section. Accordingly, metals such as antimony and germanium both have higher expected temperature gradients in combination with lower critical Grashof numbers. It can be concluded that these metals will experience higher fluid flow complexity than lead. It is not known whether fluid flow will advance into turbulent regimes in these materials under normal zone refining boundary conditions. The convection complexity of indium and

indium antimonide is inconclusive because melting temperature and the critical Grashof number are ranked oppositely compared to lead.

In terms of opportunity to reduce convection complexity, indium antimonide is very promising. Since temperature gradients are expected to be high, there is much opportunity to reduce them by manipulating operating conditions such as the insulation placement and heater power. In addition, the critical Grashof number is high, suggesting that fluid flow will be simple under low temperature gradients. On the other hand, it is not likely that indium can be improved further since the temperature gradients are already low and the critical Grashof number is small.

Chapter 6 Conclusions and Future work

6.1 Conclusions

The purpose of this project was to investigate the fundamental mechanisms behind zone refining. An analysis of the transport phenomena revealed that convection is important for both the rate of impurity movement and the stability of the advancing freezing interface. In order to understand the dominant transport phenomena and correlate convection characteristics to separation efficiency, a series of experiments were done to characterize the convection and calculate the associated separation efficiency. Using this knowledge, insight for controlling operating conditions was developed for improving separation efficiency of the process.

Experiments were designed in order to gauge the influence of operating conditions on the convection rates within the molten zone. The separation efficiency was then measured and correlated to convection characteristics. For a series of boundary conditions, temperature probes were placed in direct contact with the melt to measure the temperature field of the molten zone. Average temperatures were used to give information about the driving force of convection. Local temperature fluctuations were used to characterize the complexity and rate of flow. After characterizing the fluid flow using thermal measurements, an ingot was zone refined and the concentration profiles were measured using glow discharge mass spectrometry for the different test conditions. The concentration profile was then fitted to a mass balance model to calculate separation efficiency.

The results of this project indicated that the bulk convection rate can be reduced by decreasing the ingot depth and external temperature gradients. All tests exhibited quasi-oscillatory convection. In addition, it was demonstrated that local convection currents within the zone can vary according to position within the zone. By using different insulation patterns, the distance between the freezing interface and the heater can be increased, thereby decreasing local convection complexity at the interface. The most efficient segregation occurred when the complexity of convection was lowest at the freezing interface, indicative of a slow, stable interface velocity.

From the results of this project it was found that lead metal is sensitive to oscillations in the temperature field. A reduction in these oscillations can improve the zone refining process by enhancing the segregation efficiency. Control measures for reducing process time and product quality include reducing ingot depth and manipulating insulation placement. However, an analysis of physical properties revealed that zone refining characteristics can vary significantly between different metals. The Prandtl number, Stefan number, and melting temperature are used to compare physical properties that influence the fluid movement rate and interface oscillations. For example, metals with low Prandtl number typically exhibit oscillatory flow at lower Grashof numbers. Metals with a high melting temperature are more likely to experience high temperature gradients and therefore higher Grashof numbers. Metals with a low Stefan number have a more unstable liquid/solid interface in the presence of temperature fluctuations. Using this analysis, different

metals were rated for their relative ease of zone refining, from best to worse being: germanium, indium antimonide, antimony, lead, and indium.

6.2 Future Work

With improving the zone refining technique in mind, some valuable concepts can be distilled from the work in this thesis. It was established that high complexity of oscillations adjacent to the freezing interface can inhibit separation efficiency. This relationship is important for identifying the need for controlling convection using operating conditions. For example, to reduce convection complexity, depth of the ingot and the location of insulation can be manipulated. However, it is also evident that more work is necessary to verify the practical considerations of these techniques, and optimize these variables for industrial use. In this chapter, subjects such as optimizing heater travel rate, computer process control of heater temperature, analysis of striations, magnetic fields, and impurity interactions are addressed. The possibility of applying concepts learned in this study to Czochralski crystal growth due to some common phenomena in zone refining is also discussed.

With the goal of reducing overall zone refining process time and improving overall product quality, insulation configuration, zone depth, and number of passes must be optimized. For example, adding insulation to the rear of the heater is assumed to reduce convection complexity at the freezing interface; however this specific configuration has never been tested in practice. Further experimentation is required in order to verify the effectiveness of this approach and affirm its practicality. It is possible that insulation extending behind the heaters may increase the difficulty of

maintaining consistent zone size in the presence of perturbations in the room temperature and humidity. In addition, if the convection characteristics are modified by reducing the ingot depth, the yield per batch would be reduced. Assuming a reduction in batch load would enhance separation rate and reduce the total number of passes required, an optimization scheme would be valuable in maximizing the throughput per unit of processing time.

An analysis of the fundamental mechanisms behind zone refining described in Chapter 2 demonstrated that the zone travel rate is an essential variable for mass transport. While there has been no attempt in this thesis to correlate segregation rate to the macroscopic interface velocity, there is potential in this subject. It is possible that segregation rate may be enhanced greatly by reducing the heater travel rate. Since heater travel rate is directly proportional to the time required for a given number of zone passes, an optimization scheme is required to maximize the throughput per unit of time. This can be accomplished via experimental or modeling work, depending on the available resources and specific goals. Out of many possible combinations, one approach may involve fast initial passes to remove most of the easily removed elements, and then several slow passes to remove more immobile elements.

Throughout all experiments, the power to the heaters was controlled manually by visually observing the size of the molten zones. It was found that, at different regions of the bar, the power requirement changed somewhat. For example, more power was required at the beginning compared to the middle of the ingot. In addition, depending

on the insulation configuration and depth of zone, it was more difficult to sustain consistent zone sizes in some experiments. In order to enhance consistency of operating conditions and automate the process, one approach would be to apply a PID controller with thermocouple feedback embedded in the heater to maintain constant zone temperature [13]. This approach will likely reduce the number of mistakes attributed to human error, maximize the consistency between tests, and decrease the manpower required to operate the equipment. Another option is to remove the mechanical movement of the heater assembly entirely by placing an array of stationary heaters around the ingot. By manipulating them via PID controller, it would be possible to create a waveform in the heater power down the length of the ingot. This has benefits in that it would eliminate the discontinuity in heater movement due to retraction at the end of the heater travel distance. In addition, the zone movement rate, zone temperature, and adjacent temperature gradients could be controlled precisely.

One of the most important aspects of this study was the characterization of convection currents using a thermal analysis of the zone. While temperature oscillations are intrinsic evidence of convection currents, oscillations in the interface velocity can be characterized by striations on the surface of the ingot. In the absence of scale on the surfaces of the ingot, these striations can typically be observed visually under a microscope. This approach is helpful in that it is non-intrusive and does not pose any threat of contamination by immersed thermocouples. In addition, the presence of striation may be used as a quick qualitative indication of the presence

or extent of oscillations as a comparison between tests. For example, oscillations with larger amplitude will exhibit striations that are further apart.

Although not addressed in this project, magnetic fields have been studied extensively as an effective way to reduce striations and decrease axial segregation in Czochralski crystal growth [40] [15] [96] [103]. It is possible that this technique could be applied to horizontal Bridgman zone refining to enhance macro segregation.

As mentioned in Section 1.2, the solubility of impurities can vary according to interactions with other impurity elements. It is possible that the overall separation efficiency could be enhanced by adding impurity elements that would enhance the movement of troublesome impurities. A thorough thermodynamic investigation of the impurity systems could reveal the potential of this approach.

Zone refining is similar to Czochralski crystal growth in that they both involve a solid/liquid interface, segregation, and are highly dependant convection currents within the liquid metal. For example, melt oscillations due to turbulence has been attributed to poor crystal quality in Czochralski crystal growth [89]. It is therefore possible that some concepts learned in this study can be applied to both applications. Although there are different thermal conditions in Czochralski crystal growth, variables such as melt geometry, insulation, baffles [58], and heat reflectors [89] may be applied to reduce oscillations in the melt. Generally, for single crystal growth operations, striations are detrimental because an inhomogeneous impurity profile

causes a greater risk for defects during single crystal growth [105]. For single crystal growth, oscillations should be avoided so that higher quality crystals can be produced. However, zone refining is an intermediate step in single crystal growth, and since the material will be melted in successive processing steps, microscopic striations are not directly harmful. The most pertinent issue is that these oscillations may be detrimental to the overall macro segregation.

References

- [1] W.G. Pfann, "Principles of Zone Refining", *Transactions AIME*, v.194, **1952**, pages 747-753.
- [2] T. C. Harman, "Effect of Zone-Refining Variables on the Segregation of Impurities in Indium-Antimonide" *Journal of the Electrochemical Society*, v. 103, **1956**, pages 128-132.
- [3] H. Y. Lee, J.K. Oh, D. H. Lee, "Purification of Tin by Zone Refining with Development of a New Model", *Metallurgical Transactions B*, v. 21B, **1990**, pages 455-461.
- [4] T. Gebre, K. Bhat, A. Batra, R. Lal, M. Aggarwal, "Purification of Organic Nonlinear Optical Materials for Bulk Crystal Growth from Melt", *Proceedings of SPIE - The International Society for Optical Engineering: Crystal Materials for Nonlinear Optical Devices and Microgravity Science*, v. 4813, **2002**, pages 36-42.
- [5] A. R. Murray, J. Baldrey, J. Mullin, O. Jones, "A Systematic Study of Zone Refining of Single Crystal Indium Antimonide", *Journal of Materials Science*, v. 1, **1966**, pages 14-28.
- [6] Lab Manual on Crystal Growth, Academic Press, Budapest, 1972.
- [7] H. L. Goering, *Compound Semiconductors*, V. 1, Reinhold Publishing, New York, **1962**, page 96.
- [8] O. Nesher, P.C. Klipstein, "High-Performance IR Detectors at SCD Present and Future", *Proceedings of SPIE - The International Society for Optical Engineering: Infrared Photoelectronics*, v. 5957, **2005**, pages 1-12.
- [9] B.D. Schwartz, J. Askinazi, R.R. Poole, "Highly Transmissive, Ion Implanted Germanium Windows", *Proceedings of SPIE - The International Society for Optical Engineering: Window and Dome Technologies and Materials VII*, v. 4375, **2001**, pages 90-95.
- [10] T. Utsunomiya, Y. Hoshino, "Horizontal Resistance-Heated Zone Refiner for Chemicals and Metals with Melting Point Below 600 Degrees C", *Report of the Research Laboratory of Engineering Materials*, Tokyo Institute of Technology, No. 7, 1982.

- [11] U. Merten, K.D. Vos, A.P. Hatcher, "Distribution Coefficient Studies in Indium Antimonide", *J. Phys. Chem. Solids*, v. 30, **1969**, pages 627-64.
- [12] C.W. Lan, M.C. Liang, C.H. Chian, "Suppressing Three-Dimensional Unsteady Flow in Vertical Zone-Melting by Steady Ampoule Rotation", *Journal of Crystal Growth*, v. 213, **2000**, pages 395-407.
- [13] I. Ohno, N. Iwasaki, T. Yoneyama, "Horizontal Zone-Melting of Indium Antimonide in Vacuum. I. Basic Technique", *Japanese Journal of applied Physics*, v.18, **1979**, pages 285-293.
- [14] R.M. Felder, R.W. Rousseau, *Elementary Principles of Chemical Processes 3rd ed.*, John Wiley and Sons, New York, **2000**, page 237.
- [15] D.T.J. Hurle, *Handbook of Crystal Growth Volume: Bulk Crystal Growth*, North Holland, Amsterdam, **1994**.
- [16] W.G. Pfann, "Zone Melting, 2nd Edition", Wiley, New York, 1966.
- [17] V. N. Vigdorovich, A.E. Vol'p'yan, G.I. Shuleshko, "Selection of Optimum Zone Movement Rate when Using Zone Recrystallization", *Tsvetnye Metally*, v. 63 no. 7, **1968**, pages 87-89.
- [18] W.D. Lawson, S. Nielsen, *New Chemical Engineering Separation Techniques*, Interscience Publishers, **1962**, New York-London, page 202-205.
- [19] H. Reiss, C.S. Fuller, F.J. Morin, "Chemical Interactions Among Defects in Germanium and Silicon", *The Bell System Technical Journal*, v.35 no 3, **1956**, page 535.
- [20] L. F. Kozin, A.G. Morachevskii, "Ultrapurification of Lead by Zone Melting Methods. II. Technological Processes of Zone Refining", *High-Purity Substances*, v. 6, no 5-6, 1992, pages 687-698.
- [21] K. Lehovc, A. Slobodskoy, "Impurity Content of Germanium Crystallized from the Liquid Ternary Alloy Ge-In-Sb", *Journal of the Electrochemical Society*, v.111 No.1, **1964**, pages 65-73.
- [22] U. Merten, A.P. Hatcher, "The Distribution of Zinc Between Solid InSb and InSb Melts", *J. Phys. Chem. Solids*, v. 23, **1962**, pages 533-539.
- [23] L.W. Davies, "Determination of the Limiting Segregation of Gallium in Zone-Refined Germanium", *Transactions of AIME*, v.212, **1958**, pages 799-801.

- [24] A. Vol'p'yan, V. Ivleva, N. Pepik, V. Selyanina, "Zone Refining of Tellurium Doped InSb", *Izvestiya Akademii Nauk SSSR*, v. 7 no.7, **1971**, pages 1257-1258.
- [25] N.W. Lord, "Analysis of Molten-Zone Refining", *Transactions AIME*, November, **1953**, pages 1531-1533.
- [26] H. Reiss, "Mathematical Methods for Zone-Melting Processes", *Transactions of AIME*, September, **1954**, pages 1053-1059.
- [27] J.A. Spim, M.J.S. Bernadou, A. Garcia, "Numerical Modeling and Optimization of Zone Refining", *J. of Alloys and Compounds*, v. 298, **2000**, pages 299-305.
- [28] E.Scheil, "Bermerkunzen zur Schichtkristallbildung", *Zeitschrift für Metallkunde*, v34, **1942**, page 70.
- [29] W. Jie, R. Zhang, "The Modeling of the Solute Redistribution During Solidification of Ternary Alloys", *Materials Science Forum*, v. 437-438, **2003**, pages 375-378.
- [30] H. Yeh, C. Ho "Simulation of Multipass Zone-Refining Processes", *Journal of the Chinese Institute of Chemical Engineers*, v. 27, **1996**, pages 57-63.
- [31] L.W. Davies, "The Ultimate Distribution of Impurity in the Zone-Melting Process", *Philosophy Magazine*, v.3, **1958**, pages 159-162.
- [32] L. Burris, C. Sotckman, I. Dillon, "Contribution to Mathematics of Zone Melting", *Transactions AIME*, v.203, **1955**, pages 1017-1020.
- [33] H. Yeh, W. Yeh, "The Improvement of Separation on Zone Refining Processes with Zone Length Varied Along the Ingot", *Separation Science and Technology*, v. 14, **1979**, pages 795-803.
- [34] C. Ho, H. Yeh, T. Yeh, "Numerical Analysis on Optimal Zone lengths for Each Pass in Multipass Zone-Refining Processes", *The Canadian Journal of Chemical Engineering*, v. 76, **1998**, pages 113-119.
- [35] C. Ho, H. Yeh, T. Yeh, "Optimal zone length in multi-pass zone-refining processes", *Separations Technology*, v. 6, **1996**, pages 227-233.
- [36] C. Ho, H. Yeh, T. Yeh, "The Optimal Variation of Zone Lengths in Multipass Zone Refining Processes", *Separation and Purification Technology*, v. 15, **1999**, pages 69-78.

- [37] G.H. Rodway, J.D. Hunt, "Optimizing Zone Refining", *Journal of Crystal Growth*, v. 97, **1989**, pages 680-688
- [38] C. Ho, H. Yeh, T. Yeh, "Multipass Zone Refining with Specified Ingot Volume of Frustum with Sine-Function Profile", *Separation and Purification Technology*, v.11, **1997**, pages 57-63 .
- [39] M. Pimputkar, S. Ostrach, "Convective Effects in Crystals Grown from Melt", *Journal of Crystal Growth*, v.55, **1981**, pages 614-646.
- [40] R.A. Brown, "Theory of Transport Processes in Single Crystal Growth from the Melt Part 1", *AIChE Journal*, v. 34 no. 6, **1988**, pages 881-911.
- [41] R.B. Bird, W.E. Steward, E.N. Lightfoot, *Transport Phenomena 2nd ed.*, John Wiley and Sons, New York, **2002**.
- [42] R. Kuhl, H. Wilke, "Buoyant Convection of Low Prandtl Number Melts in Horizontal Boat Configuration", *Acta Astronautica*, v.29 no.1, **1993**, pages 51-60.
- [43] F.P. Incropera, D.P. DeWitt, *Introduction to Heat Transfer 3rd ed.*, Wiley, New York, **1996**.
- [44] E.A. Brandes, G.B. Brook, "Smithells Metals Reference Book 7th edition", Butterworth Heinemann, Oxford, 1992.
- [45] http://strategis.ic.gc.ca/epic/internet/inmc-mc.nsf/en/h_lm03166e.html, accessed June 5, 2006.
- [46] K.M. Kim, A.F. Witt, H.C. Gatos, "Crystal Growth from the Melt Under Destabilizing Thermal Gradients", *Journal of the Electrochemical Society: Solid-State science and technology*, v. 119 no 9, **1972**, pages 1218-1226.
- [47] A.G. Ostrogorsky, "A Model of Effective Segregation Coefficient, Accounting for Convection in the Solute Layer at the Growth Interface", *Journal of crystal growth*, v.121,**1992**, pages 587-598.
- [48] C. Marin, A.G. Ostrogorsky, "Control of Convection During Directional Solidification in Terrestrial and Low Gravity", *SPIE Conference on Materials Research in Low Gravity II*, v.3792, **1999**, pages 112-123.
- [49] W.A. Tiller, K.A. Jackson, J.W. Rutter, B.Chalmers, "The Redistribution of Solute Atoms during the Solidification of Metals", *Acta Metallurgica*, v.1, **1953**, pages 428-437.

- [50] C. Wagner, "Theoretical Analysis of Diffusion of Solutes During The Solidification of Alloys", *Journal of Metals*, v. 200 no.2, **1954**, pages 154-160.
- [51] J.A. Burton, R.C. Prim, W.P.Slichter, "The Distribution of Solute in Crystals Grown from the Melt. Part I. Theoretical", *The Journal of Chemical Physics*, v. 21, **1953**, pages 1987-1991.
- [52] H. Schlichting, *Boundary Layer Theory 4th ed.*, McGraw-Hill Book Co. Inc., New York, **1960**.
- [53] W.R. Wilcox, "Validity of the Stagnant Film Approximation for Mass Transfer in Crystal Growth and Dissolution", *Materials Research Bulletin*, v. 4, **1969**, pages 265-274.
- [54] J.P. Garandet, J.J. Favier, D.Camel, "Solutial Boundary Layer Concept and Scaling Analysis: Two Keys to Segregation Phenomena in Melt Crystal Growth", *Journal of Crystal Growth*, v. 130, **1993**, pages 113-122.
- [55] L.O. Wilson, "A New Look at the Burton, Prim, and Slichter Model of Segregation During Crystal Growth from the Melt", *Journal of Crystal Growth*, v. 44 no. 4, **1978**, pages 371-512.
- [56] H.J. Sung, Y.J. Jung, "Prediction of Transient Oscillating Flow in Czochralski Convection", *International Journal of Heat and Mass Transfer*, v.38 No.9, **1995**, pages 1627-1636.
- [57] T. Jung, G. Muller, "Effective Segregation Coefficients: A Comparison of Axial Solute Distributions Predicted by Analytical Boundary Layer Models and Numerical Calculations", *Journal of Crystal Growth*, v.165, **1996**, pages 463-470.
- [58] A.G. Ostrogorsky, Z. Dragojlovic, "Heat and Mass Transfer in Solidification by the Submerged Heater Method", *Transport Phenomena in Solidification ASME*, v. 182, **1994**, pages 255-263.
- [59] D. Thevenard, A. Rouzaud, J. Comera, J.J. Favier, "Influence of Convective Thermal Oscillations on a Solidification Interface in Bridgman Growth", *Journal of Crystal Growth*, v. 108, **1991**, pages 572-582.
- [60] W.W. Mullins, R.F. Sekerka, "Stability of a Planar Interface During Solidification of a Dilute Binary Alloy", *Journal of Applied Physics*, v.35 no.2, **1964**, pages 444-451.

- [61] W.M. Yim, "Transverse Striations in Bi-Sb Alloy Single Crystals", *Transactions of the Metallurgical Society of AIME*, v.236, **1966**, pages 474-482.
- [62] D.J. Carlson, A.F. Witt, "Microsegregation in Conventional Si-Doped LEC GaAs", *Journal of Crystal Growth*, v. 108, **1991**, pages 508-518.
- [63] T. Carlberg, "Some Aspects on the Formation of Striations During Crystal Growth From the Melt", *Journal of Crystal Growth*, v.85, **1987**, pages 32-39.
- [64] K.M. Kim, A.F. Witt, "Quantitative Analysis of the Thermal Effects of Destabilizing Vertical Thermal Gradients on Crystal Growth and Segregation: Ga-Doped Ge", *Journal of Crystal Growth*, v.125 no3., **1978**, pages 475-480.
- [65] D.E.Holms, H.C.Gatos, "Convective Interface and "Effective" Diffusion-Controlled Segregation during Direction Solidification under Stabilizing Vertical Thermal Gradients; Ge", *Journal of the Electrochemical Society*, v.128 no.2, **1981**, pages 429-437.
- [66] L.O. Wilson, "The Effect of Fluctuating Growth Rates on Segregation in Crystals Grown from the Melt: II Backmelting", *Journal of Crystal Growth*, v.48, **1980**, page 451-458.
- [67] A.M.J.G. Van Run, "Computation of Striated Impurity Distributions in Melt-Grown Crystals, Taking Account of Periodic Remelt", *Journal of Crystal Growth*, v. 47, **1979**, pages 680-692.
- [68] E. Bucchignani, D. Mansutti, "Rayleigh-Marangoni Horizontal Convection of Low Prandtl Number Fluids", *Physics of Fluids*, v.16 no 9, **2004**, pages 3269-3280.
- [69] H. Okamoto, *Phase Diagrams of Dilute Binary Alloys*, ASM International, Materials Park, 2002.
- [70] D.T.J. Hurle, "Convective Transport in Melt Growth Systems", *Journal of Crystal Growth*, v. 65, **1983**, pages 124-132.
- [71] G.S. Roussopoulos, "Simulation of Zone Refining for a Semiconducting Material: Indium Antimonide", *MSc Thesis*, Cranfield University School of Mechanical Engineering, 2003.
- [72] M.C. Hung, C.D. Andereck, "Subharmonic transitions in convection in a moderately shallow cavity", *Numerical Simulation of Oscillatory Convection in Low-Pr Fluids*, v. 27, **1990**, pages 338-343.

- [73] D.T.J. Hurle, E. Jakeman, C.P. Johnson, "Convective Temperature Oscillations in Molten Gallium", *Journal of Fluid Mechanics*, v.64, 1974, pages 565-576.
- [74] D. Henry, M. Buffat, "Two-and Three-Dimensional Numerical Simulations of the Transition to Oscillatory Convection in Low-Prandtl-Number Fluids", v. 374, 1998, pages 145-171.
- [75] C.W. Lan, M.K. Chen, M.C. Liang, "Bifurcation and Stability Analyses of Horizontal Bridgman Crystal Growth of a Low Prandtl Number Material", *Journal of Crystal Growth*, v. 187, 1998, pages 303-313.
- [76] E. Bucchignani, "Horizontal Thermal Convection in a Shallow Cavity: Oscillatory Regimes and Transition to Chaos", *International Journal of Numerical Methods for Heat and Fluid Flow*, v.10, 2000, pages 179-195.
- [77] J.M. Pratte, J.E. Hart, "Endwall Driven, Low Prandtl Number Convection in a Shallow Rectangular Cavity", *Journal of Crystal Growth*, v.102, 1990, pages 54-68.
- [78] J. H. Wang, D. H. Kim, "Numerical Analysis of Melt/Solid Interface Shape in Zone Melting Recrystallization Process", *Journal of Crystal Growth*, v. 173, 1997, pages 201-209.
- [79] M.J. Crochet, F.T. Geyling, J.J Van Schaftingen, "Numerical Simulation of the Horizontal Bridgman Growth of a Gallium Arsenide Crystal", *Journal of Crystal Growth*, v.65, 1983, pages 166-172.
- [80] K.H. Winters, "Oscillatory Convection in Liquid Metals in a Horizontal Temperature Gradient", *International Journal for Numerical Methods in Engineering*, v. 25, 1988, pages 401-414.
- [81] J.R. Carruthers, "Thermal Convection in Horizontal Crystal Growth", *Journal of Crystal Growth*, v.2, 1968, pages 1-8.
- [82] T. Iida, R.I.L. Guthrie, *The Physical Properties of Liquid Metals*, Clarendon Press, Oxford, 1988.
- [83] G. Muller, "Convective instabilities in melt growth configurations", *Journal of Crystal Growth*, v.128, 1993, pages 26-36.

- [84] A.K. Tangirala, M.A.A.S. Choudhury, H. Liu, S. Imtiaz, N. Thornhill, H. Jiang, S.L. Shah, *Data Visualization and Analysis Tool for Matlab*, Computer Process Control Group, University of Alberta, Edmonton, 2005.
- [85] A.E. Gill, "A Theory of Thermal Oscillations in Liquid Metals", *Journal of Fluid Mechanics*, v.64, 1974, pages 577-588.
- [86] J.R. Abernathy, F. Rosenberger, "Time-Dependent Convective Instabilities in a Closed Vertical Cylinder Heated From Below", *Journal of Fluid Mechanics*, v. 160, 1985, pages 137-154.
- [87] P. Dold, M. Schweizer, A. Croll, K.W. Benz, "Measurement of Microscopic Growth Rates in Float Zone Silicon Crystals", *Journal of Crystal Growth*, v. 237-239, 2002, pages 1671-1677.
- [88] Z. Juhasz, G. Szabo, "Fluctuations of Melt Temperature and Growth Rate During $\text{Bi}_4\text{Ge}_3\text{O}_{12}$ Growth", *Journal of Crystal Growth*, v.79, 1986, pages 303-307.
- [89] W.R. Wilcox, L.D. Fullmer, "Turbulent Free Convection in Czochralski Crystal Growth", *Journal of Applied Physics*, v. 37, no. 7, 1965, pages 2201-2206.
- [90] C.W. Lan, M.K. Chen, M.C. Liang, "Bifurcation and Stability Analyses of Horizontal Bridgman Crystal Growth of a Low Prandtl Number Material", *Journal of Crystal Growth*, v. 187, 1998, pages 303-313.
- [91] M.J. Stewart, F. Weinberg, "Fluid Flow in Liquid Metals", *Journal of Crystal Growth*, v.12, 1971, pages 228-238.
- [92] C.W. Lan, M.C. Su, M.C. Liang, "A Visualization and Computational Study of Horizontal Bridgman Crystal Growth", *Journal of Crystal Growth*, v.208, 2000, pages 717-725.
- [93] H.C. de Groh III, M. Yao, "Numerical and Experimental Study of Transport Phenomena in Directional Solidification of Succinonitrile", *Transport Phenomena in Solidification ASME*, v. 182, 1994, pages 227-243.
- [94] D. Schwabe, "Buoyant-Thermocapillary and Pure Thermocapillary Convective Instabilities in Czochralski Systems", *Journal of Crystal Growth*, v.237-239, 2002, pages 1849-1853.
- [95] *Matlab Help*, The Mathworks, Inc., 1984-2005.

- [96] T. Alboussiere, A.C. Neubrand, J.P. Garandet, R. Moreau, "Segregation During Horizontal Bridgman Growth Under an Axial Magnetic Field", v.181, **1997**, pages 133-144.
- [97] F.L. King, W.W. Harrison, "Glow Discharge Mass Spectrometry: An Introduction to the Technique and its Utility", *Mass Spectrometry Reviews*, v. 9, **1990**, pages 285-317.
- [98] M. Chopra, N. Singh, "Zone-Melting Studies on Eutectics", *Journal of Scientific and Industrial research*, v. 41, **1982**, pages 300-313.
- [99] L.P. Garandet, T. Alboussiere, "Bridgman Growth: Modeling and Experiments", *Progress in Crystal Growth and Characterization of Materials*, v. 38, **1999**, pages 73-132.
- [100] A.V. Churilov, A.G. Ostrogorsky, "Solidification of Te and Zn doped InSb in space", *42nd AIAA Aerospace Sciences Meeting and Exhibit*, Reno Nevada, 5-8 January **2004**.
- [101] <http://www.webelements.com>, accessed October 28, 2006.
- [102] J.A. Burton, E.D. Kolb, W.P. Slichter, J.D. Struthers, "Distribution of Solute in Crystals Grown from the Melt. Part II. Experimental", *The Journal of Chemical Physics*, v.21 no.11, **1953**, pages 1991-1995.
- [103] Colin Carew, Firebird Technologies Inc., private communication, June 9, **2006**.
- [104] L. Davoust, F. Bertrand, R. Moreau, P. Tanguy, R. Bolcato, "Recent Results on MHD Damped Convection in the Horizontal Bridgman Configuration", *Magnitnaia Gidrodinamika*, v.33 no.4, **1997**, pages 387-394.
- [105] D.T.J. Hurle, P. Rudolph, "A Brief History of Defect Formation, Segregation, Faceting, and Twinning in Melt-Grown Semiconductors", *Journal of Crystal Growth*, v. 264, **2004**, pages 550-564.
- [106] Hart Scientific, *Model 9122 Dry-Well Calibrator User Manual Rev. 2749*, 200 North 1300 West, Pleasant Grove, Utah 84062.
- [107] [http://ca.fluke.com/caen/products/specifications.htm?cs_id=17187\(FlukeProducts\)&category=MFCCAL\(FlukeProducts\)](http://ca.fluke.com/caen/products/specifications.htm?cs_id=17187(FlukeProducts)&category=MFCCAL(FlukeProducts)), accessed October 25, 2006.

[108] <http://digital.ni.com/manuals.nsf/websearch/332D9977C82446B7862570CF00702BA9>, accessed October 25, 2006.

[109] V. Cerny, "Comparing frequency domain, optimal, and asymptotic filtering: A tutorial", *Control and Intelligent Systems*, v 34, n 2, 2006, pages 136-142.

Chapter 7 Appendices

Appendix A Specifications for the Thermocouples, Drywell Calibrator, and Datalogger

Table A-1: Thermocouple Specifications

Model Number	A11 04-K-GSS-36
Type	K, grounded
Outer Diameter	1 mm
Length	12 thermocouples 36 “ 12 thermocouples 48 “
Sheath	316 Stainless Steel
Operating Range	0-1260°C
Response Time	0.1 s
Limits of Error	1.1°C or 0.4% whichever is greater

At 327.5°C, error is 1.3°C. Response time is based upon reaching 63.2% of boiling water temperature from room temperature.

Table A-2: Thermocouple calibration offset in degrees Celsius, measured at 327.5°C (melting temperature of lead)

Thermocouple	Offset (°C)	Plane	Location
1	0.1	A	Centre Top
2	0.2	A	Outer Top
3	-0.1	A	Inner Top
4	0.7	A	Bottom
5	-1.4	B	Centre Top
6	-1.3	B	Outer Top
7	0.4	B	Inner Top
8	0.8	B	Bottom
9	0.4	C	Top
10	0.3	C	Upper-Mid
11	0.6	C	Lower-Mid
12	0.4	C	Bottom
13	0.2	n/a	n/a
14	0.1	n/a	n/a
15	-2.6	n/a	Ambient
16	1.4	D	Bottom
17	1.4	E	Top
18	0.8	E	Upper-Mid
19	-1.2	E	Lower-Mid
20	n/a	E	Bottom
21	1.5	F	Top
22	-1.5	F	Upper-Mid
23	1.3	F	Lower-Mid
24	1.1	F	Bottom
25	1.1	D	Top
26	0.9	D	Upper-Mid
27	0.6	D	Lower-Mid

Drift of Drywell Calibrator is $\pm 0.02^{\circ}\text{C}$, Multifunction error is within $\pm 0.08^{\circ}\text{C}$. For a total, thermocouples are within $\pm 0.1^{\circ}\text{C}$ of each other.

Table A-3: Drywell calibrator specifications [106]

Power	110–125 V AC, 50–60 Hz, 700 Watts (optional 220 VAC, 50 Hz)
Ambient Temperature	5–50°C (40–120°F)
Temperature Range	0–600°C (32–1100°F)
Resolution	0.01°C or °F resolution
Accuracy	±0.1°C to 300°C, ±0.5°C to 600°C,
Control Stability	±0.02°C to 300°C, ±0.05°C to 600°C
Controller	Hybrid analog/digital controller with data retention
Heater	600 W, solid state relay switched
Cooling	27 CFM internal fan, Cooling coil for use below 100°C
Fault Protection	Sensor burnout protection, over temperature thermal cut-out, electrical fuse (6 A).
Test Wells	Four 3/4" dia. x 6" deep and 5 1/4" dia x 6" deep wells. Various diameter probe sleeves available.
Exterior Dimension	13.5" H x 7.8" W x 13" D .
Weight	26 lbs. including well sleeves

Accuracy at 327.5°C is ±0.15°C.

Table A-4: Fluke 725 Multifunction Calibrator specifications [107]

Measurement Accuracy	
Voltage DC	30.000 V 0.02%+ 2 counts (upper display) 30.000 V 0.02%+ 2 counts (lower display) 100.00 mV 0.02%+ 2 counts -10.00 mV to 75.00 mV 0.025 % + 1 count (via TC connector)
Current DC	24.000 mA 0.02%+ 2 counts
Resistance	0.0 to 400.0 Ω 0.1Ω (4-wire), 0.15Ω (2- and 3-wire) 401 to 1500 Ω 0.5Ω (4-wire), 1Ω (2- and 3-wire) 1500 to 3200 Ω 1Ω (4-wire), 1.5Ω (2- and 3-wire)
Frequency	2.0 to 1000.0 CPM 0.05 % + 1 count 1.0 to 1100.0 Hz 0.05 % + 1 count 1.00 to 10.00 kHz 0.05 % + 1 count Sensitivity 1 V peak-to-peak-minimum
Pressure	Accuracy from 0.025% of range using any of 29 pressure modules. (for detailed specifications refer to pressure modules in options and accessories) Modules available for differential, gage, vacuum, absolute, dual and high pressure.

Source Accuracy	
Voltage DC	100.00 mV 0.02%+2 counts 10.000 V 0.02%+2 counts -10.00 mV to 75.00 mV 0.025 % + 1 count (via TC connector)
Current DC	24.000 mA (Source) 0.02%+ 2 counts 24.000 mA (Simulate) 0.02%+ 2 counts
Resistance	15.0 to 400.0 Ω 0.15 Ω (exc. current 0.15 to 0.5 mA), 0.1 Ω (exc. current 0.5 to 2 mA) 401 to 1500 Ω 0.5 Ω(excitation current 0.05 to 0.8 mA) 1500 to 3200 Ω 1 Ω(excitation current 0.05 to 0.4 mA)
Frequency	2.0 to 1000.0 CPM 0.05% 1.0 to 1100.0 Hz 0.05% 1.00 to 10.00 kHz 0.25% Waveform: 5 V p-p squarewave, -0.1 V offset

**On thermocouple connection mode, accuracy is $\pm 0.025\%$ of 327.5 °C, or $\pm 0.08^\circ\text{C}$.
 (0.1°C display resolution)**

Table A-5: List of data acquisition equipment (for specifications access [108])

Part Number	Description
777687-03	SCXI-1303 32-Channel T/C terminal block
776572-02	SCXI-1102 32-channel T/C assembly
777745-01	NI PCI-6052E DAC for Windows
776574-492	SCXI-149 shielded cable
776671-03	LabVIEW Base for Windows
776576-60	SCXI-1360 front filler panel
776576-61	SCXI-1361 rear filler panel
778389-01	VI-logger
776570-01	SCXI-1000 4-Slot chassis, US 120VAC

Nominal range scale was 100 mV for K-type thermocouple data acquisition. Absolute accuracy in this range was 0.06%, or 0.2 °C at 327.5 °C. Resolution accuracy was 0.0028% or 0.009°C at 327.5 °C.

Appendix B Raw Data from Tests 1, 3, 4, and 5

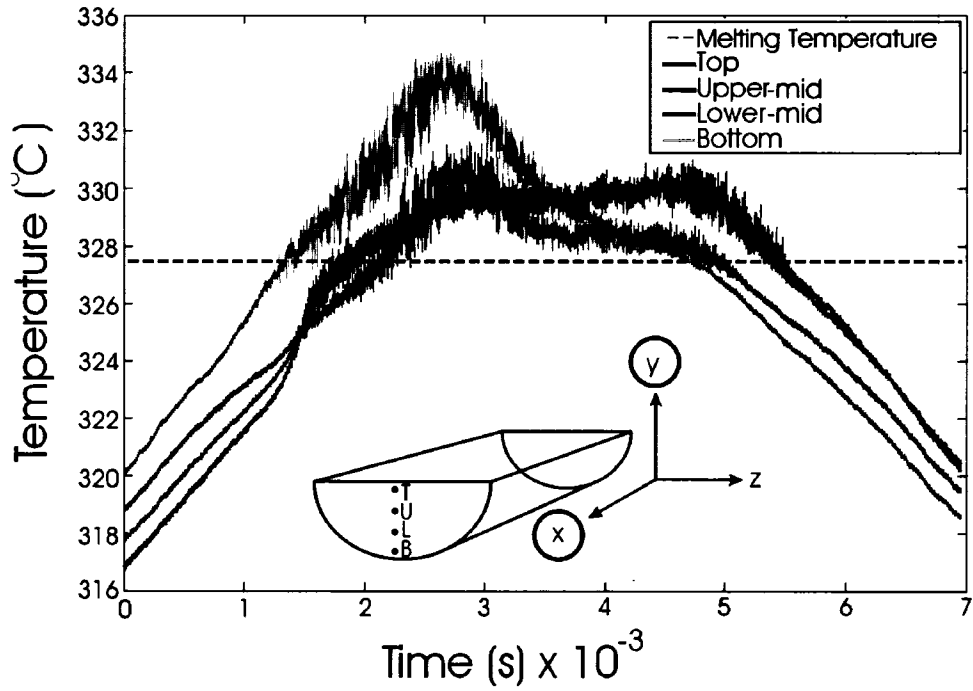


Figure B-1: Sample raw data from Test 1, Plane 'C', pass 3

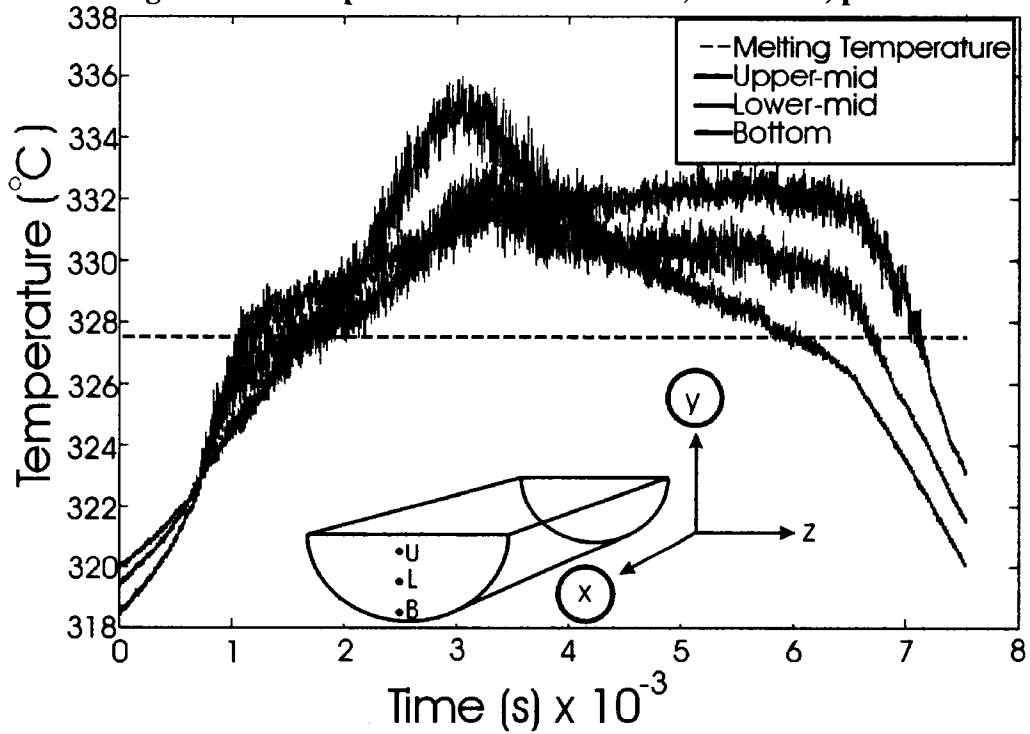


Figure B-2: Sample raw data from Test 3, Plane 'C', pass 3

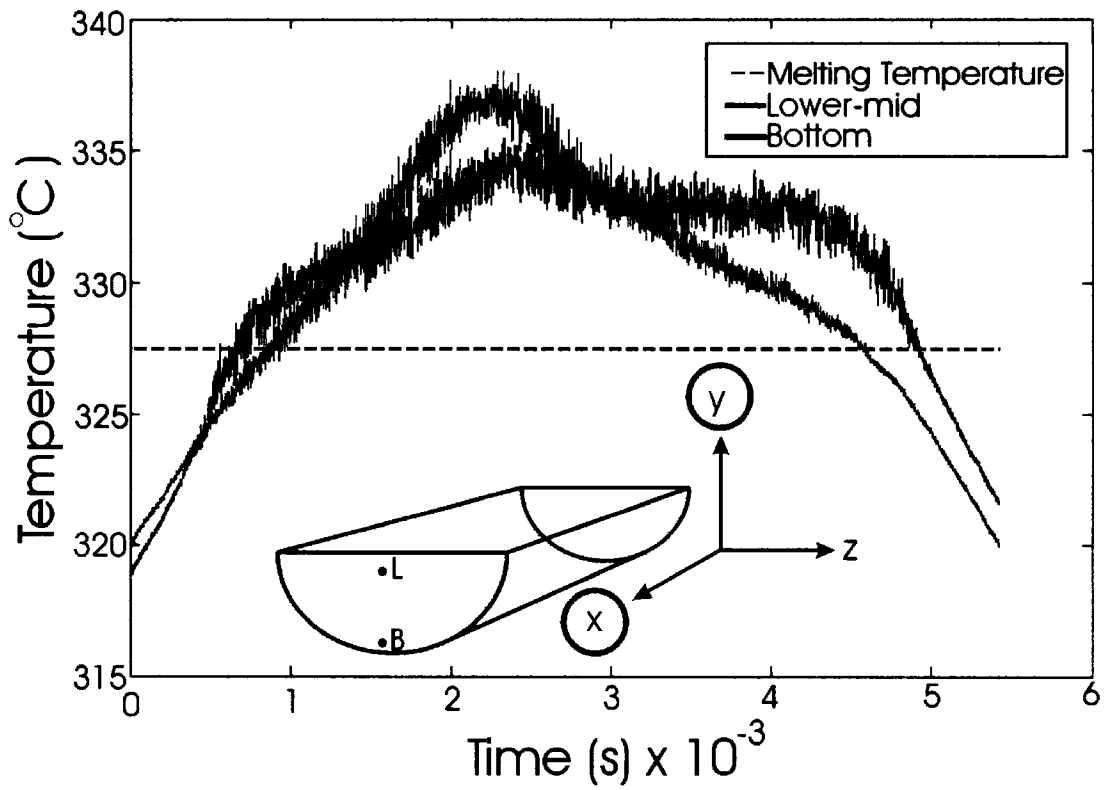


Figure B-3: Sample raw data from Test 4, Plane 'C', pass 2

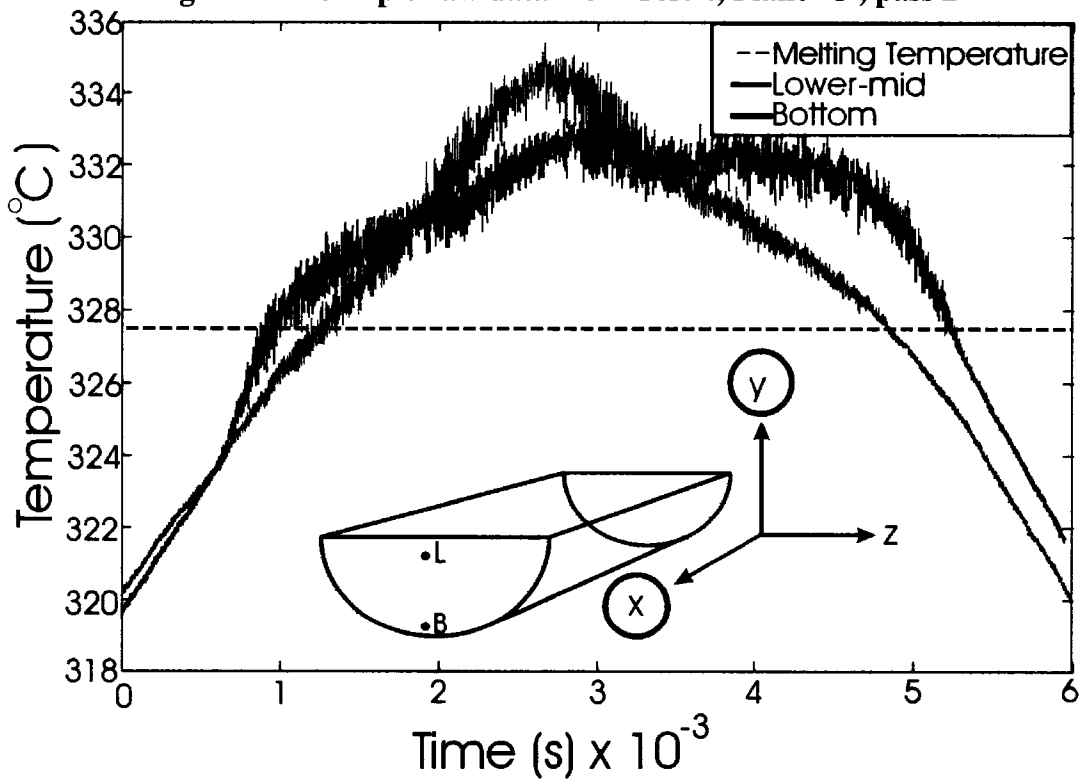
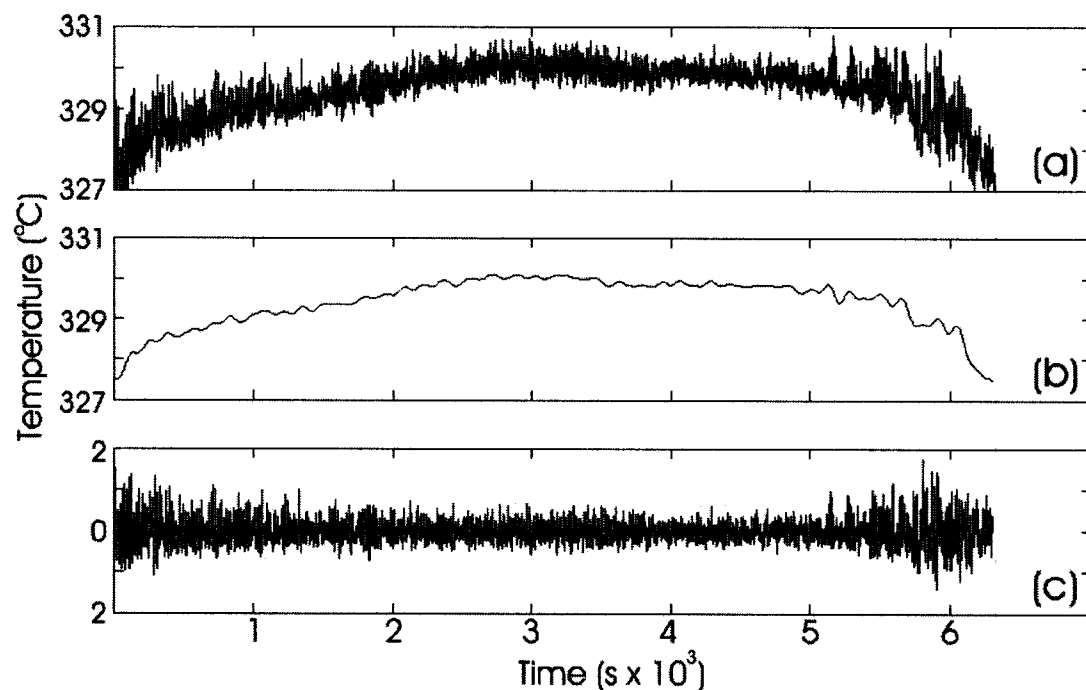


Figure B-4: Sample raw data from Test 5, Plane 'C', pass 1

Appendix C High and Low Pass Filter Design

A function in Matlab 7.1 called 'FILTFILT', isolate different ranges of frequencies within the temperature signal. The algorithm filters the data forwards and then again in reverse to eliminate any phase distortion. The coefficients of the filter were calculated using the 'BUTTER' function in Matlab 7.1 which utilizes a Butterworth filter design [109]. An example of the raw signal and then the output of low and high pass filters are shown in Figure C-1.



**Figure C-1: Temperature data from Test 2, plane 'C', top thermocouple
(a) raw data (b) low pass filtered data (c) high pass filtered data**

The cutoff frequency for both the high and low pass filters was chosen to be 0.008 hertz. This decision was based on the observation that very low frequencies corresponding to large sweeping temperature changes exhibited very large amplitudes while faster frequencies corresponding to fluid movement within the zone exhibited lower amplitude. For example, in Figure C-1 (b), the average temperature of the zone

fluctuates over time to a maximum of 330°C while the small temperature fluctuations corresponding to convective movement on Figure C-1 (c) occur within around 4°C of the average temperature. When analyzed using a discrete Fourier transform, general temperature trends exhibited much higher amplitudes than the higher frequencies. Figure C-2 shows the discrete Fourier transform of a temperature signal calculated using the ‘FFT’ function in Matlab 7.1. The cutoff frequency was chosen to take out the frequency with very large amplitudes. Note the difference in scale between graphs (a), (b), and (c).

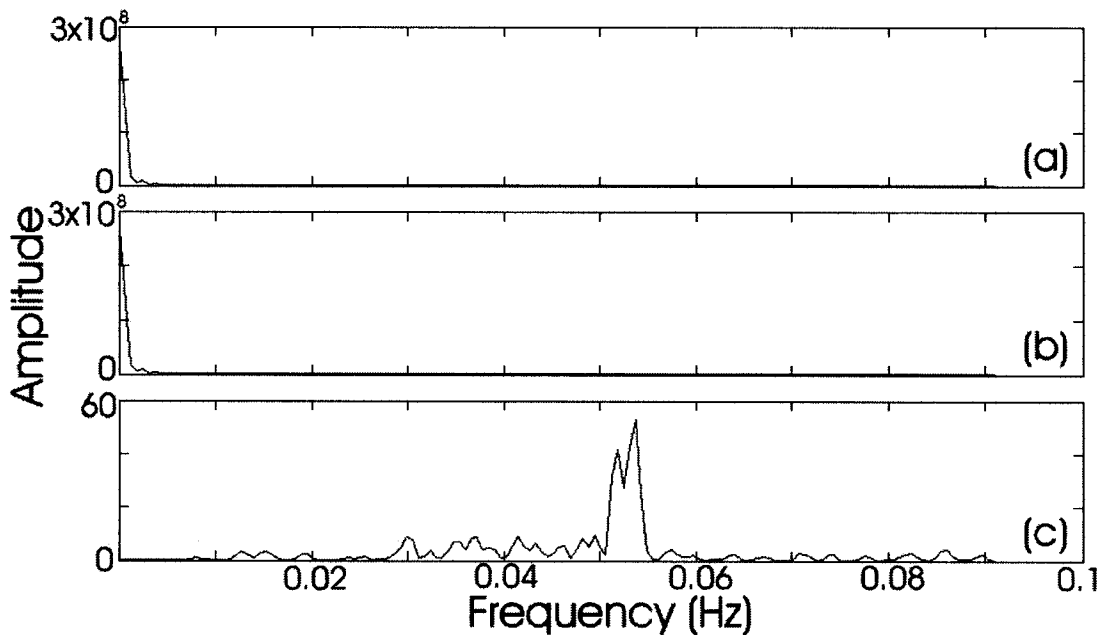


Figure C-2: Discrete Fourier transform of the top thermocouple, Test 2, plane 'C' (a) raw data (b) low pass filtered (c) high pass filtered
 The raw data signal in Figure C-2 (a) represents both general temperature trends and convective oscillations. Since the figure is scaled for general temperature trends of much higher amplitude, the small fluctuations are overshadowed and are not visible. When the low frequencies are removed as displayed in Figure C-2 (c), the higher frequency oscillations are visible.

Appendix D Wavelet Spectrum Plots for Tests 1, 3, 4, and 5

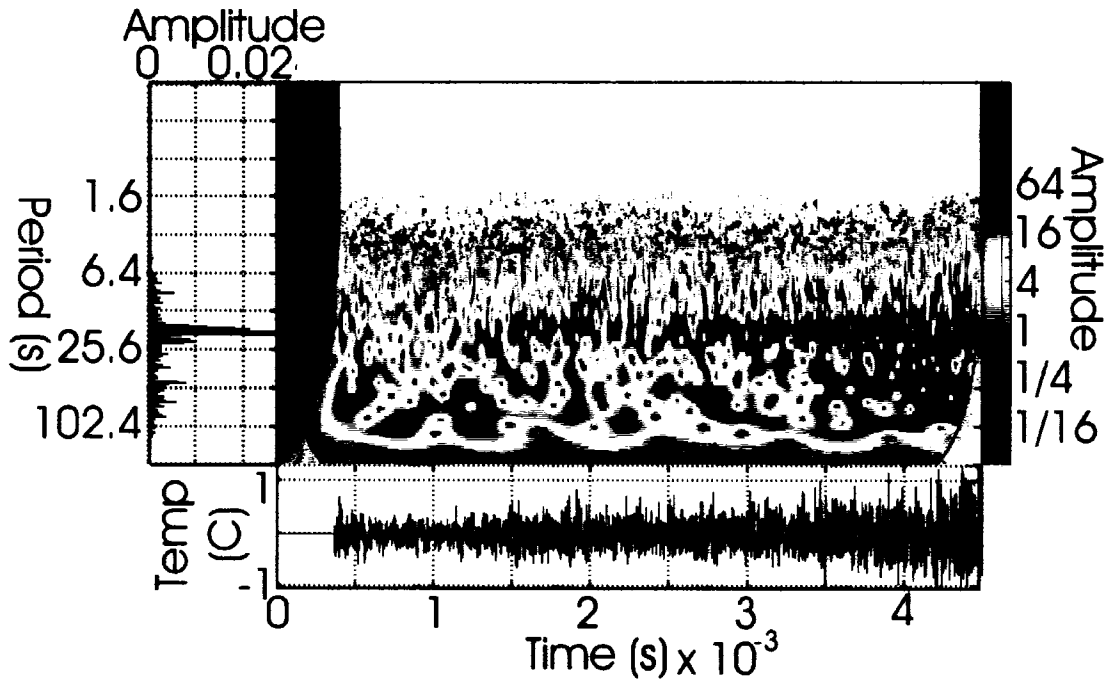


Figure D-1: Wavelet spectrum, Test 1, top thermocouple, plane 'C', pass 3

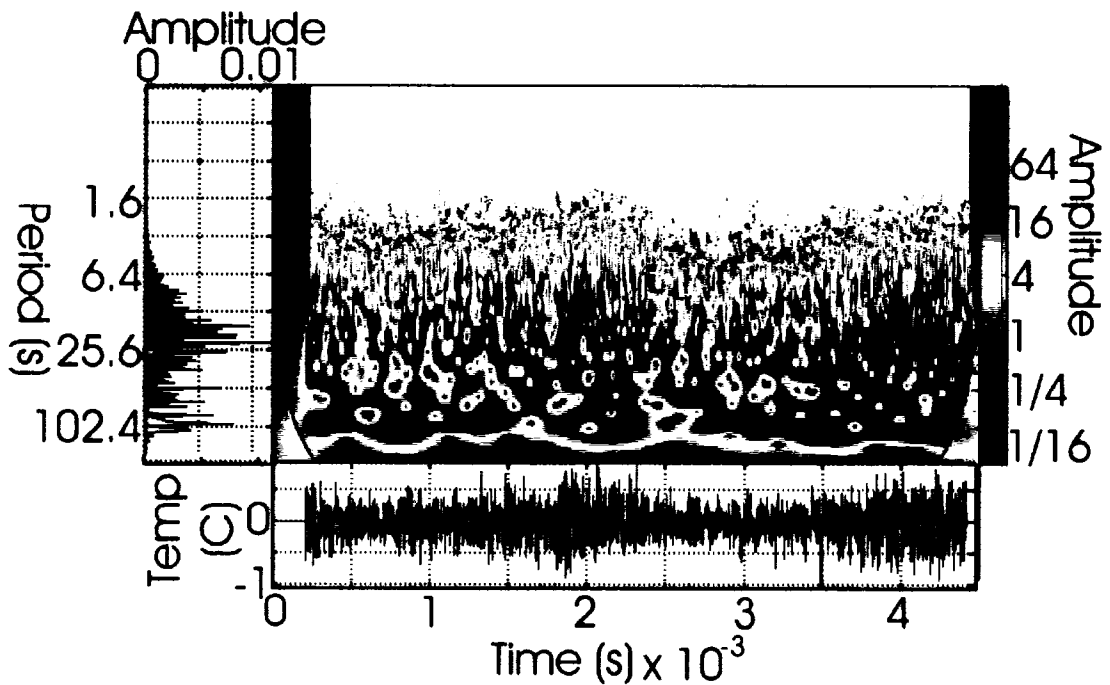


Figure D-2: Wavelet spectrum, Test 1, upper-mid thermocouple, plane 'C' pass 3

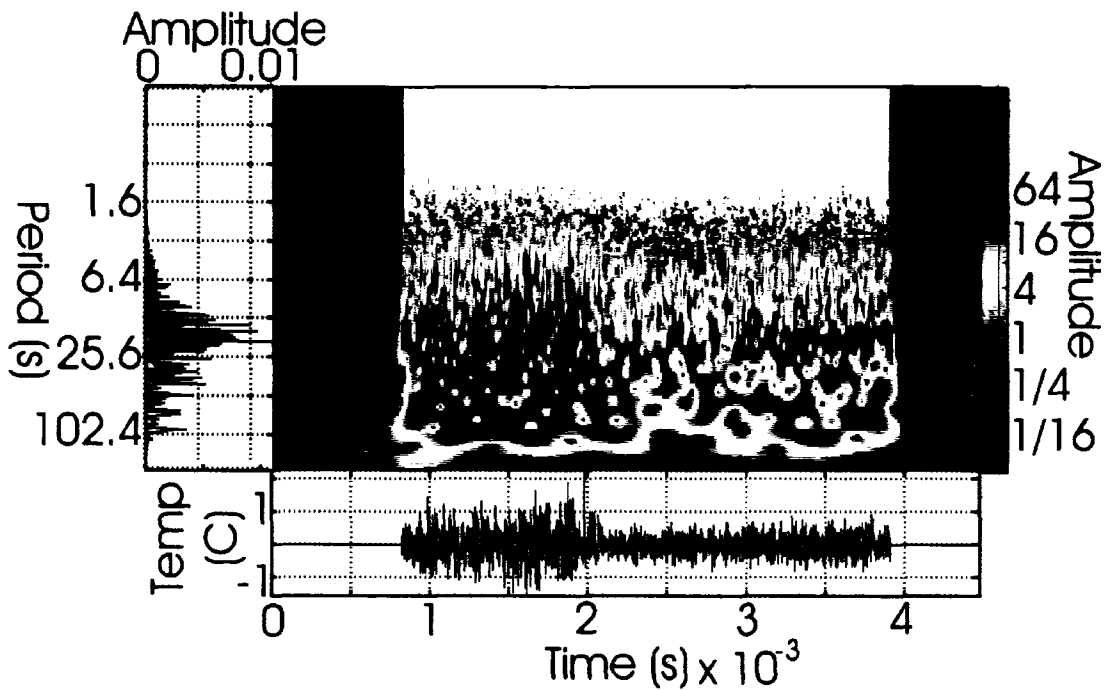


Figure D-3: Wavelet spectrum, Test 1, lower-mid thermocouple, plane 'C' pass 3

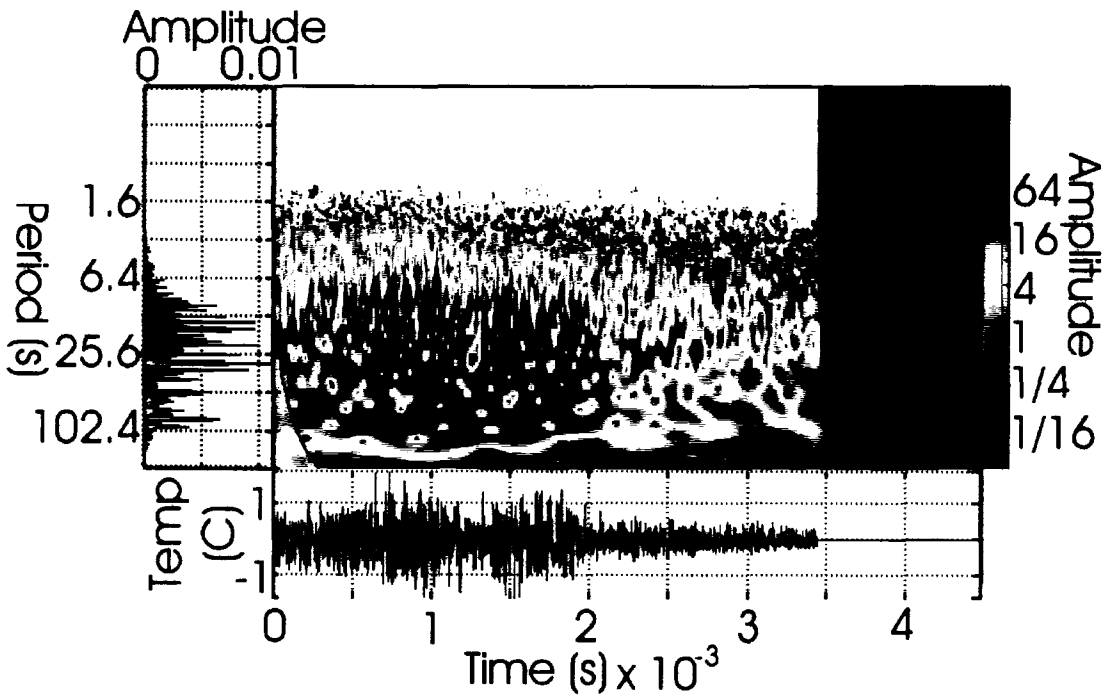


Figure D-4: Wavelet spectrum, Test 1, bottom thermocouple, plane 'C' pass 3

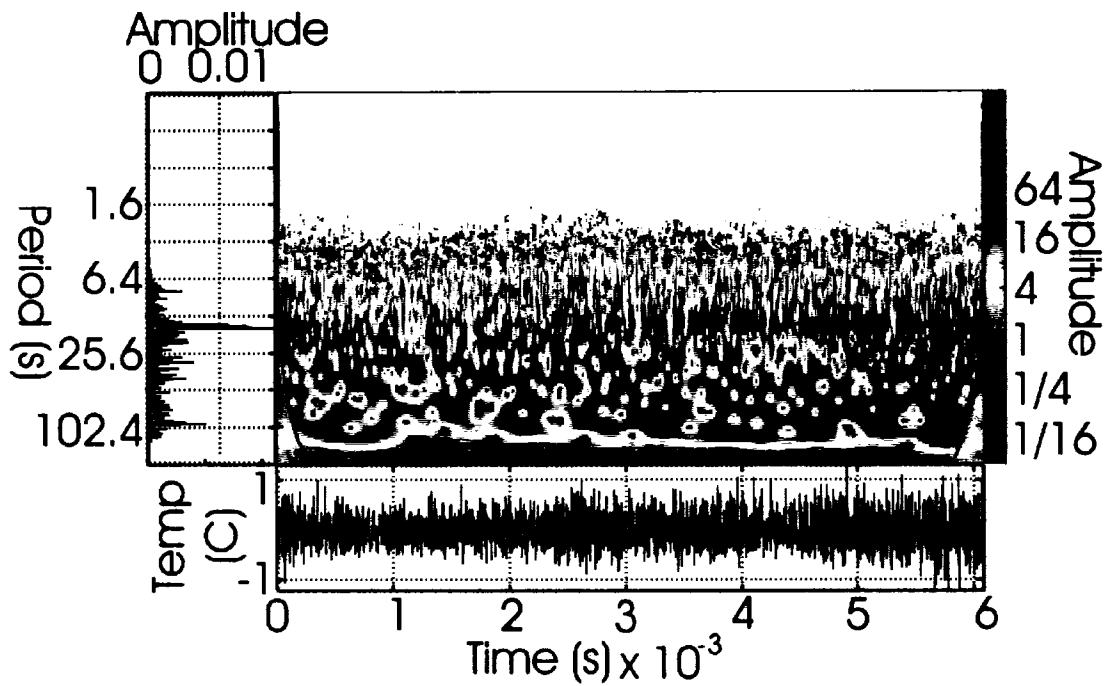


Figure D-5: Wavelet spectrum, Test 3, upper-mid thermocouple, plane 'C' pass 2

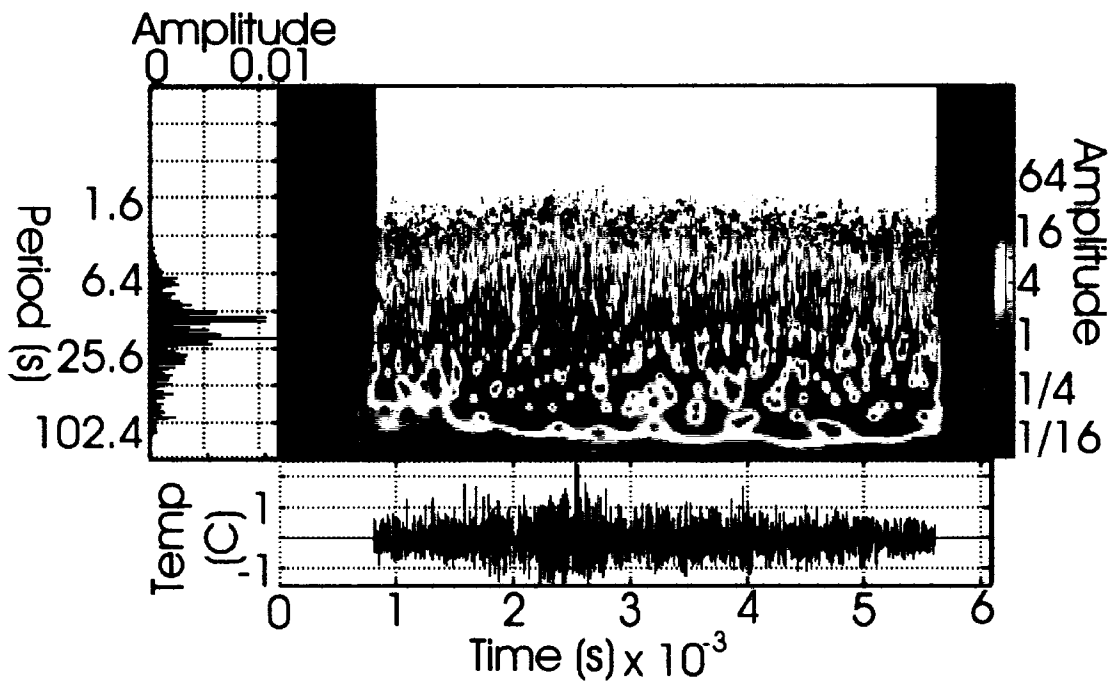


Figure D-6: Wavelet spectrum, Test 3, lower-mid thermocouple, plane 'C' pass 2

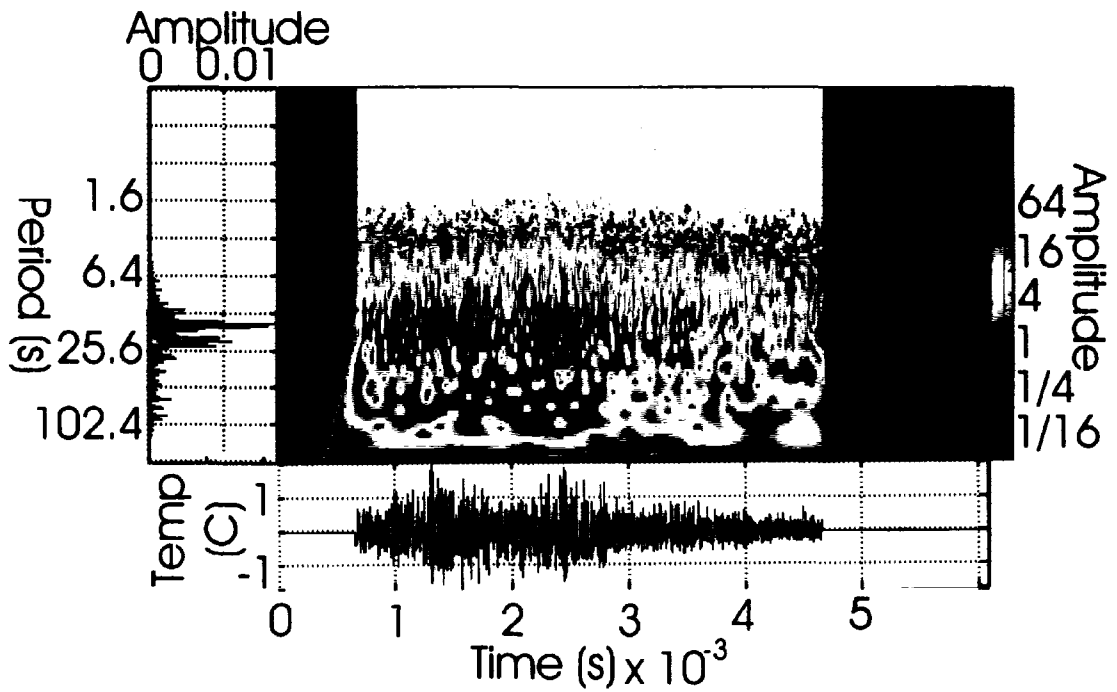


Figure D-7: Wavelet spectrum, Test 3, bottom thermocouple, plane 'C' pass 2

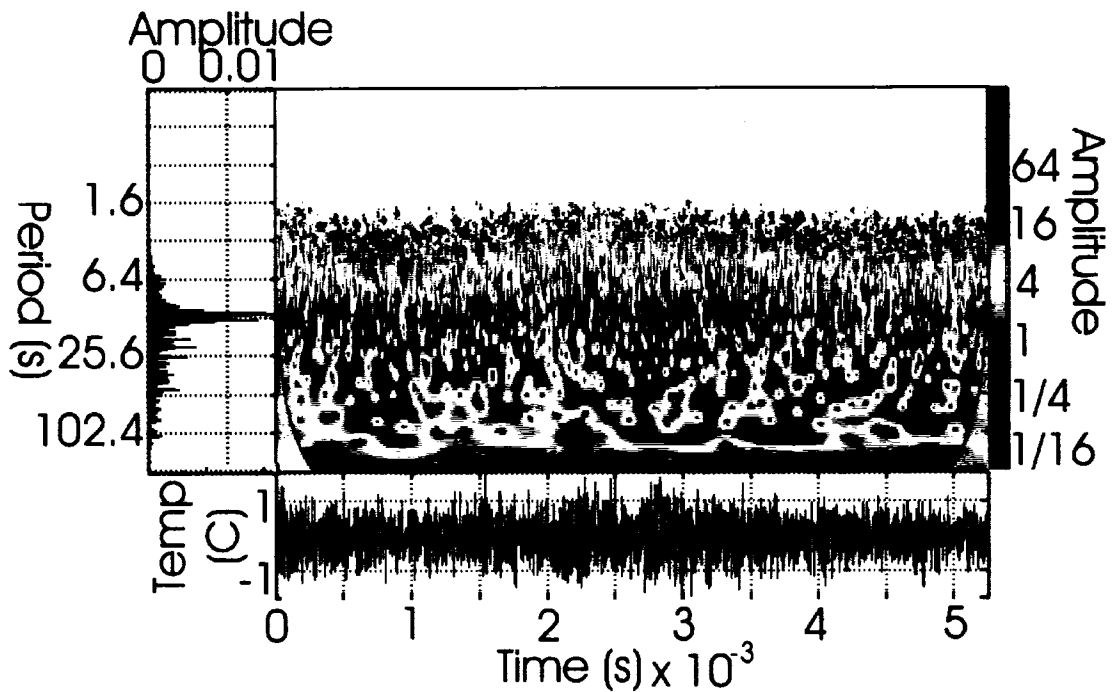


Figure D-8: Wavelet spectrum, Test 4, lower-mid thermocouple, plane 'C' pass 2

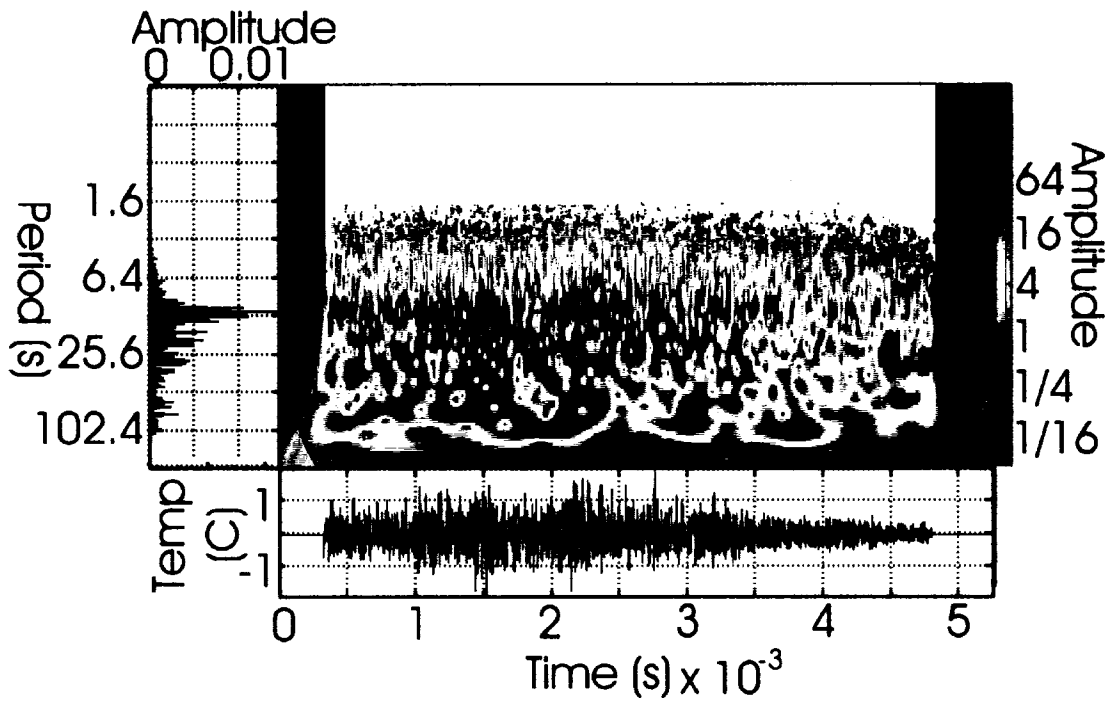


Figure D-9: Wavelet spectrum, Test 4, bottom thermocouple, plane 'C' pass 2

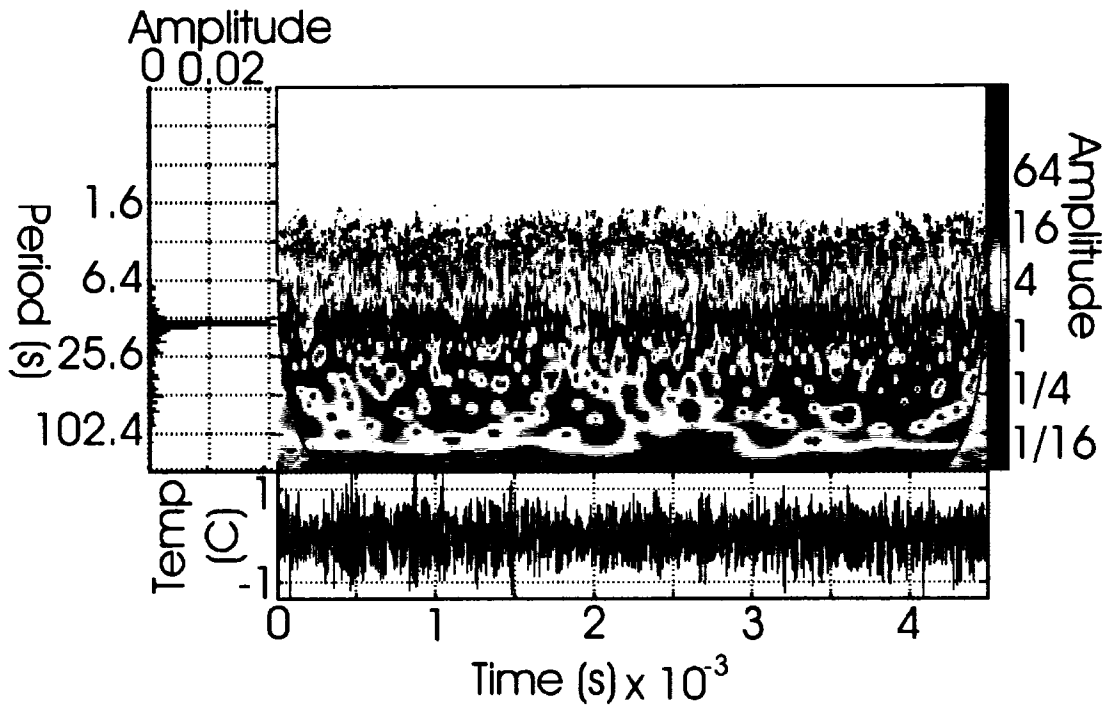


Figure D-10: Wavelet spectrum, Test 5, lower-mid thermocouple, plane 'C' pass 1

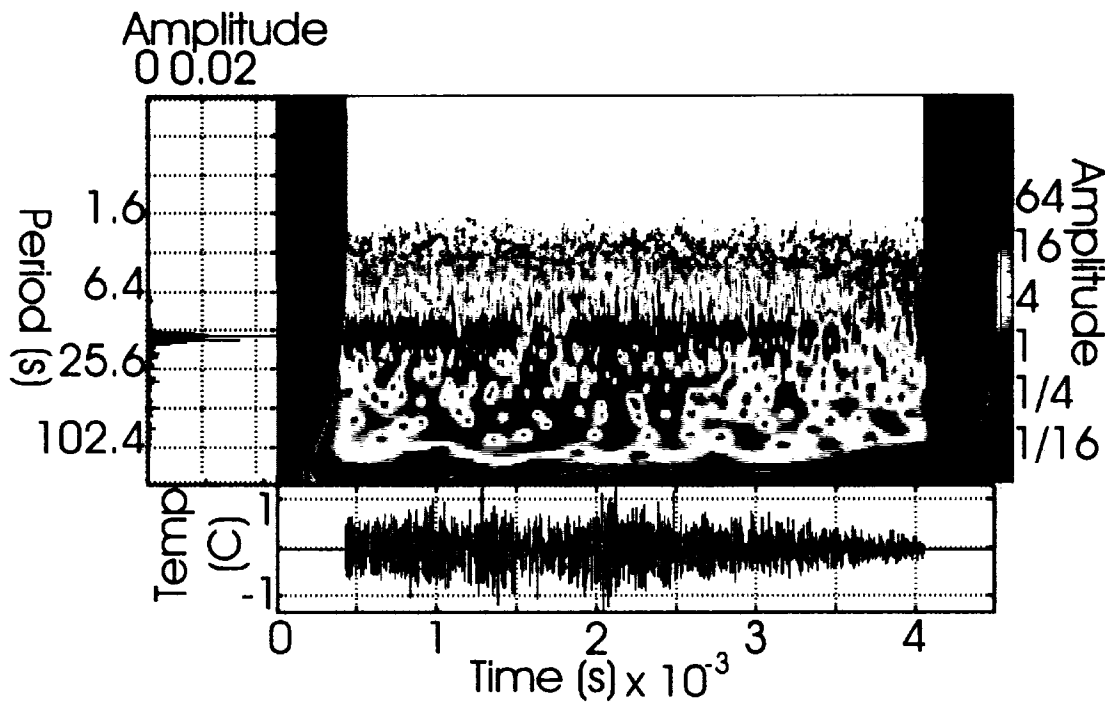


Figure D-11: Wavelet spectrum, Test 5, bottom thermocouple, plane 'C' pass 1

Appendix E Mass Balance Model Program

PROGRAM 'mass.m', calculates impurity profile after zone refining based upon mass balance around the molten zone. Concentration is calculated as a function of zone length (constant), number of passes (constant), initial concentration (constant), and separation coefficient. The program is structured to use sub-routines such as 'initial.m' to store constants, and 'diffusion.m' to simulate homogenization of concentration within the zone as described by models outlined in Section 2.1. The model accounts for partial passes at the beginning of the zone refining procedure and shutdown sequence at the end of the procedure. All programs were written and executed in Matlab 7.1.

```
%-----  
%PROGRAM 'mass.m'  
%Program to represent the mass balance around the molten zone  
%model the movement of each interface bounded by a time step and  
%interface velocity (they will move simultaneously therefore a constant  
%zone length  
  
%discretation point will be designed to coincide with time step at  
%a constant velocity (constant zone length)  
%zone length can be changed between passes.  
  
%MODEL SOLUTE ENTERING AND LEAVING AT MELTING AND FREEZING INTERFACE  
  
initial %sets up initial concentration profile and input variables  
  
n=0; %# of time steps (start at time zero)  
t=0;  
  
%STARTUP-----  
r=1; %count  
for p=1:8  
    C(:,p+1)=C(:,p);  
    %melt in  
    distan=round((9-p)*travel*discre);  
    Z=[];  
    Z=C(distan:Zsize+distan-1,p);  
    diffusion  
    %zone refine from melt in point  
    Z1=Z;
```

```

for n=distan+Zsize+1:discre
%shift all concentrations within the zone back one discretation point
for q=1:Zsize-1
    Z(q)=Z1(q+1);
end
%enter the concentration of the melting disc point to the end of
%the zone
Z(Zsize)=C(n,p);
%enter the leftover concentration of freezing disc point to the
%beginning of the zone
if k<1 %if tail moving
    Z(1)=Z(1)+(Z1(1)-k*Z1(1));
else %if head moving
    Z(1)=Z(1)-(k*Z1(1)-Z1(1));
end
C(n-Zsize,p+1)=k*Z1(1);
diffusion %mass movement within the zone
%use total to check mass balance has be retained
total=zeros(discre,1);
total(:,1)=C(:,p);
total(1:n-Zsize,1)=C(1:n-Zsize,p+1);
total(n-Zsize+1:n,1)=Z(:);

Z1=Z; %dump zone contents into resevoir variable for next calculation
t=t+r*dt; %total time taken
r=r+1; %count
end
%-----
%calculate freezing interface from x=1-L to x=L
%the last discretation point retains the concentration of the final liquid
r=1; %count
for n=discre+1:discre+Zsize-1
    %resize zone (reduce by one)
    Z=ones(size(Z,1)-1,1);
    Z(:)=Z1(2:size(Z1,1));
    %beginning of the zone
    if k<1 %if tail moving
        Z(1)=Z(1)+(Z1(1)-k*Z1(1));

    else %if head moving
        Z(1)=Z(1)-(k*Z1(1)-Z1(1));
    end
    C(n-Zsize,p+1)=k*Z1(1);
    diffusion
    Z1=Z;
    t=t+r*dt; %count time
    r=r+1; %count
end
C(discre,p+1)=Z;
end
%-----COMPLETED PASSES-----
for p=9:passes+passes-1 %repeat procedure for number of passes
%-----
%calculate melting interface into beginning of ingot up to distance x=L (no
%freezing interface)

```

```

Z=[]; %so it is not empty

%beginning index of Z is 1, end is the number of discretation points to the
%size of the zone
for n=1:Zsize
    Z1=Z;
    Z=ones(n,1); %resize zone
    Z(1:size(Z1))=Z1;
    Z(n)=C(n,p);
    diffusion %mass movement within zone
    t=t+dt*r; %total time taken
    r=r+1; %count
end
%-----
%calculate the melting interface from x=L to the end of the ingot
%calculate the freezing interface from x=0 to x=1-L
Z1=Z;
r=1; %count
for n=Zsize+1:discre
    %shift all concentrations within the zone back one discretation point
    for q=1:Zsize-1
        Z(q)=Z1(q+1);
    end
    %enter the concentration of the melting disc point to the end of
    %the zone
    Z(Zsize)=C(n,p);
    %enter the leftover concentration of freezing disc point to the
    %beginning of the zone
    if k<1 %if tail moving
        Z(1)=Z(1)+(Z1(1)-k*Z1(1));

    else %if head moving
        Z(1)=Z(1)-(k*Z1(1)-Z1(1));
    end
    C(n-Zsize,p+1)=k*Z1(1);
    diffusion %mass movement within the zone
    %use total to check mass balance has be retained
    total=zeros(discre,1);
    total(:,1)=C(:,p);
    total(1:n-Zsize,1)=C(1:n-Zsize,p+1);
    total(n-Zsize+1:n,1)=Z(:);

    Z1=Z; %dump zone contents into resevoir variable for next calculation
    t=t+r*dt; %total time taken
    r=r+1; %count
end
%-----
%calculate freezing interface from x=1-L to x=L
%the last discretation point retains the concentration of the final liquid
r=1; %count
for n=discre+1:discre+Zsize-1
    %resize zone (reduce by one)
    Z=ones(size(Z,1)-1,1);
    Z(:)=Z1(2:size(Z1,1));

```

```

%beginning of the zone
if k<1 %if tail moving
    Z(1)=Z(1)+(Z1(1)-k*Z1(1));

else %if head moving
    Z(1)=Z(1)-(k*Z1(1)-Z1(1));
end
C(n-Zsize,p+1)=k*Z1(1);
diffusion
Z1=Z;
t=t+r*dt; %count time
r=r+1; %count
end
C(discre,p+1)=Z;
End
%-----

```

```

%-----
%SUBROUTINE 'initial.m'
%sets up initial concentration profile and input variables

%zone length
zone=0.045; %as a fraction of ingot length, based on the mean zonelength in thermocouple data
%interface velocity
v=0.025; % equivalent to 55 mm/hr

%set up discretation points

%1 metre ingot length, 1 zone
ingot=1;
travel=18/155;

discre=1000; %number of discretation points
dx=ingot/discre; %discretation size

%number of dx in zone length
Zsize=round(zone*discre);

%sets up time step (how much time to move one discretation point?)
dt=ingot/(discre*v);

%number of passes
passes=9;

%value of k, separation coefficient
%k=0.95;

%initialize concentration
C=ones(discre,passes+passes); %one column for initial conc., a column for every pass

C(:,1)=initialcon;
%-----

%-----
%SUBROUTINE 'diffusion.m'

% assume perfect stirring and average the contents of the zone

Z(:)=sum(Z(:))/Zsize;
%-----

```

Appendix F Linear Least Squares Program

This section contains programs that were used to calculate k_{eff} based upon a linear least squares fit between the data and the mass balance model provided in Appendix D. The program makes a guess for k_{eff} , then iterates to minimize the least squares value between the data and the model. All programs were written and executed in Matlab 7.1. Dataset 'assay.mat' contains concentration data from assay analysis. Variable 'colheaders' contains the species name and test number for variables 'data' and 'control'. Variable 'control' contains the initial concentration prior to zone refining. Variable 'data' contains the concentration data for various after zone refining for tests 3,4 and 5 (columns) and at 10%, 50% and 80% of ingot length (rows). Program 'runleastsquares.m' runs a minimization routine called 'fminbnd' found in Matlab 7.1. Program 'distribution.m' sets up a function for the minimization routine in 'runleastsquares.m'

```
%-----  
% DATASET 'assay.mat'  
  
rowheaders =  
  
    'S3'  
    'S4'  
    'S5'  
    'Cu3'  
    'Cu4'  
    'Cu5'  
    'Ag3'  
    'Ag4'  
    'Ag5'  
    'Bi3'  
    'Bi4'  
    'Bi5'  
    'Ni3'  
    'Ni4'  
    'Ni5'  
    'I3'  
    'I4'
```

```

'I5'
'As3'
'As4'
'As5'
'Cd3'
'Cd4'
'Cd5'
'Te3'
'Te4'
'Te5'
'Cl3'
'Cl4'
'Cl5'

control =

2300
1700
55
300
6
3
25
3
4
70

data =

1.0e+04 *

1.40000000000000 0.00300000000000 0.00520000000000
0.01800000000000 0.00190000000000 0.00530000000000
0.05700000000000 0.01100000000000 0.00940000000000
0.55000000000000 0.00500000000000 0.00020000000000
0.03100000000000 0.00050000000000 0.00010000000000
0.05500000000000 0.00020000000000 0.00070000000000
0.03700000000000 0.00050000000000 0.00020000000000
0.00710000000000 0.00020000000000 0.00008000000000
0.01000000000000 0.00090000000000 0.00010000000000
0.05000000000000 0.02000000000000 0.02000000000000
0.03000000000000 0.03000000000000 0.02000000000000
0.03000000000000 0.03000000000000 0.03000000000000
0.00400000000000 0.00030000000000 0.00010000000000
0.00070000000000 0.00020000000000 0.00006000000000
0.00140000000000 0.00070000000000 0.00007000000000
0.00020000000000 0.00006000000000 0.00004000000000
0.00004000000000 0.00003000000000 0.00004000000000
0.00008000000000 0.00010000000000 0.00005000000000
0.00070000000000 0.00020000000000 0.00060000000000
0.00030000000000 0.00030000000000 0.00040000000000
0.00280000000000 0.00060000000000 0.00010000000000
0.00120000000000 0.00050000000000 0.00060000000000
0.00040000000000 0.00030000000000 0.00040000000000
0.00040000000000 0.00050000000000 0.00040000000000
0.00560000000000 0.00020000000000 0.00010000000000
0.00050000000000 0.00040000000000 0.00020000000000

```

0.00160000000000	0.00070000000000	0.00020000000000
0.00080000000000	0.00090000000000	0.00270000000000
0.00060000000000	0.00060000000000	0.00040000000000
0.00310000000000	0.00300000000000	0.00080000000000

%-----


```

%-----
%PROGRAM 'runleastsquares.m'
%run the least squares method to solve for keff

%minimize S

clear
load assay
t1=clock;
save t1 t1
for n=1:10
    initialcon=control(n);
    for p=1:3
        value80=data((3*n+p-3),1);
        value50=data((3*n+p-3),2);
        value10=data((3*n+p-3),3);

[keff(n,p),leastsquare(n,p)]=fminbnd(@(k)distribution(k,initialcon,value80,value50,value10),0.05,1)

    end
end
load t1
t2=clock;
etime(t2,t1)
save leastsquareskeff keff
%-----

```

```

%-----
% FUNCTION 'distribution.m'
%distribution solves the effective separation coefficient to match that
%of the data analysis based upon a linear least squares fit

function [S] = distribution(k,initialcon,value80,value50,value10)
    %STAT Interesting statistics.

    mass
    value(1)=C(800,18);
    value(2)=C(500,18);
    value(3)=C(100,18);
    meaner=mean([value80 value50 value10]);
    value=value-meaner;
    value80=value80-meaner;
    value50=value50-meaner;
    value10=value10-meaner;

    S=((value10)-(value(3)))^2+((value50)-(value(2)))^2+((value80)-(value(1)))^2;
%-----

```